New Graz (7839) Data Screening Algorithm

Van S Husson

ILRS Quality Control Board

Introduction

- **In February 2026, Michael Steindorfer from Graz (7839) developed a new data screening process. The current Fortran code was written by Georg Kirchner and is no longer maintainable. Legacy data screening is too slow, especially with larger datasets when using their MHz laser**
- **The new approach is semi-automatic: automatic cleaning with manual quality checking of results. If something goes wrong during automatic cleaning, the data will be manually recleaned**
- **Some differences between Georg's and Michael's new algorithm:**
  - New approach uses a "least squares orbit cleaning" for 2.2 sigma iteration of the data. Fitting is only used for coarse outlier removal, during the first 2.2 sigma iteration, the raw (unfitted) data is used
  - New approach uses NP bin cleaning: after coarse outlier removal 2.2 sigma orbit cleaning is done for each NP bin separately (i.e. batched cleaning). The cleaning adapts to parameters like: return rate changes, visibility of 2 CCRs simultaneously, tilt of CCR panels (e.g. GNSS, when the panel w.r.t to the observer leads to different raw data RMS)
  - Leading Edge (LE): It was not possible to exactly evaluate Georg's LE algorithm. The new approach tried to mimic, but there are differences. The new LE detection approach uses the first 5% of the data. Returns are accepted within 3 mm before and 17 mm after the LE. This is done individually for each NP. The LE detection is used for Lageos-1,-2, Lares-2 and Ajisai only, same as Georg's software
  - NP acceptance criterion: new approach applies a limit of a minimum of 100 points per NP bin and a NP precision <1.5 mm. The new approach produces less NPs, however; these criteria can be changed

7838 GRZL Dataset Comparison Approach

Satellite	# of CRDs
AJISAI	15
BEC	19
BEIDOU	50
Cryosat-2	11
ETALON-1	5
ETALON-2	4
GALILEO	83
GRACE-FO1	4
GRACE-FO2	4
HY-2B	6
HY-2C	13
HY-2D	13
JASON3	9
LAGEOS	15
LAGEOS-2	11
LARES	5
LARES2	10
LARETS	1
PAZ	3
SARAL	4
SENTINEL3A	10
SENTINEL3B	9
SENTINEL6A	14
SENTINEL6B	12
STARLETTE	25
STELLA	12
SWARM-A	2
SWARM-B	1
SWARM-C	2
SWOT	9
TANDEMX	3
TERRASARX	3
WESTPAC	2
Grand Total	389

- **Michael provided 389 CRDs (NPs and FR) using his new data screening approach. Michael knew that his kurtosis values were not normalized by subtracting a three**
- **The following checks were performed:**
  - For every CRD, the header and configuration records between the old and new were compared. The new H4 records start and end times are closer to the first and last NP, which is good
  - For every CRD, session tracking statistics (RMS, skew, kurtosis) from the old and new 50 session records were compared. Here is where there were some significant differences. The new RMSs were too small by a factor of two, but this was fixed in the analysis along with fixing the known kurtosis issue
  - For every LAGEOS class satellite, the calibration system delays from the new and old 40 calibration records were compared. The system delays differed slightly (typically sub-mm)
  - For one new LAGEOS pass, the new NP time of flights from the 11 records were compared to the corresponding new FR time of flights from the 10 records. The epochs agreed exactly, but the new FR CRD data didn't have the system delay applied
  - For one LAGEOS pass, FR and NPs between the old and new LE technique were compared

7839 GRZL LAGEOS-1 40 Calibration Record Analysis

		7839	7839 new	Sys Dly Diff	7839	7839 new	Cal Shift	7839	7839 new	Cal RMS	7839	7839 new	Cal Skew	7839	7839 new	Cal Kurtosis	7839	7839 new	P-M Diff
Satellite	Start Time	System Delay in ps		(mm)	Cal Shift in ps		Diff (mm)	Cal RMS in ps		Diff (mm)	Cal Skew		Diff	Cal Kurtosis		Diff	Cal Peak-Mean in ps		(mm)
lageos1	1/4/26 22:02	111822.4	111826.0	-0.54	-7.1	18.0	-3.8	16.0	16.0	0.0	0.016	0.016	0.000	-0.677	2.323	-3.000	-0.50	-0.50	0.0
lageos1	1/7/26 21:24	111813.2	111812.5	0.10	-14.7	21.0	-5.4	16.0	16.0	0.0	-0.008	0.008	-0.016	-0.679	2.322	-3.001	0.50	0.50	0.0
lageos1	1/8/26 1:03	111773.9	111777.0	-0.46	-5.8	16.0	-3.3	16.0	16.0	0.0	0.003	0.015	-0.012	-0.692	2.308	-3.000	0.00	0.00	0.0
lageos1	1/8/26 13:13	111788.4	111795.5	-1.06	-5.9	27.0	-4.9	16.5	16.5	0.0	0.025	0.025	0.000	-0.663	2.337	-3.000	-0.50	-0.50	0.0
lageos1	1/11/26 19:30	111780.2	111781.5	-0.19	-0.4	-1.0	0.1	17.0	16.5	0.1	0.007	0.011	-0.004	-0.682	2.344	-3.026	0.50	0.00	0.1
lageos1	1/11/26 23:19	111783.0	111782.5	0.07	0.0	1.0	-0.1	16.5	16.5	0.0	0.005	0.007	-0.002	-0.675	2.336	-3.011	-1.00	-0.50	-0.1
lageos1	1/14/26 12:00	111793.5	111793.5	0.00	0.4	-1.0	0.2	16.0	16.0	0.0	0.026	0.026	0.000	-0.677	2.322	-2.999	0.00	0.00	0.0
lageos1	1/14/26 15:37	111793.6	111793.0	0.09	0.6	-2.0	0.4	15.5	15.5	0.0	0.023	0.023	0.000	-0.680	2.320	-3.000	-0.50	-0.50	0.0
lageos1	1/14/26 19:00	111794.1	111793.5	0.09	1.5	-3.0	0.7	16.0	16.0	0.0	-0.003	0.005	-0.008	-0.672	2.328	-3.000	0.00	0.00	0.0
lageos1	1/14/26 22:25	111794.1	111794.0	0.01	-1.6	2.0	-0.5	16.0	16.0	0.0	0.007	0.015	-0.008	-0.653	2.348	-3.001	1.00	1.00	0.0
lageos1	1/15/26 21:05	111791.0	111791.0	0.00	0.8	-2.0	0.4	16.0	16.0	0.0	0.000	0.022	-0.022	-0.688	2.312	-3.000	1.00	1.00	0.0
lageos1	1/16/26 0:39	111792.1	111792.5	-0.06	-0.1	1.0	-0.2	16.0	16.0	0.0	0.005	0.005	0.000	-0.670	2.330	-3.000	0.50	0.50	0.0
lageos1	1/22/26 18:38	111792.9	111792.0	0.13	-5.0	18.0	-3.4	15.5	15.5	0.0	0.007	0.015	-0.008	-0.681	2.319	-3.000	-0.50	-0.50	0.0
lageos1	1/27/26 12:07	111802.1	111804.5	-0.36	9.2	-15.0	3.6	15.5	15.5	0.0	0.035	0.035	0.000	-0.665	2.335	-3.000	-0.50	-0.50	0.0
lageos1	1/27/26 15:41	111806.5	111809.0	-0.37	-1.2	8.0	-1.4	15.5	15.5	0.0	0.064	0.064	0.000	-0.678	2.322	-3.000	-2.00	-2.00	0.0
lageos1 aggregate		111794.7	111795.9	-0.17	-2.0	5.9	-1.2	16.0	16.0	0.0	0.014	0.019	-0.005	-0.675	2.327	-3.003	-0.13	-0.13	0.0

- ❑ **The system delays are not exact between the two versions of the software. All differences are less than 1 mm except the pass on 8-Jan-2026 at 13:13.**
- ❑ **The calibration shifts have opposite signs and different magnitudes between the two versions**
- ❑ **The calibration higher moments (RMS, skew, kurtosis) and Peak minus Mean (P-M) values are similar between the two versions, except the new software needs to subtract 3 from the kurtosis value to adhere to the CRD format**

7839 GRZL LAGEOS-1 50 Session Record Analysis

Satellite	Start Time	7839 RMS (ps)	7839 new RMS (ps)	RMS Diff in mm	7839 Skew	7839 new Skew	Skew Diff	7839 Kurtosis	7839 new Kurtosis	Kurtosis Diff	7839 Peak-Mean (ps)	7839 new Peak-Mean (ps)	P-M Diff (mm)
lageos1	1/4/26 22:02	35.1	16.4	2.80	0.155	0.053	0.102	-1.018	2.048	-3.066	-15.1	0.6	-2.35
lageos1	1/7/26 21:24	33.7	16.0	2.65	0.275	0.168	0.107	-0.879	2.155	-3.034	-14.8	-1.1	-2.05
lageos1	1/8/26 1:03	35.1	16.9	2.73	-0.075	-0.146	0.071	-1.075	1.932	-3.007	17.6	0.7	2.53
lageos1	1/8/26 13:13	35.9	17.2	2.80	0.132	0.108	0.024	-1.171	1.895	-3.066	-24.3	0.7	-3.75
lageos1	1/11/26 19:30	33.3	15.9	2.61	0.190	0.083	0.107	-0.884	2.147	-3.031	-7.9	-0.1	-1.17
lageos1	1/11/26 23:19	33.2	16.1	2.56	0.203	0.140	0.063	-0.981	2.033	-3.014	-20.9	-0.3	-3.09
lageos1	1/14/26 12:00	34.3	16.4	2.68	0.223	0.138	0.085	-0.965	2.064	-3.029	-16.6	-0.5	-2.41
lageos1	1/14/26 15:37	34.5	16.6	2.68	0.176	0.119	0.057	-1.056	1.969	-3.025	-19.4	-0.1	-2.89
lageos1	1/14/26 19:00	33.4	16.0	2.61	0.168	0.078	0.090	-0.939	2.091	-3.030	-15.1	0.3	-2.31
lageos1	1/14/26 22:25	32.3	14.9	2.61	0.344	0.235	0.109	-0.737	2.296	-3.033	-14.0	-1.4	-1.89
lageos1	1/15/26 21:05	33.3	16.0	2.59	0.177	0.083	0.094	-0.946	2.069	-3.015	-16.2	0.0	-2.43
lageos1	1/16/26 0:39	34.7	16.3	2.76	0.391	0.331	0.060	-0.954	2.150	-3.104	-19.9	-2.7	-2.58
lageos1	1/22/26 18:38	32.9	15.5	2.61	0.294	0.195	0.099	-0.816	2.198	-3.014	-14.3	-1.3	-1.95
lageos1	1/27/26 12:07	34.7	16.4	2.74	0.194	0.119	0.075	-1.000	2.071	-3.071	-17.3	-0.2	-2.56
lageos1	1/27/26 15:41	33.1	16.0	2.56	0.036	-0.134	0.170	-0.916	2.216	-3.132	-9.6	1.1	-1.60
lageos1 aggregate		34.0	16.2	2.67	0.192	0.105	0.088	-0.956	2.089	-3.045	-13.9	-0.3	-2.03

- **The Session RMSs were too low by a factor of 2 with the new software. The Session skew is less with the new software. The session kurtosis is different, and the new software needs to subtract 3 from the kurtosis value to adhere to the CRD format**
- **The LAGEOS-1, LAGEOS-2, and LARES-2 Session Peak minus Mean (P-M) values are different by up to 3.1 mm, 3.2 mm and 2.8 mm; respectively**

New 50 Session RMS more than doubled

Start Date & Time	Satellite	Legacy RMS	Legacy Skew	Legacy Kurto	New RMS (p	New Skew	New Kurtosis
1/11/26 19:58	BEC	35	0.110	-0.607	83	0.496	2.609
1/27/26 15:37	BEC	50	0.054	-0.498	148	0.392	1.521
1/14/26 13:55	BEIDOU3M15	32	0.064	-0.675	100	-1.084	101.473
1/7/26 21:43	BEIDOU3M19	63	-0.049	-0.845	461	0.143	1.880
1/14/26 21:15	BEIDOU3M19	44	0.131	-0.711	321	0.483	4.429
1/4/26 19:43	BEIDOU3M2	61	-0.003	-0.674	130	0.506	34.169
1/14/26 18:03	BEIDOU3M20	65	-0.047	-1.038	1527	-0.163	2.329
1/14/26 18:59	BEIDOU3M21	36	-0.018	-0.806	96	-3.096	72.351
1/14/26 11:55	BEIDOU3M22	27	0.030	-0.722	481	0.123	3.129
1/8/26 12:07	BEIDOU3M23	58	-0.016	-0.926	301	0.295	8.964
1/14/26 11:19	BEIDOU3M6	60	0.018	-0.849	219	-0.045	15.734
1/18/26 17:19	BEIDOU3M9	68	-0.125	-0.861	347	0.370	4.784
1/13/26 12:40	GALILEO101	66	-0.052	-0.880	163	0.958	32.590
1/4/26 15:52	GALILEO102	73	0.107	-0.633	149	-0.345	25.294
1/13/26 9:00	GALILEO202	92	0.041	-0.654	246	-0.321	12.339
1/14/26 11:20	GALILEO202	44	0.068	-0.598	94	-0.064	2.992
1/15/26 19:59	GALILEO203	95	0.038	-0.760	196	-0.126	11.480
1/4/26 20:28	GALILEO213	60	0.002	-0.733	132	-0.120	20.406
1/4/26 17:59	GALILEO216	91	0.071	-0.808	302	-0.181	6.806
1/14/26 11:56	GALILEO218	27	0.003	-0.644	87	1.117	91.784
1/7/26 22:20	GALILEO219	71	0.037	-0.650	462	0.102	1.951
1/14/26 20:24	GALILEO219	61	0.043	-0.669	2709	-0.990	19.869
1/14/26 16:32	GALILEO224	46	0.101	-0.715	138	-0.057	17.663
1/14/26 20:16	GALILEO224	49	0.054	-0.718	101	0.161	21.766
1/15/26 20:32	GALILEO225	56	0.005	-0.709	151	1.840	39.105
1/11/26 11:56	GALILEO226	123	0.006	-0.951	294	0.101	7.498
1/15/26 16:08	GALILEO226	98	0.032	-0.707	198	0.380	5.958
1/11/26 17:24	GRACE-FO2	18	-0.035	-0.748	197	-0.533	692.047

Start Date & Time	Satellite	Legacy RMS	Legacy Skew	Legacy Kurto	New RMS (p	New Skew	New Kurtosis
1/11/26 17:24	GRACE-FO2	18	-0.035	-0.748	197	-0.533	692.047
1/14/26 14:32	HY-2B	22	-0.047	-0.630	284	-0.407	19.377
1/14/26 9:37	HY-2C	19	0.078	-0.673	60	1.838	288.049
1/14/26 11:27	HY-2C	19	0.034	-0.679	59	2.745	117.772
1/27/26 13:44	HY-2C	23	0.126	-0.712	71	1.174	172.702
1/27/26 15:31	HY-2C	20	0.146	-0.771	399	0.090	2.990
1/13/26 15:51	HY-2D	19	0.067	-0.678	54	-1.612	342.365
1/27/26 13:00	HY-2D	18	0.060	-0.706	52	2.208	274.981
1/14/26 7:33	JASON3	19	0.119	-0.665	104	0.548	85.729
1/15/26 21:31	LARES2	30	0.225	-0.707	198	0.366	23.297
1/19/26 15:09	LARES2	45	0.222	-0.729	120	-2.670	63.588
1/22/26 18:31	LARES2	32	0.219	-0.751	97	-0.312	92.012
1/13/26 15:38	PAZ	16	0.005	-0.697	65	-0.011	170.893
1/7/26 21:43	SENTINEL3A	17	0.011	-0.717	100	-3.354	119.100
1/8/26 9:52	SENTINEL3A	17	0.019	-0.688	191	0.119	20.996
1/14/26 9:59	SENTINEL3B	18	0.046	-0.696	42	-0.562	464.808
1/5/26 1:38	SENTINEL6A	21	0.078	-0.700	51	-1.447	300.900
1/7/26 22:56	SENTINEL6A	21	0.093	-0.760	145	-1.355	26.144
1/14/26 21:43	SENTINEL6A	18	0.053	-0.677	139	112.333	12912.128
1/7/26 22:57	SENTINEL6B	20	0.011	-0.739	135	-0.128	52.174
1/14/26 5:10	SENTINEL6B	19	0.090	-0.660	70	-0.509	180.749
1/14/26 7:07	SENTINEL6B	23	0.135	-0.712	50	2.944	223.298
1/14/26 9:03	SENTINEL6B	17	0.041	-0.668	55	3.403	170.673
1/27/26 15:16	STARLETTE	22	0.127	-0.670	49	2.011	315.898
1/14/26 18:03	STELLA	24	0.167	-0.607	86	-3.179	130.578
1/14/26 21:22	STELLA	51	0.086	-0.463	199	14.379	992.056
1/14/26 13:45	WESTPAC	16	0.004	-0.714	137	-0.188	50.411

- **When the new session RMS more than doubled, the kurtosis minus three always (100%) exceeds +1**
- **When the new session RMS more than doubled, sometimes the absolute value of skew is greater than 1**
- **Three out of 10 LARES-2 passes (LE filter applied) are on this list**

New 50 Session Skew greater than 1

Satellite	Legacy			New		
	RMS (p	Skew	Kurtos	RMS (p	Skew	Kurtosis
BEC	82	0.107	-0.976	131	1.364	106.246
BEIDOU3M15	32	0.064	-0.675	100	-1.084	101.473
BEIDOU3M21	36	-0.018	-0.806	96	-3.096	72.351
Cryosat-2	18	0.092	-0.672	27	-5.114	864.205
Cryosat-2	17	0.061	-0.698	19	-1.238	57.483
Cryosat-2	18	0.049	-0.676	25	3.993	1393.247
GALILEO218	27	0.003	-0.644	87	1.117	91.784
GALILEO225	56	0.005	-0.709	151	1.840	39.105
GRACE-FO1	18	0.088	-0.668	22	1.399	112.442
HY-2C	19	0.078	-0.673	60	1.838	288.049
HY-2C	19	0.034	-0.679	59	2.745	117.772
HY-2C	23	0.126	-0.712	71	1.174	172.702
HY-2D	19	0.067	-0.678	54	-1.612	342.365
HY-2D	18	0.060	-0.706	52	2.208	274.981
JASON3	19	0.072	-0.687	27	-1.126	694.079
LARES2	45	0.222	-0.729	120	-2.670	63.588
SENTINEL3A	17	0.011	-0.717	100	-3.354	119.100
SENTINEL3A	18	0.061	-0.693	27	1.496	556.877
SENTINEL6A	21	0.078	-0.700	51	-1.447	300.900
SENTINEL6A	21	0.093	-0.760	145	-1.355	26.144
SENTINEL6A	20	0.056	-0.666	29	-7.769	697.724
SENTINEL6A	18	0.053	-0.677	139	112.333	12912.128
SENTINEL6B	23	0.135	-0.712	50	2.944	223.298
SENTINEL6B	17	0.041	-0.668	55	3.403	170.673
SENTINEL6B	19	0.082	-0.688	22	-5.155	304.788
STARLETTE	23	0.084	-0.641	42	2.584	332.611
STARLETTE	22	0.127	-0.670	49	2.011	315.898
STELLA	24	0.167	-0.607	86	-3.179	130.578
STELLA	51	0.086	-0.463	199	14.379	992.056
SWARM-A	19	0.072	-0.701	25	1.375	47.385
SWOT	20	0.118	-0.655	34	1.382	247.642

- **When the absolute value of the new session skew exceeds 1, the kurtosis minus three always (100%) exceeds +1**
  - and the new session RMS is more than doubled ~50% of the time

New 50 Session Kurtosis' Minus 3 is greater than 1

Satellite	Legacy RMS	Legacy Skew	Legacy Kurto	New RMS (p	New Skew	New Kurtosis
BEC	82	0.107	-0.976	131	1.364	106.246
BEC	79	0.112	-0.791	143	0.033	27.135
BEC	50	0.054	-0.498	148	0.392	1.521
BEIDOU3M15	32	0.064	-0.675	100	-1.084	101.473
BEIDOU3M16	66	0.066	-0.661	73	0.217	3.003
BEIDOU3M19	63	-0.049	-0.845	461	0.143	1.880
BEIDOU3M19	106	-0.012	-0.866	202	0.059	7.687
BEIDOU3M19	44	0.131	-0.711	321	0.483	4.429
BEIDOU3M2	61	-0.003	-0.674	130	0.506	34.169
BEIDOU3M2	61	0.016	-0.646	83	0.373	29.667
BEIDOU3M20	65	-0.047	-1.038	1527	-0.163	2.329
BEIDOU3M20	46	-0.045	-0.640	72	0.433	1.846
BEIDOU3M21	36	-0.018	-0.806	96	-3.096	72.351
BEIDOU3M21	69	-0.015	-0.763	121	0.820	43.048
BEIDOU3M22	27	0.030	-0.722	481	0.123	3.129
BEIDOU3M23	58	-0.016	-0.926	301	0.295	8.964
BEIDOU3M4	117	0.128	-0.763	127	0.148	4.849
BEIDOU3M6	60	0.018	-0.849	219	-0.045	15.734
BEIDOU3M9	68	-0.125	-0.861	347	0.370	4.784
Cryosat-2	18	0.092	-0.672	27	-5.114	864.205
Cryosat-2	17	0.061	-0.698	19	-1.238	57.483
Cryosat-2	18	0.049	-0.676	25	3.993	1393.247
GALILEO101	42	0.049	-0.706	80	-0.098	1.808
GALILEO101	66	-0.052	-0.880	163	0.958	32.590
GALILEO102	73	0.107	-0.633	149	-0.345	25.294
GALILEO201	134	0.024	-0.723	166	0.380	10.372
GALILEO201	75	-0.005	-0.606	106	0.175	17.238
GALILEO202	92	0.041	-0.654	246	-0.321	12.339
GALILEO202	44	0.068	-0.598	94	-0.064	2.992
GALILEO202	82	-0.117	-0.674	100	-0.358	3.511
GALILEO203	95	0.038	-0.760	196	-0.126	11.480
GALILEO207	82	-0.006	-0.633	95	0.149	18.809
GALILEO213	60	0.002	-0.733	132	-0.120	20.406
GALILEO216	91	0.071	-0.808	302	-0.181	6.806
GALILEO216	95	0.021	-0.759	121	0.403	18.043
GALILEO218	27	0.003	-0.644	87	1.117	91.784
GALILEO219	71	0.037	-0.650	462	0.102	1.951
GALILEO219	61	0.043	-0.669	2709	-0.990	19.869
GALILEO222	107	0.083	-0.981	214	-0.771	11.513
GALILEO224	46	0.101	-0.715	138	-0.057	17.663
GALILEO224	49	0.054	-0.718	101	0.161	21.766
GALILEO225	56	0.005	-0.709	151	1.840	39.105
GALILEO226	123	0.006	-0.951	294	0.101	7.498
GALILEO226	98	0.032	-0.707	198	0.380	5.958

Start Date & Time	Satellite	Legacy RMS	Legacy Skew	Legacy Kurto	New RMS (p	New Skew	New Kurtosis
1/11/26 17:23	GRACE-FO1	19	0.018	-0.655	28	0.291	159.346
1/14/26 17:16	GRACE-FO1	18	0.088	-0.668	22	1.399	112.442
1/11/26 17:24	GRACE-FO2	18	-0.035	-0.748	197	-0.533	692.047
1/14/26 14:32	HY-2B	22	-0.047	-0.630	284	-0.407	19.377
1/14/26 9:37	HY-2C	19	0.078	-0.673	60	1.838	288.049
1/14/26 11:27	HY-2C	19	0.034	-0.679	59	2.745	117.772
1/14/26 16:53	HY-2C	19	0.098	-0.693	20	-0.655	163.751
1/27/26 13:44	HY-2C	23	0.126	-0.712	71	1.174	172.702
1/27/26 15:31	HY-2C	20	0.146	-0.771	399	0.090	2.990
1/13/26 15:51	HY-2D	19	0.067	-0.678	54	-1.612	342.365
1/14/26 14:22	HY-2D	20	0.081	-0.687	20	-0.473	45.815
1/14/26 23:25	HY-2D	18	0.077	-0.660	26	0.448	549.719
1/15/26 23:44	HY-2D	20	0.062	-0.701	20	0.014	6.245
1/27/26 13:00	HY-2D	18	0.060	-0.706	52	2.208	274.981
1/5/26 1:21	JASON3	19	0.072	-0.687	27	-1.126	694.079
1/14/26 7:33	JASON3	19	0.119	-0.665	104	0.548	85.729
1/14/26 23:59	JASON3	34	0.344	-0.732	35	0.512	6.011
1/14/26 23:08	LARES2	30	0.205	-0.719	22	0.717	207.714
1/15/26 21:31	LARES2	30	0.225	-0.707	198	0.366	23.297
1/19/26 15:09	LARES2	45	0.222	-0.729	120	-2.670	63.588
1/22/26 18:31	LARES2	32	0.219	-0.751	97	-0.312	92.012
1/27/26 14:43	LARES2	31	0.202	-0.723	22	0.693	49.422
1/14/26 14:46	LARETS	21	0.054	-0.722	22	0.131	1.282
1/13/26 15:38	PAZ	16	0.005	-0.697	65	-0.011	170.893
1/22/26 17:48	SARAL	17	0.058	-0.669	23	0.651	819.160
1/4/26 19:39	SENTINEL3A	16	0.076	-0.701	17	0.829	63.315
1/7/26 21:43	SENTINEL3A	17	0.011	-0.717	100	-3.354	119.100
1/8/26 9:52	SENTINEL3A	17	0.019	-0.688	191	0.119	20.996
1/14/26 18:42	SENTINEL3A	18	0.049	-0.716	22	0.474	93.208
1/14/26 20:20	SENTINEL3A	18	0.061	-0.693	27	1.496	556.877
1/8/26 9:14	SENTINEL3B	17	0.098	-0.701	24	0.640	404.552
1/14/26 9:59	SENTINEL3B	18	0.046	-0.696	42	-0.562	464.808
1/22/26 19:35	SENTINEL3B	18	0.037	-0.688	22	0.112	387.090
1/5/26 1:38	SENTINEL6A	21	0.078	-0.700	51	-1.447	300.900
1/7/26 22:56	SENTINEL6A	21	0.093	-0.760	145	-1.355	26.144
1/12/26 6:21	SENTINEL6A	16	0.011	-0.651	19	-0.259	21.720
1/14/26 5:10	SENTINEL6A	20	0.056	-0.666	29	-7.769	697.724
1/14/26 9:02	SENTINEL6A	17	0.054	-0.651	29	0.398	23.424
1/14/26 21:43	SENTINEL6A	18	0.053	-0.677	139	112.333	12912.128
1/7/26 22:57	SENTINEL6B	20	0.011	-0.739	135	-0.128	52.174
1/8/26 10:39	SENTINEL6B	19	0.038	-0.757	34	0.481	7.871
1/14/26 5:10	SENTINEL6B	19	0.090	-0.660	70	-0.509	180.749
1/14/26 7:07	SENTINEL6B	23	0.135	-0.712	50	2.944	223.298
1/14/26 9:03	SENTINEL6B	17	0.041	-0.668	55	3.403	170.673
1/14/26 21:43	SENTINEL6B	19	0.082	-0.688	22	-5.155	304.788

Start Date & Time	Satellite	Legacy RMS	Legacy Skew	Legacy Kurto	New RMS (p	New Skew	New Kurtosis
1/4/26 20:39	STARLETTE	37	0.139	-0.704	44	0.599	147.168
1/4/26 22:28	STARLETTE	22	0.086	-0.651	34	-0.385	250.788
1/5/26 0:17	STARLETTE	30	0.141	-0.638	39	-0.797	224.848
1/7/26 21:36	STARLETTE	25	0.169	-0.641	28	-0.054	81.662
1/7/26 23:26	STARLETTE	37	0.258	-0.745	40	-0.309	42.519
1/8/26 1:15	STARLETTE	23	0.084	-0.641	42	2.584	332.611
1/14/26 18:23	STARLETTE	24	0.168	-0.675	26	0.258	31.322
1/15/26 18:42	STARLETTE	23	0.118	-0.663	27	0.253	18.284
1/15/26 22:21	STARLETTE	22	0.086	-0.642	32	0.053	449.058
1/27/26 15:16	STARLETTE	22	0.127	-0.670	49	2.011	315.898
1/14/26 18:03	STELLA	24	0.167	-0.607	86	-3.179	130.578
1/14/26 21:22	STELLA	51	0.086	-0.463	199	14.379	992.056
1/7/26 23:05	SWARM-A	19	0.072	-0.701	25	1.375	47.385
1/11/26 17:43	SWOT	20	0.118	-0.655	34	1.382	247.642
1/13/26 16:05	TANDEMX	17	0.041	-0.673	18	0.099	3.244
1/14/26 15:48	TANDEMX	17	0.045	-0.667	19	0.561	22.002
1/14/26 13:45	WESTPAC	16	0.004	-0.714	137	-0.188	50.411

OrbitNP FullRate Analysis

Georg's LE Detection

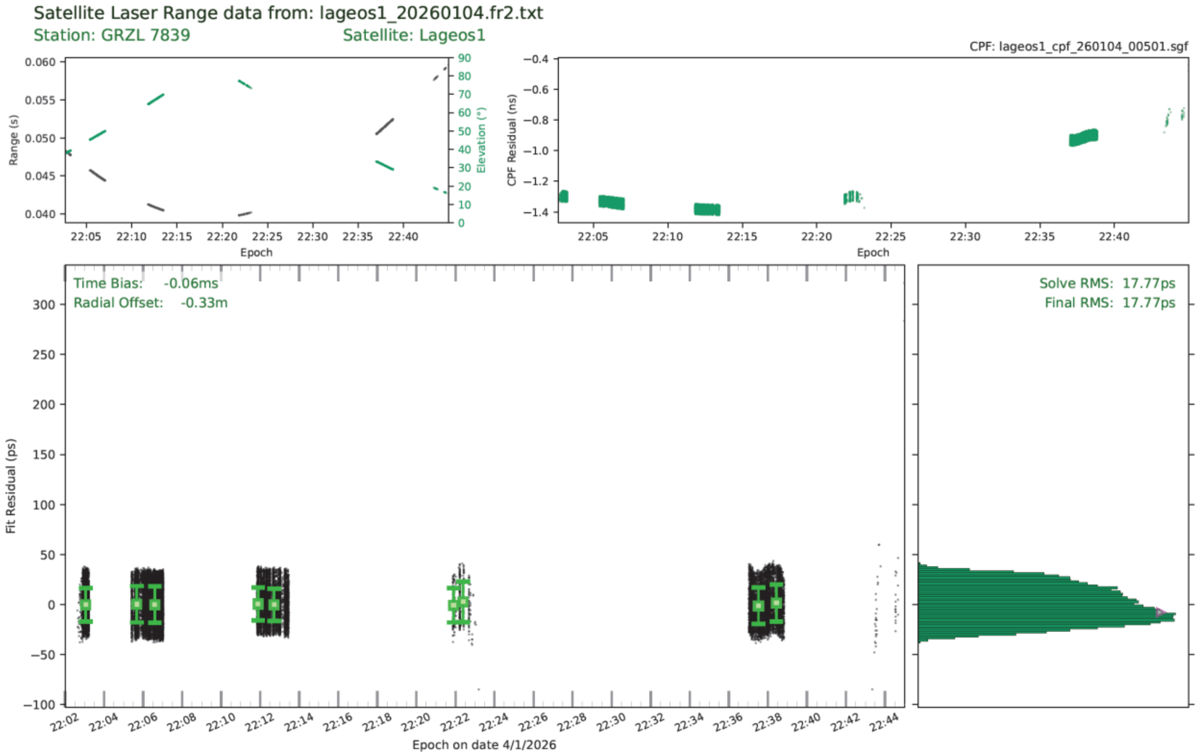

Michael's LE Detection

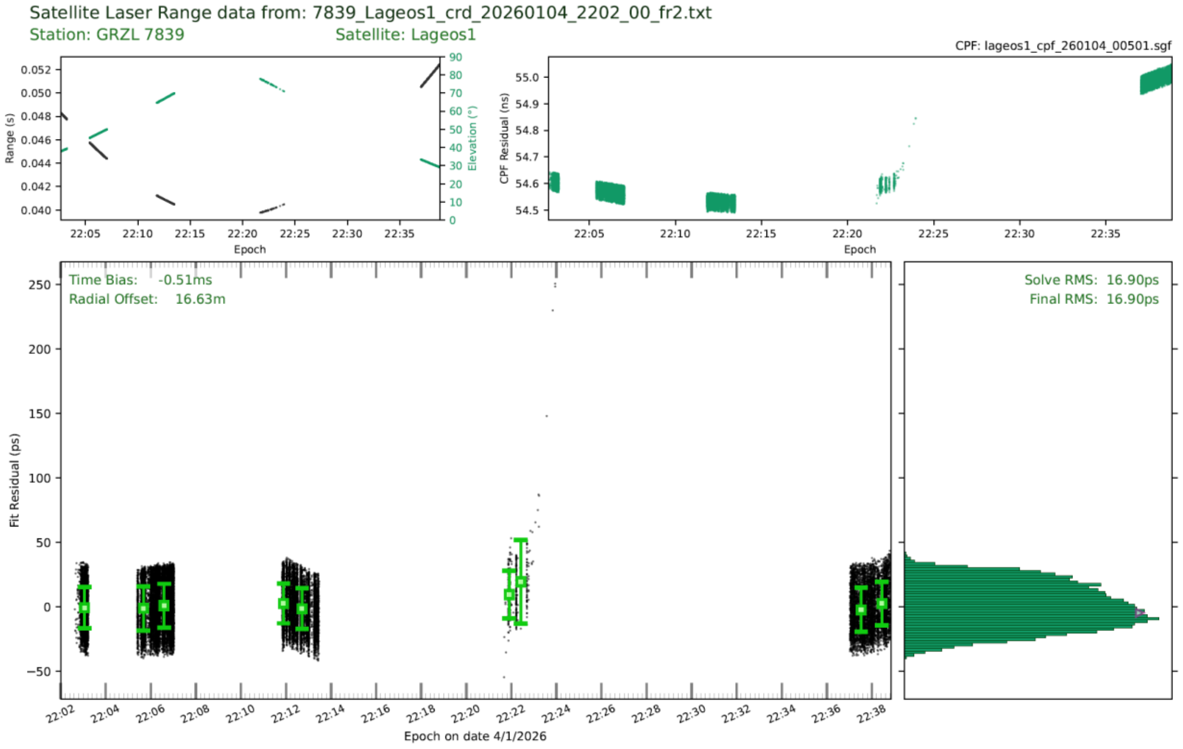

- **Michael's new cleaning approach deleted the sparse data near the end of the LAGEOS-1 pass (after 22:42)**
- **Georg's OrbitNP residuals show less trended residuals. Did the new batch cleaning by bin introduce any new systematics?**

7839 GRZL LAGEOS-1 on 4-Jan-2026 at 22:02 Analysis (FR Differences)

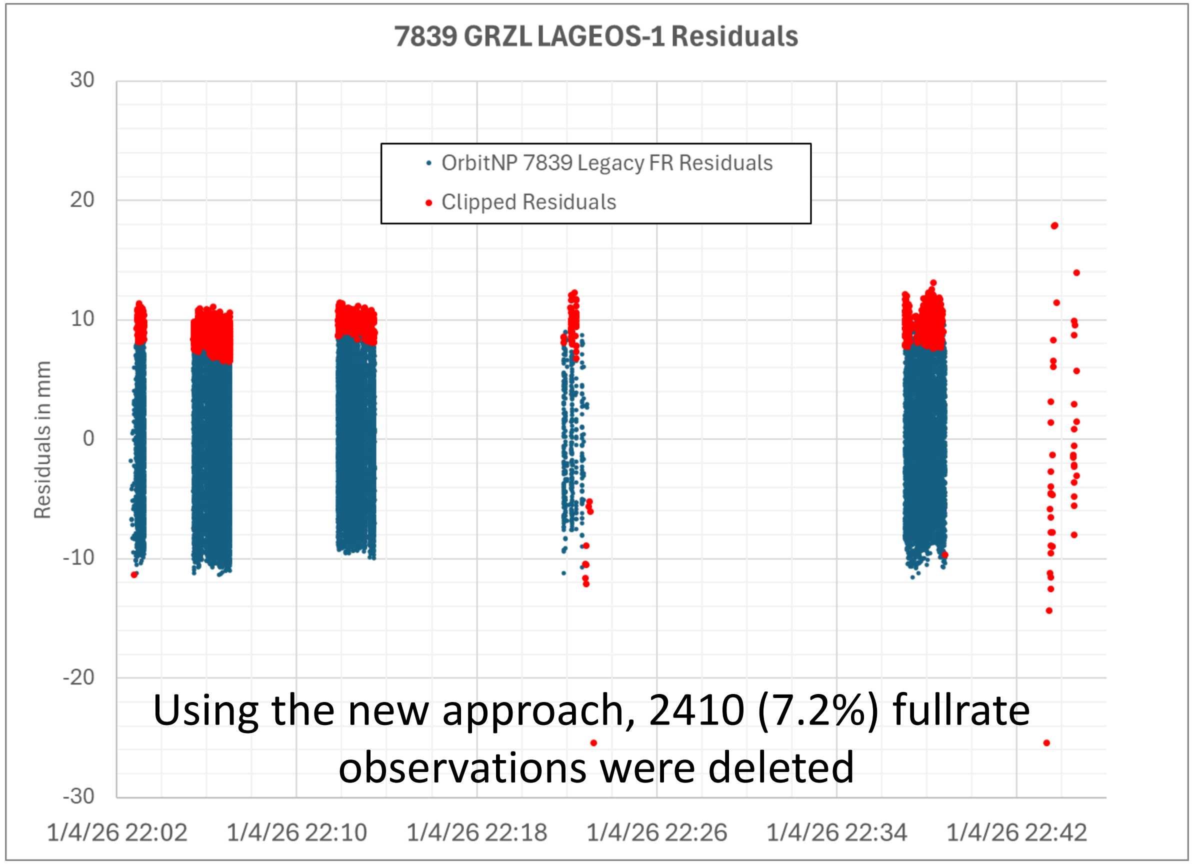

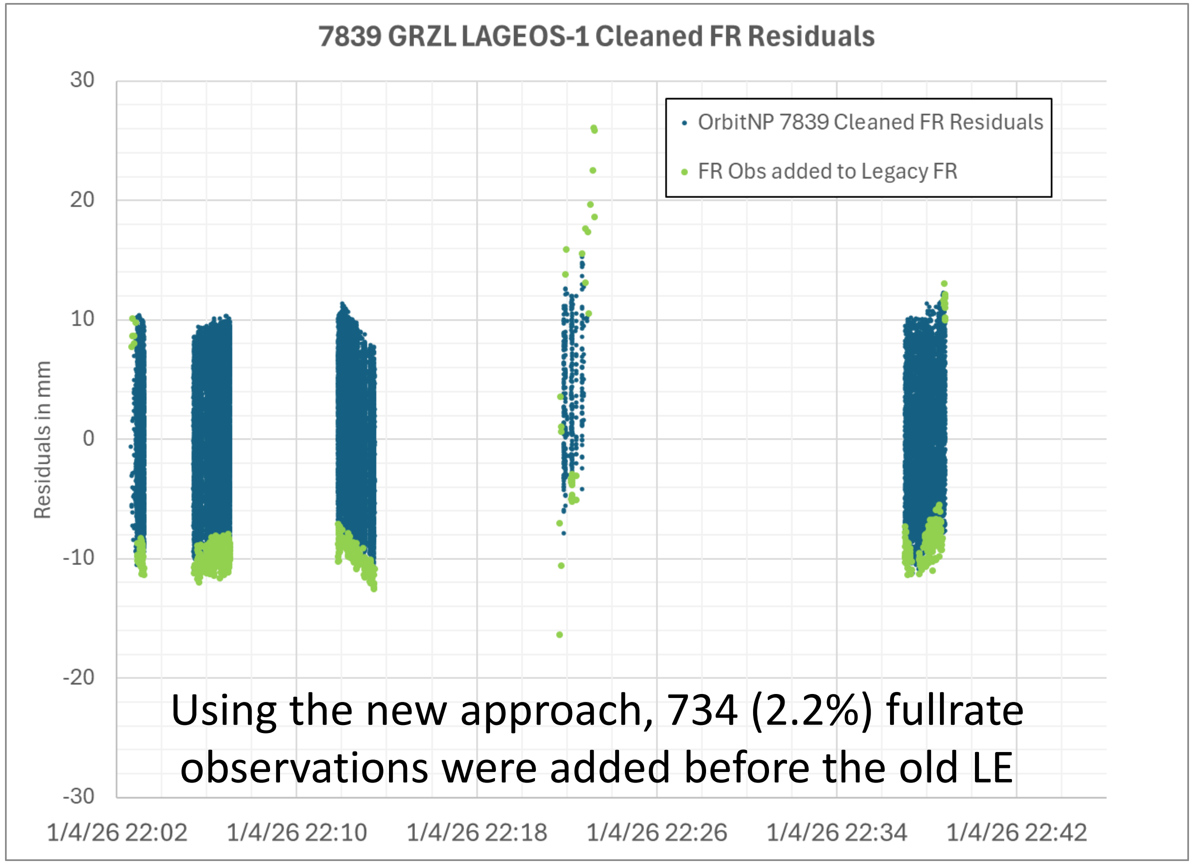

- **Michael mentioned that his new approach returns are accepted within 3 mm before and 17 mm after the LE and here is the proof**
- **The left chart are the legacy OrbitNP FR Residuals with the FR observations highlighted in red that don't exist in the new 'cleaned' FR data. The right chart are the 'Cleaned' FR residuals with the cleaned FR observation highlighted in green that didn't exist in the legacy FR data. The blue dots on both charts are the FR observations common to both the legacy and the new cleaned data filtering approach. The NP created from the new data filtering will be biased closer to the LE by 0.9 mm on this LAGEOS-1 pass**

7839 GRZL LAGEOS-1 on 4-Jan-2026 at 22:02 Analysis

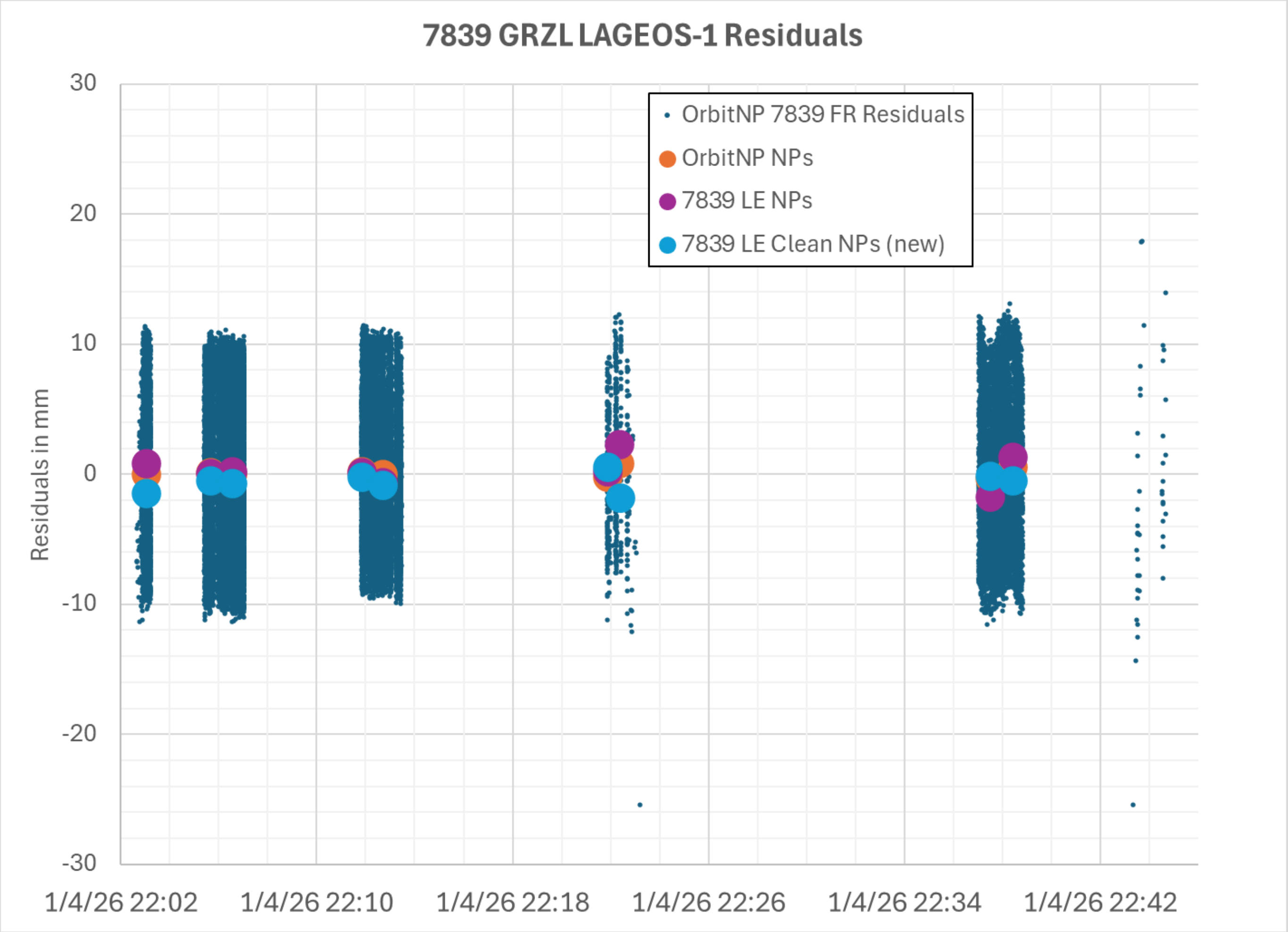

- In this chart, the dark blue dots are the OrbitNP FullRate (FR) residuals based on the existing FR data in the Data Centers (i.e. Georg's LE algorithm)
- The large orange circles are the OrbitNP Normal Points (NP) produced from the 7839 GRZL FR data. The large purple circles are the existing NP data in the Data Centers. The light blue circles are the NPs produced from the new 'clean' editing approach after removing a small system delay offset between the old and new data filtering approaches
- The new data filtering approach creates NPs that are slightly closer (~0.9 mm) to the LAGEOS-1 LE
- Note: No NPs were created in the sparse amount of FR data in the last two NP bins by the either the legacy or the new LE data filtering technique

7839 GRZL LAGEOS-1 on 4-Jan-2026 at 22:02 Analysis (Legacy NP Differences)

Source	Rec Type	Epoch	ToF	cfg1	np ind	bin size	Obs	RMS	Skew	Kurtosis	P-M	Return Rate	ToF Diff in mm	P-M Diff in mm
7839 LE NP	11	79383.596663897	0.047913562019	902	2	120	3386	33.4	0.130	-0.886	0.0	1.4		
OrbitNP NPs	11	79383.596663897	0.047913562013	902	2	120	3386	33.6	0.141	-0.845	-3.4	4.8	0.90	0.51
7839 LE NP	11	79540.450563895	0.045513675346	902	2	120	3150	36.1	0.059	-1.154	-23.4	1.3		
OrbitNP NPs	11	79540.450563895	0.045513675347	902	2	120	3150	36.3	0.064	-1.131	-20.5	4.3	-0.15	-0.43
7839 LE NP	11	79595.770863895	0.044740173107	902	2	120	11179	36.2	0.050	-1.133	-20.9	4.7		
OrbitNP NPs	11	79595.770863895	0.044740173106	902	2	120	11179	36.4	0.076	-1.128	-19.5	9	0.15	-0.21
7839 LE NP	11	79913.326063895	0.041199342996	902	2	120	1497	33.2	0.249	-0.793	-6.6	0.6		
OrbitNP NPs	11	79913.326063895	0.041199342997	902	2	120	1497	33.3	0.259	-0.782	-9.1	7.2	-0.15	0.37
7839 LE NP	11	79962.729963892	0.040805574265	902	2	120	7355	32.2	0.199	-0.842	-15.8	3.1		
OrbitNP NPs	11	79962.729963892	0.040805574269	902	2	120	7355	32.3	0.213	-0.785	-5.8	4.2	-0.60	-1.50
7839 LE NP	11	80514.163063887	0.039821288328	902	2	120	134	34.2	0.053	-1.162	-28.4	0.1		
OrbitNP NPs	11	80514.163063887	0.039821288325	902	2	120	134	34.1	0.048	-1.147	1.9	1.4	0.45	-4.54
7839 LE NP	11	80543.288063895	0.039948923644	902	2	120	273	38.3	0.059	-1.238	-31.7	0.1		
OrbitNP NPs	11	80543.288063895	0.039948923634	902	2	120	273	40.8	-0.145	-0.097	-24.5	0.2	1.50	-1.08
7839 LE NP	11	81451.404863887	0.051049548010	902	2	120	3574	35.7	0.226	-1.016	-22.1	1.5		
OrbitNP NPs	11	81451.404863887	0.051049548020	902	2	120	3574	36.3	0.246	-0.953	-19.7	3.1	-1.50	-0.36
7839 LE NP	11	81506.350463895	0.052034612347	902	2	120	2825	36.9	0.198	-1.064	-21.5	1.2		
OrbitNP NPs	11	81506.350463895	0.052034612342	902	2	120	2825	37.1	0.223	-0.973	-17.5	2.8	0.75	-0.60
												AVG	0.15	

- **Line-by-Line comparison of the OrbitNP generated NPs from the legacy FR data compared to the legacy generated NPs. The individual Time of Flight (ToF) differences are <=10 ps/1.5 mm with an average offset of 1 ps/0.15 mm**

7839 GRZL LAGEOS-1 on 4-Jan-2026 at 22:02 Analysis (Cleaned NP Differences)

Source	Rec Type	Epoch	ToF	cfg	np ind	bin size	Obs	RMS	Skew	Kurtosis	P-M	Return Rate	ToF Diff in mm	P-M Diff in mm
Clean 7839 NPs	11	79383.567663890	0.047914031514	902	2	120	3299	32	0.003	2.102	-0.2	1.4		
OrbitNP Clean 7839 NPs	11	79383.567663890	0.047914143350	902	2	120	3299	32.2	0.005	-0.863	-0.1	4.7	-1.50	-0.01
Clean 7839 NPs	11	79540.463163897	0.045513494551	902	2	120	2955	33.9	-0.003	1.923	1.2	1.2		
OrbitNP Clean 7839 NPs	11	79540.463163897	0.045513606378	902	2	120	2955	34.2	0.009	-1.051	-15.1	4.1	-0.15	2.44
Clean 7839 NPs	11	79595.620863897	0.044742214475	902	2	120	10342	33.7	0.014	1.990	1.4	4.3		
OrbitNP Clean 7839 NPs	11	79595.620863897	0.044742326301	902	2	120	10342	33.9	0.013	-0.984	-12.0	8.4	0.00	2.01
Clean 7839 NPs	11	79913.326063895	0.041199342990	902	2	120	1432	30.6	0.041	2.167	-0.6	0.6		
OrbitNP Clean 7839 NPs	11	79913.326063895	0.041199454815	902	2	120	1432	30.7	0.042	-0.829	-4.3	6.9	0.15	0.55
Clean 7839 NPs	11	79962.729963892	0.040805574260	902	2	120	7173	30.6	0.040	2.169	-0.6	3		
OrbitNP Clean 7839 NPs	11	79962.729963892	0.040805686089	902	2	120	7173	31.4	0.068	-0.771	-3.0	4.1	-0.45	0.36
Clean 7839 NPs	11	80514.163063887	0.039821288327	902	2	120	139	35.2	-0.008	1.887	2.4	0.1		
OrbitNP Clean 7839 NPs	11	80514.163063887	0.039821400146	902	2	120	139	36.8	-0.188	-0.069	-14.4	0.4	1.05	2.52
Clean 7839 NPs	11	80545.255563892	0.039958178011	902	2	120	247	33	0.191	1.898	0.0	0.1		
OrbitNP Clean 7839 NPs	11	80545.255563892	0.039958289852	902	2	120	247	64.8	4.290	26.218	-26.2	0.1	-2.25	3.93
Clean 7839 NPs	11	81451.342263900	0.051048438653	902	2	120	3461	33.9	0.185	2.017	-4.6	1.4		
OrbitNP Clean 7839 NPs	11	81451.342263900	0.051048550472	902	2	120	3461	34.3	0.175	-0.952	-16.7	3	1.05	1.81
Clean 7839 NPs	11	81506.712663887	0.052041178811	902	2	120	2648	33.4	0.092	2.010	-1.7	1.1		
OrbitNP Clean 7839 NPs	11	81506.712663887	0.052041290633	902	2	120	2648	33.8	0.108	-0.919	-12.3	2.6	0.60	1.59
												AVG	-0.17	1.69

- **Line-by-Line comparison of the OrbitNP generated NPs from the cleaned FR data compared to the cleaned generated NPs after applying the system delay to the cleaned FR data. The individual Time of Flight (ToF) differences are <15 ps/2.25 mm with an average offset of ~1 ps/0.15 mm.**

Summary/Conclusions/Questions

- There are some CRD formatting issues that need to be corrected, which are simple fixes
- The Peak minus Mean Algorithms are different between the old and new algorithms and yield different results on LAGEOS class satellites. Georg's old P-M algorithm is in better agreement with OrbitNP P-M algorithm
- The new LE approach is biased more toward the LE than before. Does this require a new CoM correction?
- Biggest concerns are
  - the batching approach is in violation of the Herstmonceux NP algorithm,
  - does this new batching approach introduce any systematics? and
  - 14% of all passes have higher session RMSs and 30% of LARES-2 passes
- No detailed analysis of GNSS or altimetric satellites was performed
- Should we give Michael a green light to implement his new screening approach? Or
- When any station introduces a new data screening approach, should the station be placed in quarantine and should they provide data in the old and new approach?

Evolution of ILRS Barometric Pressure Quality Control (QC); Incorporation of VMF3o data in Barometric QC; Meteorological Data Processing and Data Handling from Cradle to Grave

Van S. Husson, Mary Fenno, Sean Mayer

vhusson@peraton.com, mary.fenno@peraton.com, smayer@peraton.com

ILRS Quality Control Board

18-Mar-2026

Peraton

Systematic Error Trends as a Function of Time

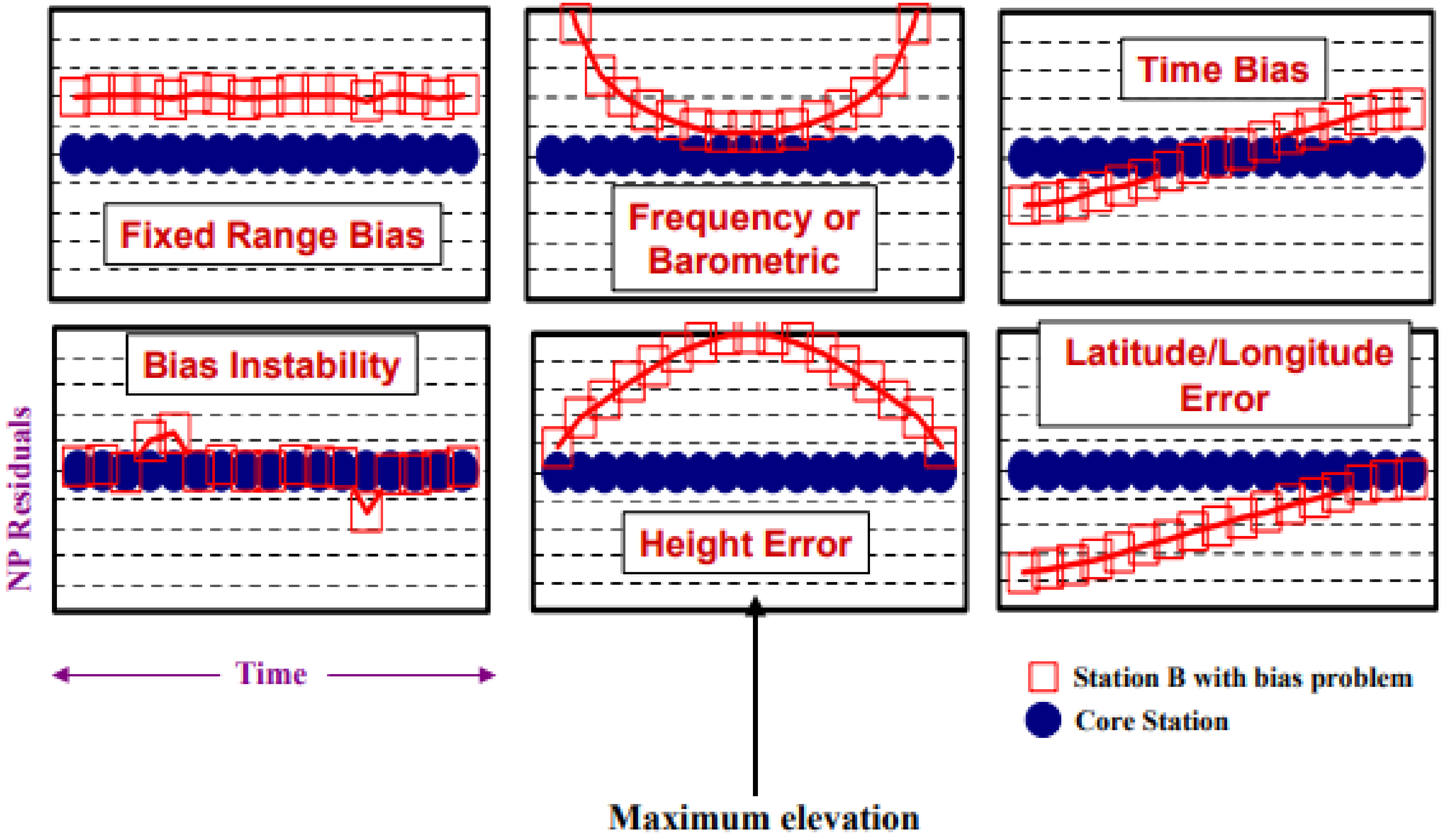

- **Source: Graham generated this graphic for our joint paper on "System Performance Assessment from NERC Simultaneous Arc Analysis" for the 2000 International Workshop in Matera**
- **Elevation dependent errors:**
  - a station height error
  - a station frequency error
  - a station barometric error
- **Epoch errors are range-rate dependent**
- **A station horizontal position error will be azimuth and elevation dependent**

Systematic Errors as a Function of Elevation Angle

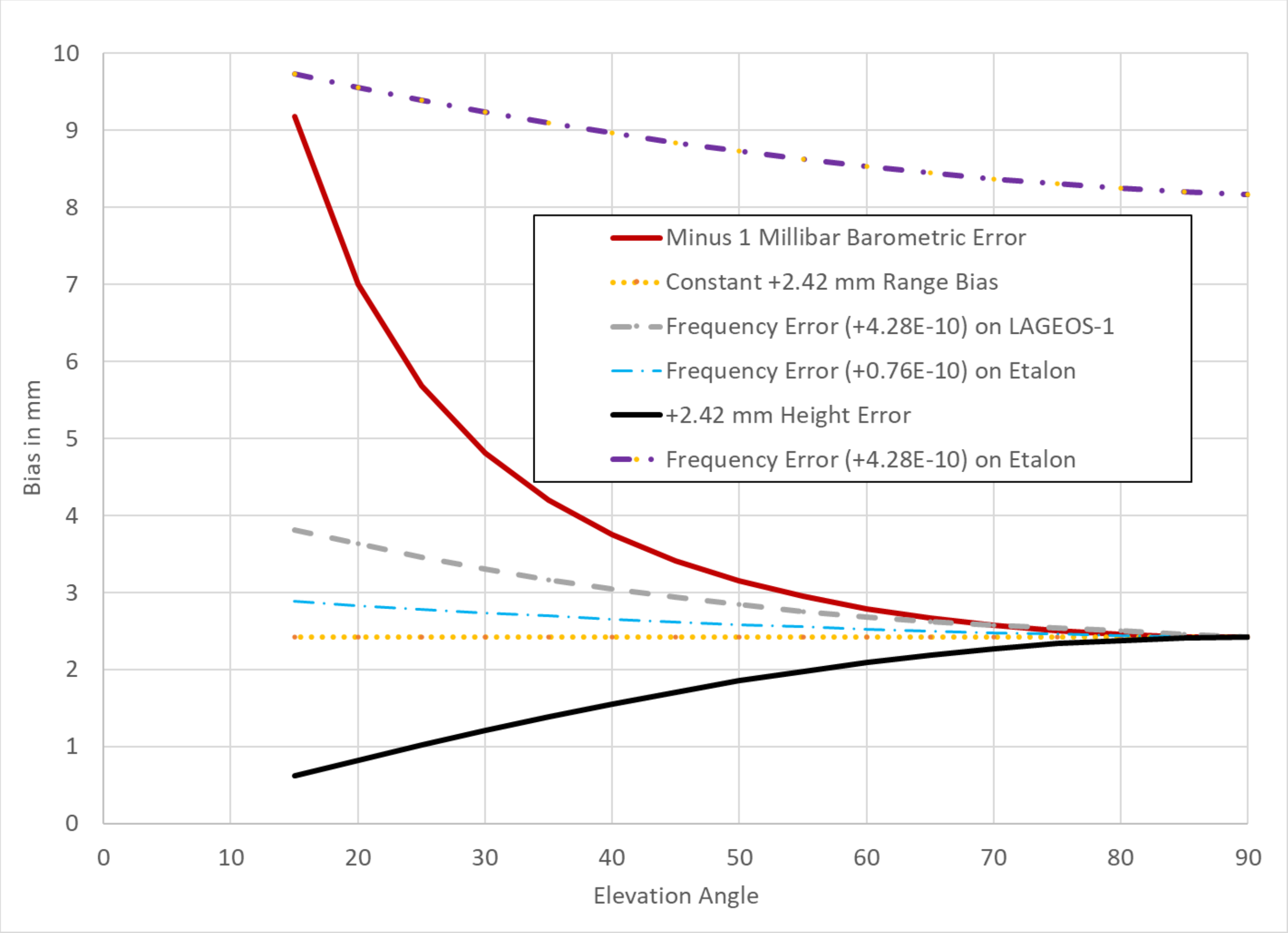

- **The following systematic errors will induce a 2.42 mm range bias at zenith**
  - Plus 2.42 mm fixed range bias
  - Minus 1 mbar pressure error
  - Plus 2.42 mm station coordinate height error
  - 4.28 E-10 frequency error on LAGEOS-1
  - 0.76 E-10 frequency error on Etalon
- **A frequency error is range dependent NOT elevation dependent and why a frequency error of 4.28 E-10 is shown for Etalon**
- **Epoch errors (aka time biases) and station coordinate horizontal errors are NOT elevation dependent, but are pass geometry dependent**
- **The impact of barometric error is the most non-linear**

Evolution of ILRS Barometric Pressure Quality Control

1990's Barometric Quality Control (QC)

- **In the 1990's, barometric QC checks were limited**
- **Individual sites did report issues with their barometric measurements and provide barometric corrections (if recoverable)**
  - NASA SLR stations 7080, 7105, 7109, 7110, and 7210 reported issues and are documented on the ILRS website at https://ilrs.gsfc.nasa.gov/network/site_information/slr_problems_text.html
  - If known barometric errors could not be removed by reprocessing the data, then the corrections were incorporated into the ILRS Data Handling File (DHF)

Early 2000's Barometric QC Technique to Detect Discontinuities

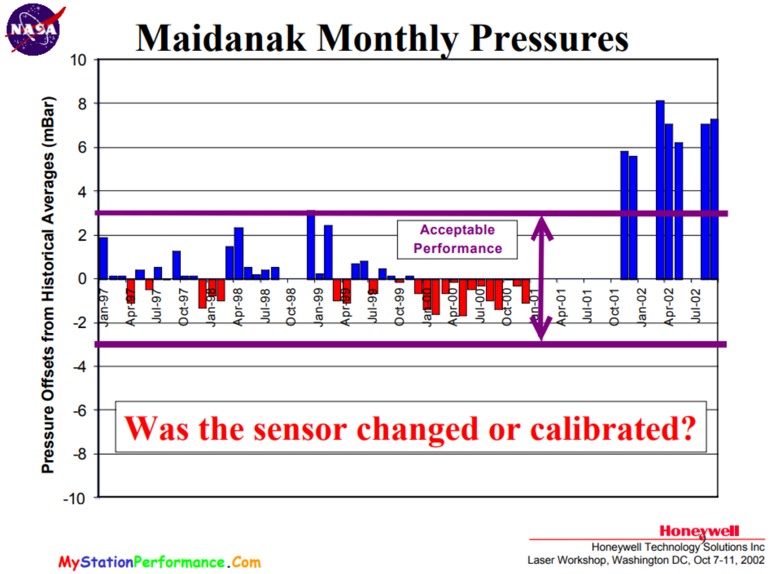

Shanghai 7837 Pressure Analysis

Seasonal

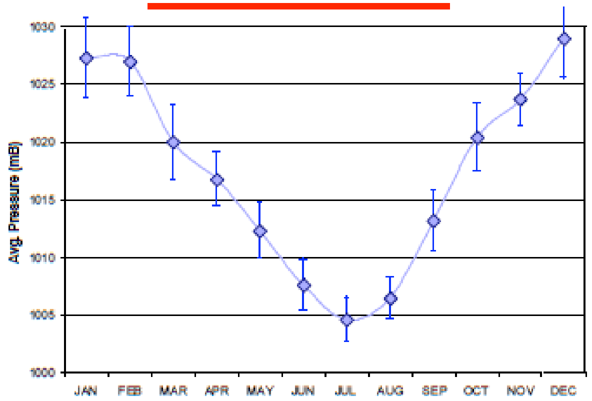

Aggregate OMCs

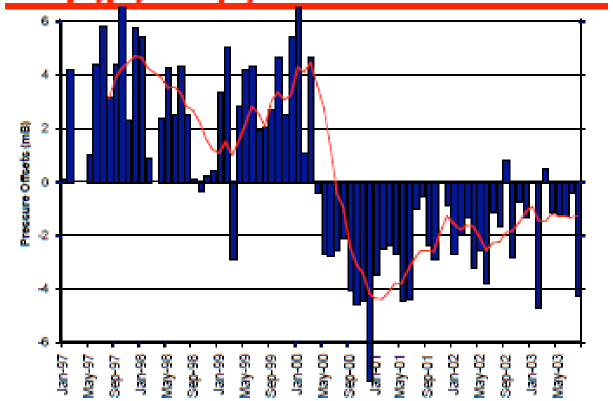

- ❑ Some SLR sites have repeatable seasonal fluctuations in barometric pressures. Asian sites have the largest seasonal barometric pressure variations exceeding 25 mBars. Removing the seasonal trends helps identify discontinuities in the pressures
- ❑ The top chart is barometric pressure analysis of the legacy Maidanak system, 1864, presented at the 2002 International Workshop in Washington, DC
- ❑ The bottom two charts were the barometric pressure analysis of the legacy Shanghai system, 7837, which were presented during Session 18 of the 2003 ILRS Technical Workshop in Kötzting, Germany
- ❑ These are two examples where a barometric sensor change induced a discontinuity

2000 to 2020 Barometric QC

- **Some SLR sites installed a secondary barometric sensor to compare the values. Some barometric sensors were 3 in 1**
- **Sites would perform regular barometric sensor calibrations**
- **In April 2019, barometric pressure data integrity checks were implemented as part of Automatic CRD Quality Control (AutoQC) to catch obvious blunders**
- **These barometric AutoQC checks were not site specific**
  - The lower and upper limits were 700 and 1100 mBars; respectively, and the failure rate was near zero

Gross Barometric Measurement Errors in Legacy SLR Data

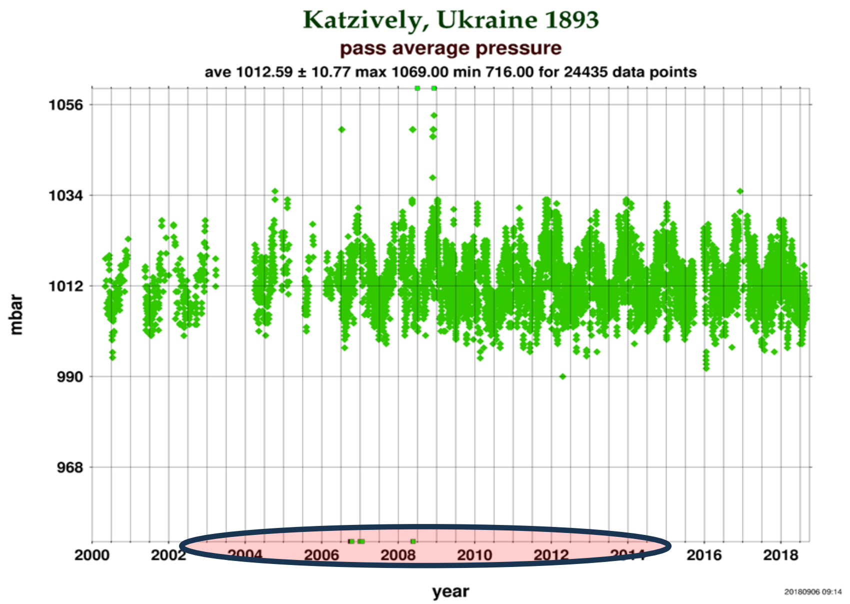

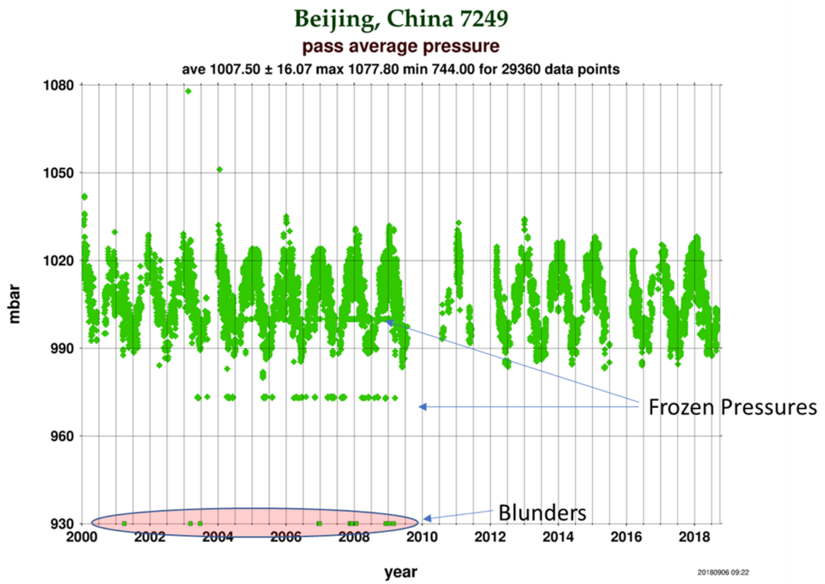

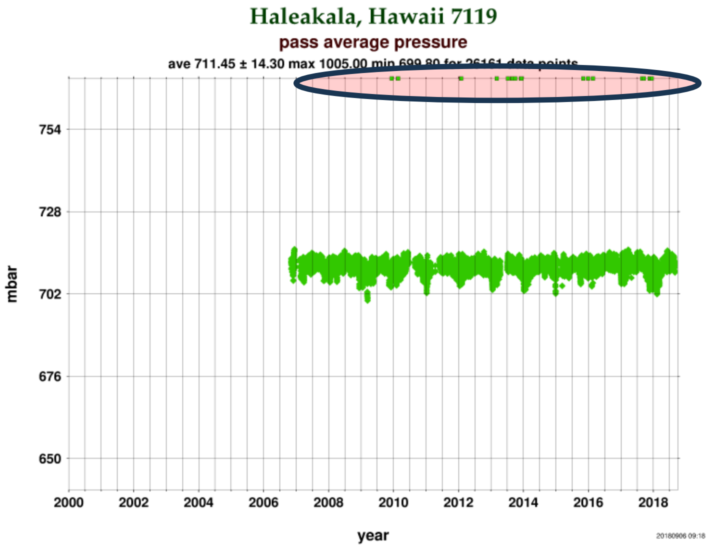

- ❑ These charts are a time series of the pass-by-pass barometric pressure measurements from a legacy version of the station pages on the ILRS website
- ❑ Interface issue between the barometric sensor and the tracking computer can cause outliers and frozen measurements highlighted here
- ❑ **These obvious blunders still escaped the April 2019 AutoQC barometric data integrity checks**

2020's Barometric Data Integrity Checks

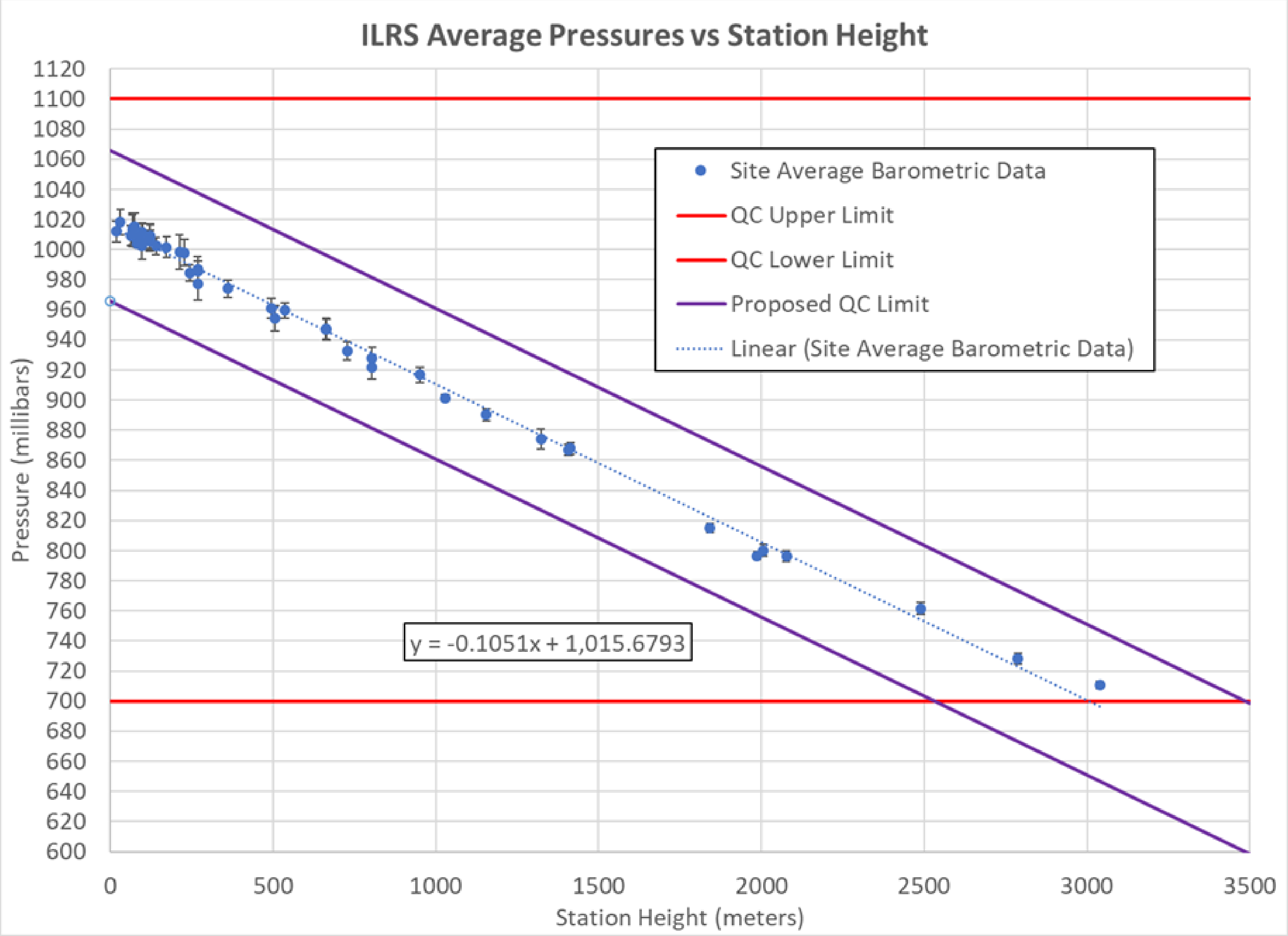

- ❑ **At the June 2021 ILRS CB meeting, more restrictive barometric data integrity checks (+/- 50 mBars) based on the station's height (i.e. height above the ellipsoid) were recommended; were later approved and implemented**
- ❑ **Some, but not all, of the visually obvious errors on the previous slide would have been caught with these new more restrictive limits**

What new algorithms can we develop to identify barometric errors?

- **Can we develop an algorithm to identify frozen barometric measurements?**
- **Can we develop an algorithm to identify inexplicable jumps in the barometric measurements within a pass?**
- **Can we utilize the Vienna Mapping Function for optical wavelengths (VMF3o) to aid in our barometric AutoQC?**
  - Using the VMF3o data, can we develop a more restrictive algorithm than +/- 50 mBars?
  - Using the VMF3o data, can we develop an algorithm to identify small discontinuities (i.e. several tenths of a mBar) in the measurements?
  - Using the VMF3o data, can we develop an algorithm to identify small linear drifts (i.e. 0.15 mBars/year) in the measurements?

Frozen Pressure Detection Algorithm

- **At the March 2025 ILRS Central Bureau Meeting, an algorithm was presented to detect frozen barometric pressures**
- **Below is the algorithm:**
  - Prerequisite: Store at least one CRD 20 Meteorological for each pass to a relational database (VMF3o data not required)
  - Step 1: For each SLR station, compute the average pressure and temperature for every six-hour period (0, 6, 12 and 18) along with their standard deviations and store the results (Additional benefit: Enables direct comparison to VMF3o data which has a temporal resolution of 6 hours)
  - Step 2: For each station, query the step 1 results and bring back a match for any two consecutive six-hour periods where the following are all true
    - The pressures are identical;
    - There are more than 1 pass segment in each six-hour period; and
    - The standard deviation of pressures in the two consecutive six-hour periods is zero (i.e. no change in the measurement)

Frozen Meteorological Data Example from 1889 ZELL

pad	sat	start date & time	pressure (mbar)	temp (K)	hum (%)
1889	STRL	1/24/2023 11:37	896.2	281.4	28
1889	LAG1	1/24/2023 12:51	896.3	280.6	35
1889	STRL	1/24/2023 13:25	896.3	280.6	35
1889	LARS	1/24/2023 15:05	896.3	280.6	35
1889	STRL	1/24/2023 15:13	896.3	280.6	35
1889	LAG2	1/24/2023 15:21	896.3	280.6	35
1889	AJI1	1/24/2023 15:56	896.3	280.6	35
1889	LAG1	1/24/2023 16:11	896.3	280.6	35
1889	STEL	1/24/2023 16:38	896.3	280.6	35
1889	LARS	1/24/2023 17:02	896.3	280.6	35
1889	LAG2	1/24/2023 19:39	896.3	280.6	35
1889	LAG1	1/24/2023 19:57	896.3	280.6	35
1889	STRL	1/24/2023 20:42	896.3	280.6	35
1889	AJI1	1/24/2023 22:03	895.3	271.9	47
1889	AJI1	1/25/2023 23:13	892.9	271.1	41
1889	STEL	1/26/2023 4:24	893.1	270.4	36
1889	LAG1	1/26/2023 10:25	892.3	279.4	22
1889	LAG2	1/26/2023 11:25	892.3	279.4	22
1889	STRL	1/26/2023 12:11	892.3	279.4	22
1889	LAG1	1/26/2023 13:39	892.3	279.4	22
1889	STRL	1/26/2023 14:06	892.3	279.4	22
1889	AJI1	1/26/2023 14:11	892.3	279.4	22
1889	LARS	1/26/2023 14:56	892.3	279.4	22
1889	LAG2	1/26/2023 15:11	892.3	279.4	22
1889	STRL	1/26/2023 15:50	892.3	279.4	22
1889	AJI1	1/26/2023 16:11	892.3	279.4	22
1889	LARS	1/26/2023 16:51	892.3	279.4	22
1889	LAG1	1/26/2023 17:05	892.3	279.4	22
1889	STRL	1/26/2023 17:41	892.3	279.4	22
1889	AJI1	1/26/2023 18:15	892.3	279.4	22
1889	LAG2	1/26/2023 19:13	891.4	270.8	50

8 hours

8 hours

- **The current AutoQC algorithm will not flag this issue because the pressures are in the reasonable range of expected values**
- **Did a change in the operators resolve the issue?**
- **Do other stations have this issue?**

Potential Number of Occurrences of Frozen Pressures (1-Jan-2024 to 31-Jan-2026)

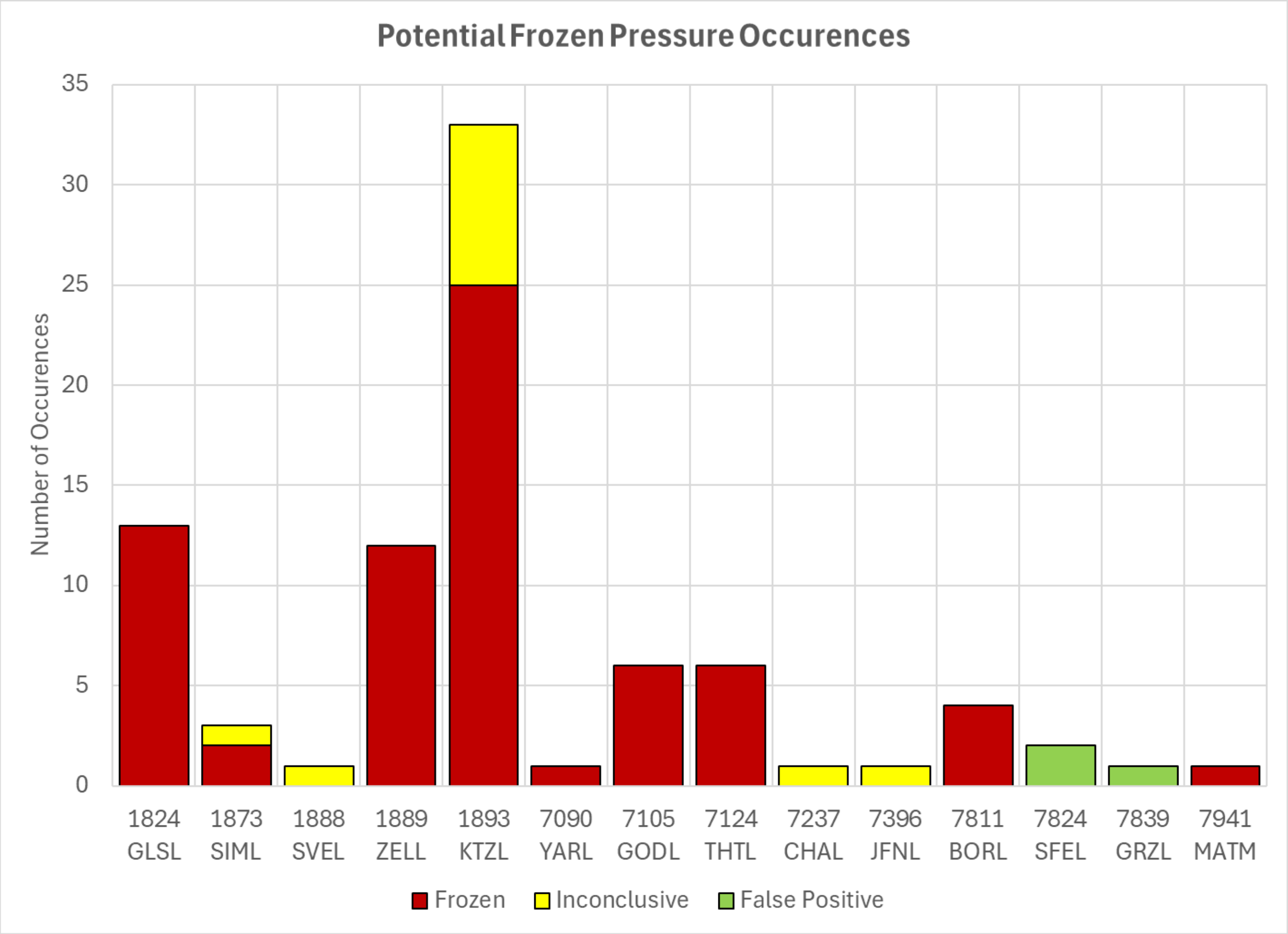

- **When the pressures were frozen, most of the time the temperatures were also frozen**
- **Incorrect temperatures influence the system delay calculations which are calibration target range dependent**
- ***Note: The resolution of the 1893 KTZL barometric measurements were 1 mBar making it difficult to tell if the pressures were changing***
- **Very few false positives and inconclusives**

Inexplicable Barometric Jump Detection Algorithm

- **Starting on 8-Apr-2025, as a process improvement, the NASA SLR DOC began to store every CRD NP 20 meteorological record to a relational database; a prerequisite for a new algorithm to detect inexplicable jumps in barometric pressures within a CRD**
- **Below is the algorithm**
  - Query every CRD where the peak-to-peak pressure variation is more than a TBD amount and the time span of the 20 meteorological records is less than TBD minutes
  - For LEO and MEO satellites, the best TBD values appear to be 2 mBars and 60 minutes to minimize false alarms. For HEO satellites, the best TBD values appear to be 4 mBars and 480 minutes (8 hours) to minimize false alarms

Algorithm Results

Pad	Satellite	Date and start time YYYY-MM-DD HH:MM:SS	Wave	Pres Var	Minute	# Met
7249	COMPI3	2026-02-05 12:45:00	532.0	3.49	328.43	109
7825	GALILEO220	2025-07-13 09:14:00	532.1	3.35	383.50	3
7825	GALILEO203	2025-08-18 06:34:00	532.1	3.10	273.17	3
7827	BEIDOU3M17	2025-10-30 12:01:00	849.8	3.12	324.22	3
7839	GALILEO208	2025-05-19 14:44:00	532.0	3.24	280.52	2
7839	GALILEO227	2025-10-24 03:47:00	532.0	3.74	216.05	2
7839	GALILEO221	2025-11-23 17:04:00	532.0	3.06	284.72	2
7840	GALILEO213	2025-04-11 23:11:00	532.0	3.70	318.10	61
7840	GALILEO208	2025-09-04 17:39:00	532.0	3.22	216.00	41
7840	GALILEO201	2025-09-04 22:07:00	532.0	3.08	227.95	43
7840	GALILEO224	2025-10-29 21:52:00	532.0	3.63	246.08	46
7840	GALILEO227	2025-11-17 07:53:00	532.0	3.31	264.08	49
7840	GALILEO204	2026-02-16 17:34:00	532.0	3.93	238.03	47
7840	GALILEO102	2026-03-02 15:26:00	532.0	3.02	338.98	66
7840	GALILEO102	2026-03-02 15:26:00	532.0	3.02	338.98	66
1893	STARLETTE	2025-08-22 19:55:00	532.0	5.00	9.07	2
7838	GRACE-FO2	2025-08-17 21:01:00	532.0	9.60	1.28	13
7941	HY-2D	2025-05-07 10:55:00	532.0	4.80	2.05	4

- **Here are the results where the TBD values were 3 mBars and 480 minutes (8 hours) for barometric pressure variation and time span of the 20 Meteorological records; respectively**
- **Notice the barometric pressures can change by more 3 mBars during a GNSS pass**
- **The last 3 passes are from LEO CRDs which do have inexplicable barometric changes**

Inexplicable Jumps in Barometric Pressure

station	satellite	YYYY-MM-DD	Seconds of Day	Pressure (mBar)	Hum (%)	Temp (K)
7838	GRACE-FO1	2025-08-17	75580	1009.5000	78	300.4
7838	GRACE-FO1	2025-08-17	75583	1009.5000	78	300.4
7838	GRACE-FO1	2025-08-17	75585	1009.5000	78	300.4
7838	GRACE-FO1	2025-08-17	75594	1009.5000	78	300.4
7838	GRACE-FO1	2025-08-17	75608	1009.5000	77	300.4
7838	GRACE-FO1	2025-08-17	75617	1009.5000	77	300.4
7838	GRACE-FO1	2025-08-17	75623	1009.5000	77	300.4
7838	GRACE-FO1	2025-08-17	75626	1009.5000	77	300.4
7838	GRACE-FO1	2025-08-17	75632	1009.5000	77	300.4
7838	GRACE-FO1	2025-08-17	75639	1009.5000	77	300.4
7838	GRACE-FO1	2025-08-17	75649	1009.5000	77	300.4
7838	GRACE-FO1	2025-08-17	75653	1009.5000	77	300.4
7838	GRACE-FO2	2025-08-17	75695	1019.5000	78	300.4
7838	GRACE-FO2	2025-08-17	75697	1019.5000	78	300.4
7838	GRACE-FO2	2025-08-17	75713	1019.5000	78	300.4
7838	GRACE-FO2	2025-08-17	75717	1019.5000	78	300.4
7838	GRACE-FO2	2025-08-17	75723	1009.9000	78	300.4
7838	GRACE-FO2	2025-08-17	75727	1009.9000	78	300.4
7838	GRACE-FO2	2025-08-17	75735	1009.9000	78	300.4
7838	GRACE-FO2	2025-08-17	75738	1009.9000	78	300.4
7838	GRACE-FO2	2025-08-17	75741	1009.9000	78	300.4

- **Simosato (7838) was tracking both Grace follow-on satellites and the barometric pressures jumped twice by 10 mBars in 42 seconds and 6 seconds; respectively**
- **This issue would not be flagged by the current AutoQC algorithm**

Inexplicable Jumps in Barometric Pressure

Pad	Satellite	YYYY-MM-DD	Secs	Wave	R	Pressure	Hum	Temp
7941	SENTINEL6A	2025-05-07	36899	532	0	956.62	89	294.0
7941	SENTINEL6A	2025-05-07	37086	532	0	956.62	89	294.3
7941	SENTINEL6A	2025-05-07	37117	532	0	956.62	89	294.5
7941	SENTINEL6A	2025-05-07	37141	532	0	956.62	89	294.7
7941	SENTINEL6A	2025-05-07	37179	532	0	956.62	89	294.9
7941	SENTINEL6A	2025-05-07	37236	532	0	956.62	89	295.1
7941	SENTINEL6A	2025-05-07	37456	532	0	956.62	89	294.9
7941	SWOT	2025-05-07	37980	532	0	956.62	89	294.5
7941	SWOT	2025-05-07	38021	532	0	956.62	89	294.3
7941	HY-2D	2025-05-07	39353	532	0	956.32	89	294.3
7941	HY-2D	2025-05-07	39376	532	0	956.32	89	294.5
7941	HY-2D	2025-05-07	39401	532	0	956.32	89	294.7
7941	HY-2D	2025-05-07	39476	532	0	961.12	89	285.3
7941	LAGEOS-2	2025-05-08	2399	532	0	953.82	68	286.8
7941	SENTINEL6A	2025-05-08	2982	532	0	954.02	68	286.7
7941	SENTINEL6A	2025-05-08	3188	532	0	954.02	68	286.9
7941	LAGEOS-2	2025-05-08	3999	532	0	954.22	66	287.0

- **Matera (7941) was tracking HY-2D and the very last 20 record, the pressure changed by 4.8 mbars in 75 seconds**
- **The current AutoQC algorithm will not identify these inexplicable barometric jumps**

Incorporation of VMF3o data in Barometric Quality Control?

Vienna Mapping Function for Optical Frequencies (VMF3o)

- **In 2017, the Vienna Mapping Function for optical wavelengths (VMF3o) was developed (ref: DOI:10.1007/s00190-020-01385-5).There are 3 categories of VMF3o data**
  - VMF3o_EI: European Centre for Medium-Range Weather Forecast (ECMWF) ERA-Interim Numerical Weather Models (NWM) data
    - Time Span: January 1, 1990, to August 31, 2019 (the most accurate VMF3o data)
  - VMF3o_FC: ECMWF forecasted NWM
    - Time span: January 1, 2019, to present
  - VMF3o_OP: ECMWF operational NWM. Data is available next day
    - Time Span: January 1, 2008, to present
- **VMF3o data has a temporal resolution of 6 hours and exists for every ILRS site**
- **The original VMF3o time series was based on ‘approximate’ site heights**
- **All three VMF3o time series were updated in August 2025 based on more accurate SLR station heights and the addition of newer SLR sites**

Comparisons of the Old and New versions of VMF3o data by SLR station

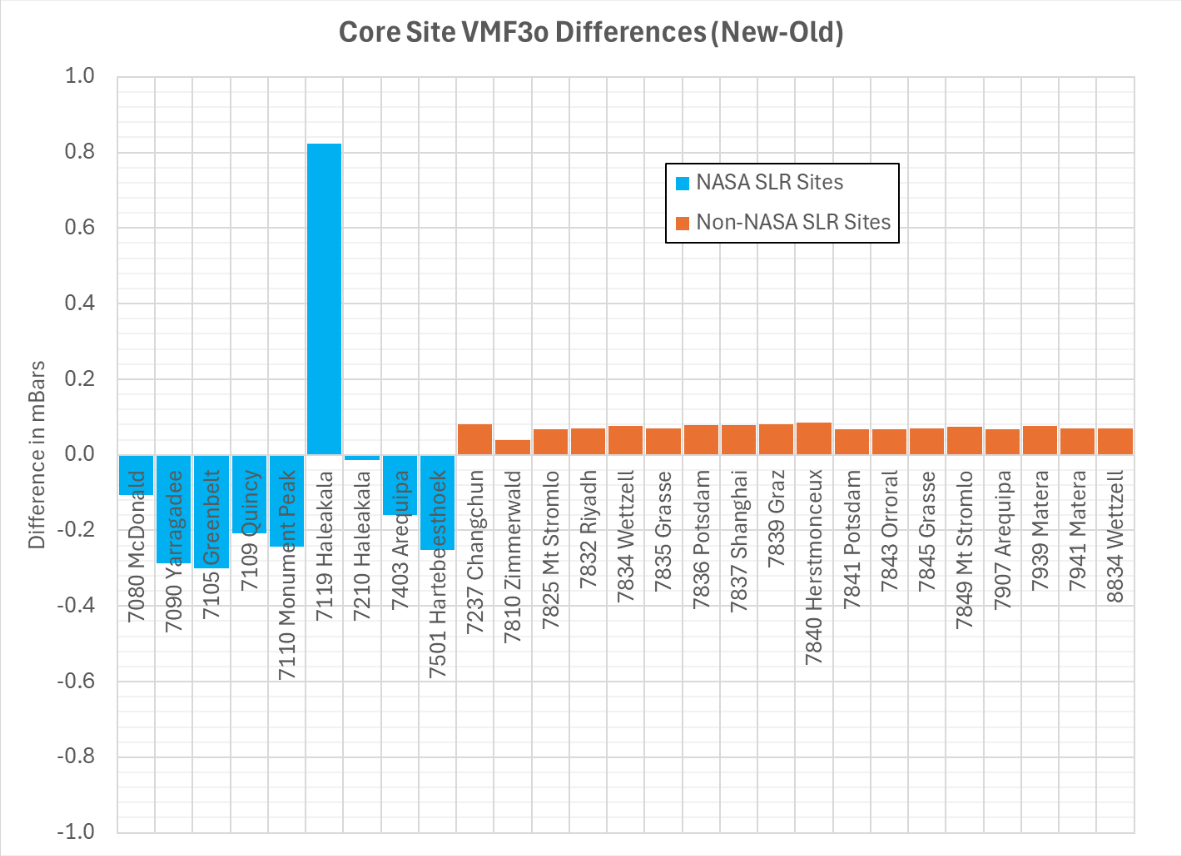

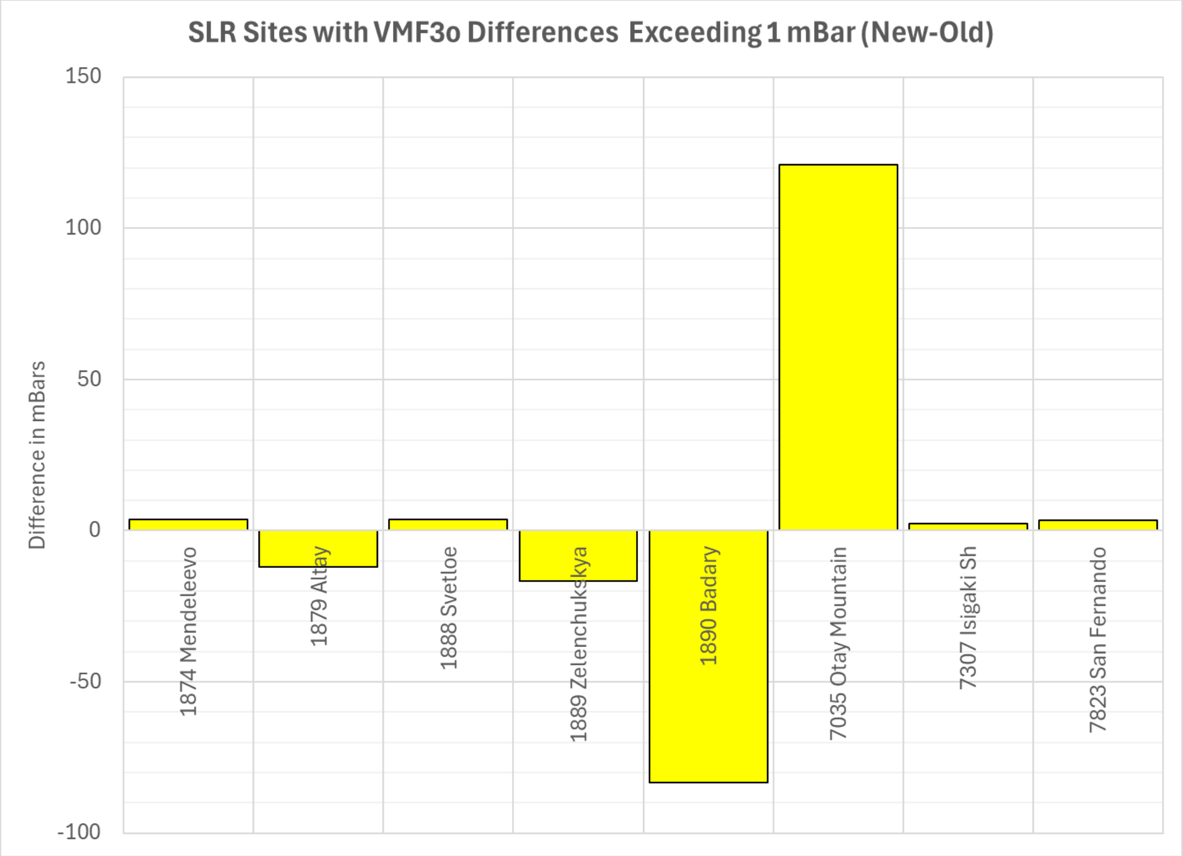

- ❑ **The old VMF3o data was based on the approximate station heights from the ILRS station eccentricity file**
- ❑ **The new VMF3o data is based on ITRF2020 heights. ITRF monument heights were adjusted based on the Up eccentricities (i.e. the system refence point for NASA SLR systems and other legacy transportable systems)**
- ❑ **The VMF3o differences between the old and new data are systematic. For Core ILRS sites the differences are sub 1 mBar. The original 7119 station height used was off by ~10m**

The Technique of Comparing VMF3o Pressures to SLR Pressures

- The VMF3o data is every 6 hours (00:00, 06:00, 12:00, 18:00 GMT)
- The NASA SLR Data Operations CRD NP Data Accountability DataBase (DB) contains the meteorological data from the last CRD 20 meteorological record and it is timestamped based on the CRD H4 header record start time
- We binned the SLR barometric pressures into six-hour bins (21:00 to 03:00; 03:00 to 09:00, 09:00 to 15:00, 15:00 to 21:00 GMT) and computed the average pressure within the bin and timestamped the data to the center of the bin (i.e. 0:00, 6:00, 12:00 and 18:00)
- Using the last CRD 20 CRD meteorological record may slightly alias our six-hour averages because HEO passes can last several hours
  - Starting in April 2025, we began to store every CRD 20 meteorological record received in a separate DB

What is the absolute accuracy of VMF3o_EI and VMF3o_OP Data?

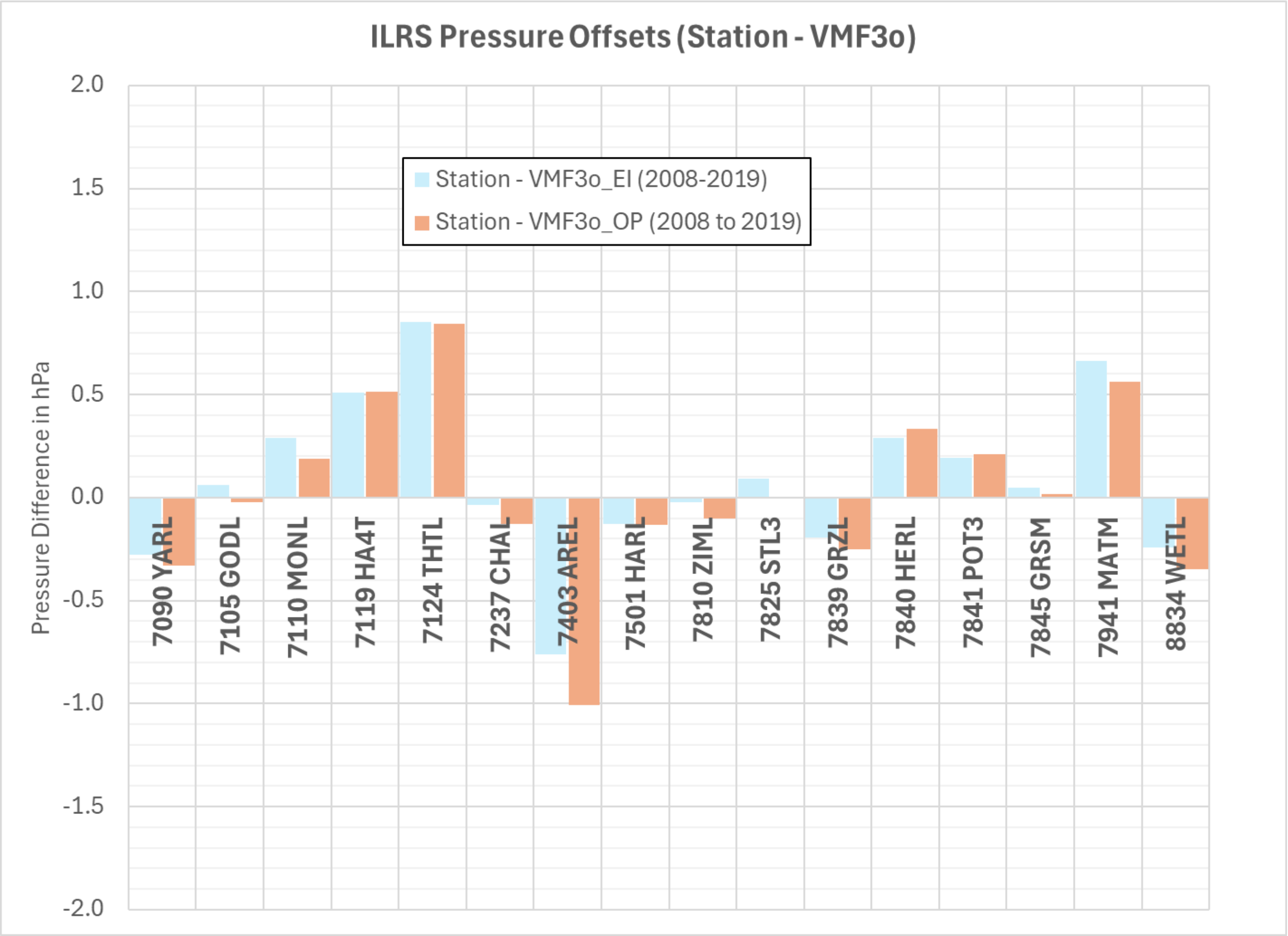

- Plotted here are the mean barometric pressure differences between the active sixteen ILRS Core stations and the two VMF3o categories, VMF3o_EI and VMF3o_OP for the 12 years (2008-2019) the data overlapped
- The aggregate pressure differences between the two VMF3o categories are within a few tenths of a hPa
- For twelve of the 16 sites, the barometric differences are less than 0.4 hPa. Stations 7119 and 7124 are on small islands in the Pacific Ocean. Is VMF3o data less accurate for sites near large bodies of water?
- Based on the first VMF3o paper (https://link.springer.com/article/10.1007/s00190-020-01385-5), there are semidiurnal variations with an amplitude of less than 3 hPa for stations 7090 YARL and 7839 GRZL

Average Six-Hour Differences (Station minus VMF3o_OP) for the ILRS Network (2024 and 2025)

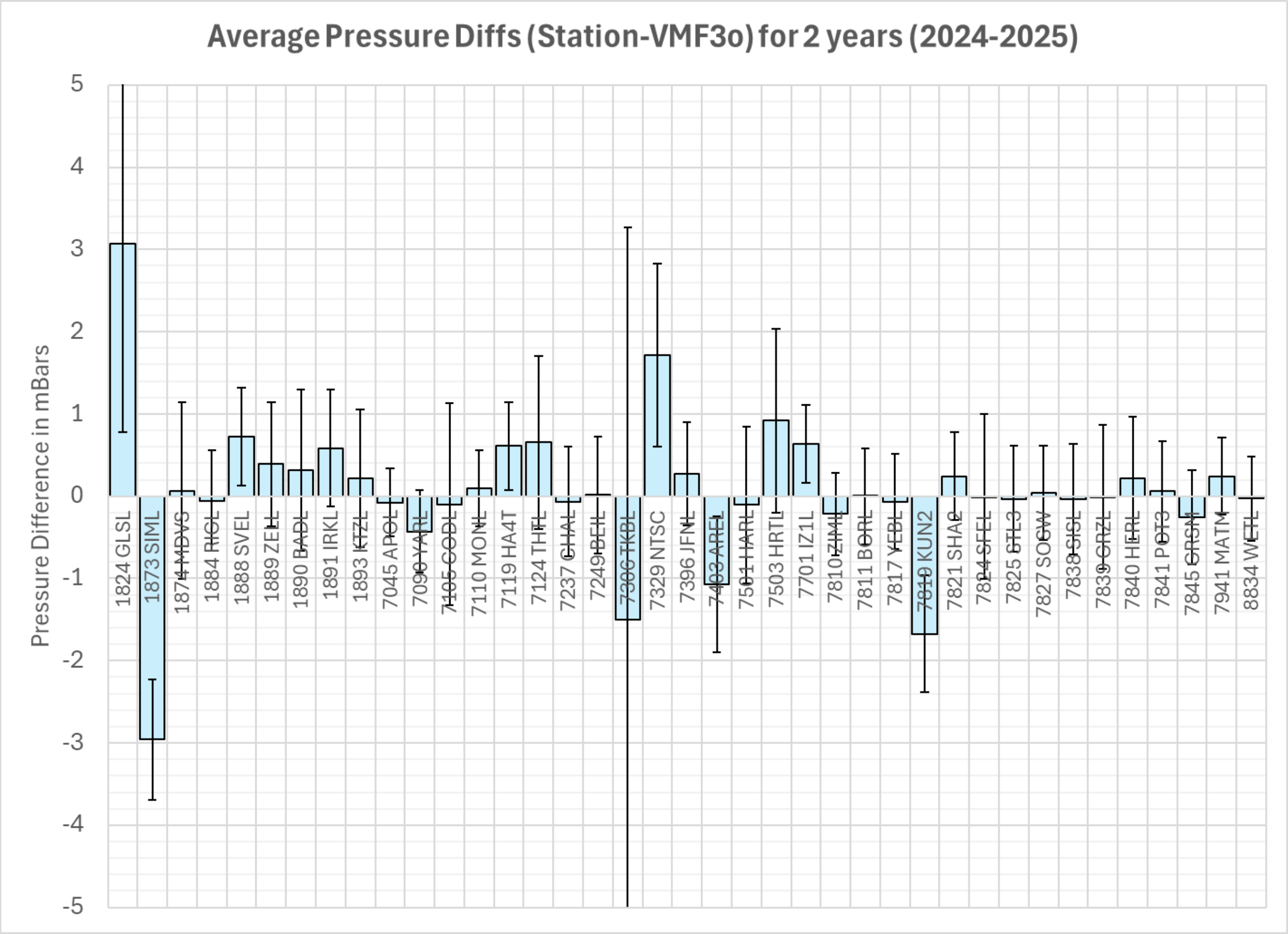

- **Six out of 39 sites have pressure differences exceeding 1 mBar on average**
  - Our two newest sites, Xian (7329) and Tsukuba (7306). Tsukuba (7306) differences have a high standard deviation
  - Golosiiv (1824) and Simeiz (1873). Golosiiv (1824) differences have a high standard deviation
  - Arequipa (7403) and Kunming (7819)
- **According to the sensor specifications for Golosiiv (1824) and Kunming (7819), the barometric accuracy is only +/- 1 mBar**
- **There appears to be an issue with the accuracy of the VMF3o data for Tsukuba (7306) and possibly Xian (7329)**

7306 TKBL and 7329 NTSC Pressures Differences (Station minus VMF3o_OP)

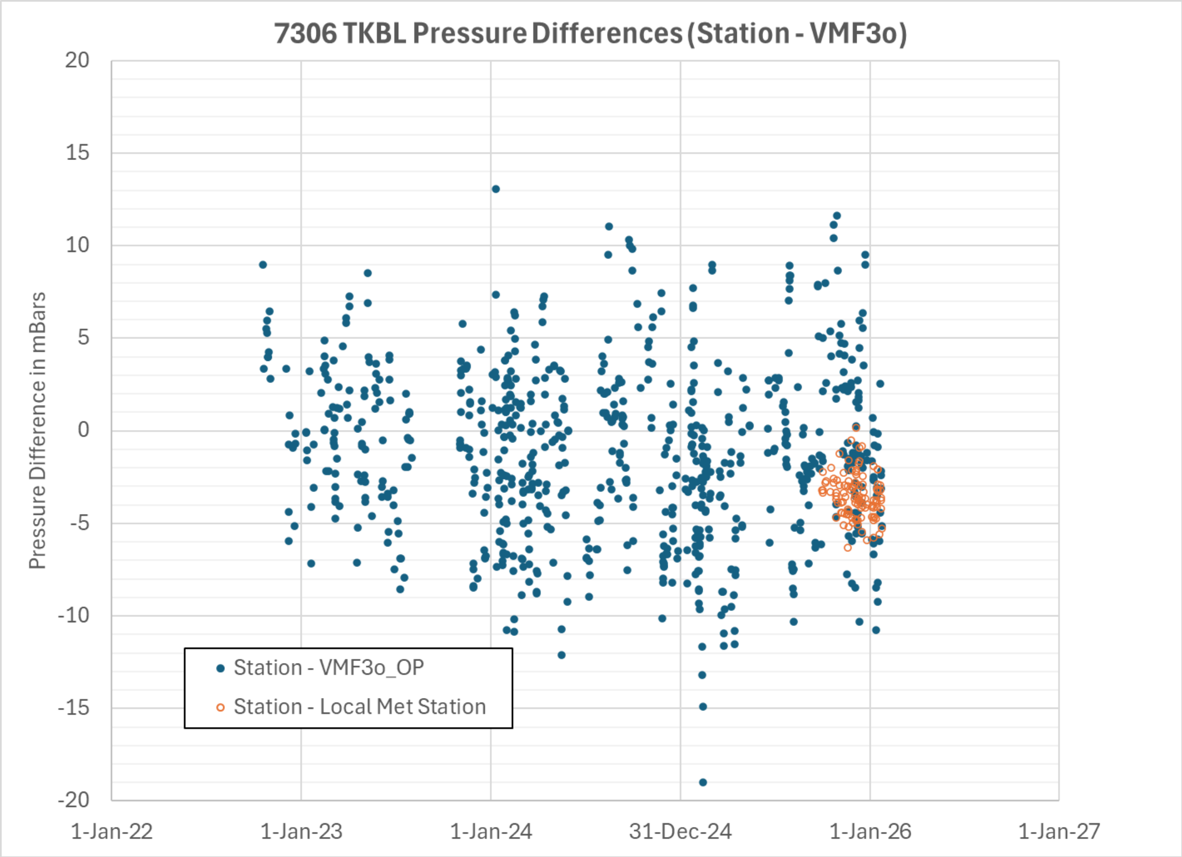

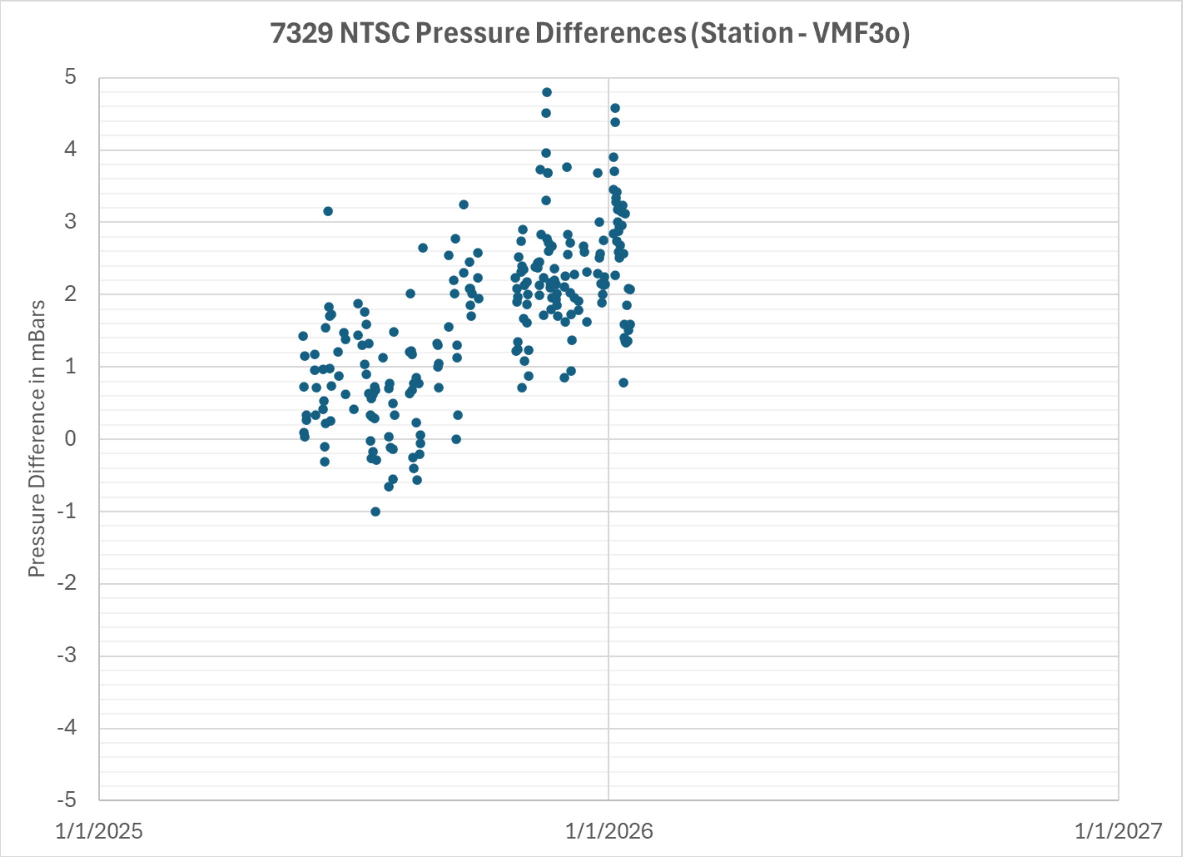

- ❑ **Tsukuba (7306) pressure differences (Station – VMF3o) have a large scatter, but data from a local Tsukuba weather bureau has reduced scatter suggesting an issue with the VMF3o data for that site**
- ❑ **Xian (7329) pressure differences (Station – VMF3o) appear to have a discontinuity. Needs further investigation**

Six-Hour Barometric Differences (Station – VMF3o)
Six Examples from Core Sites

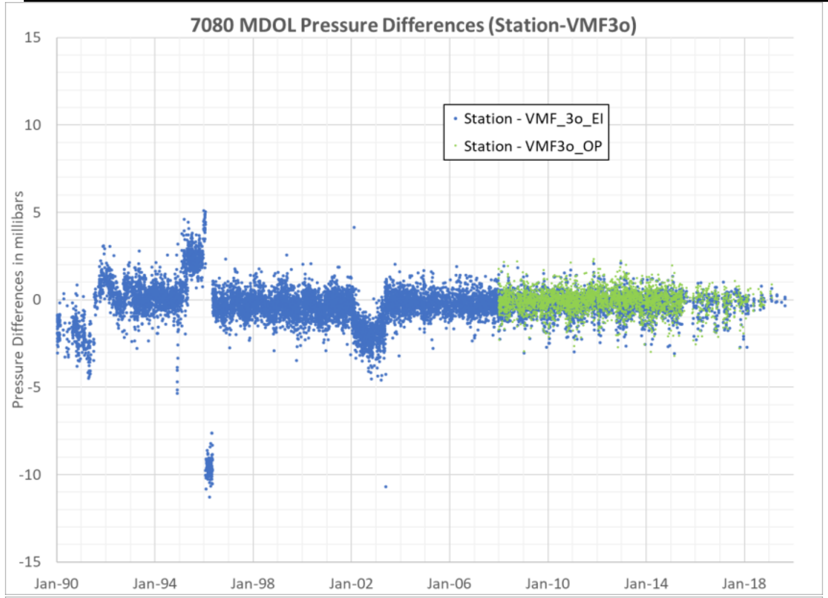

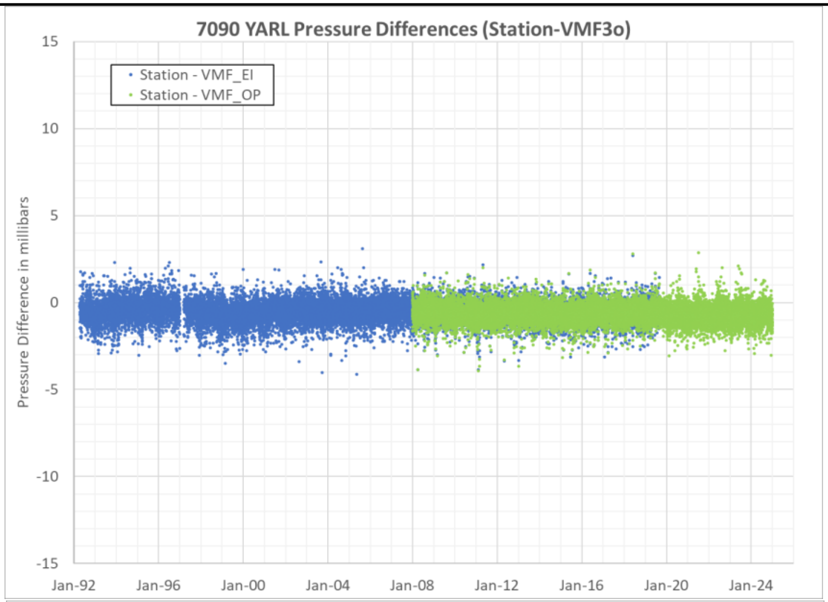

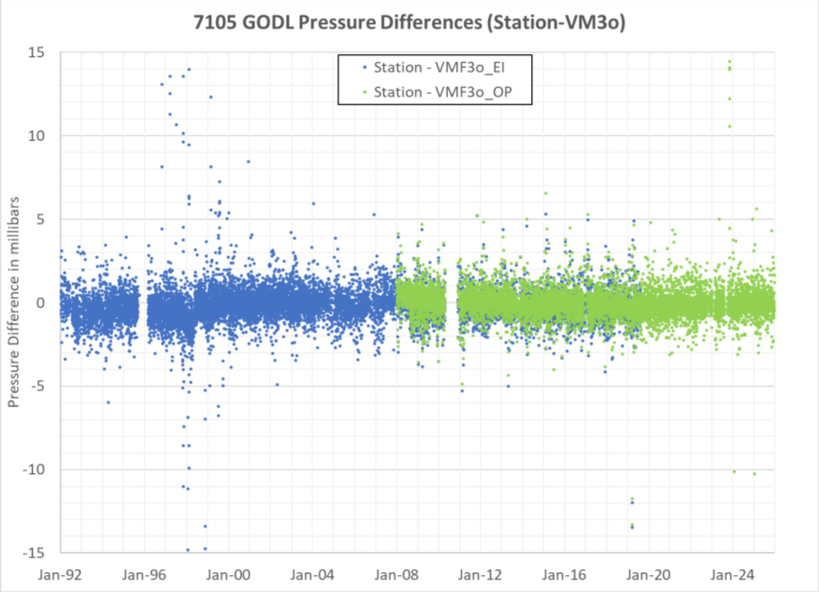

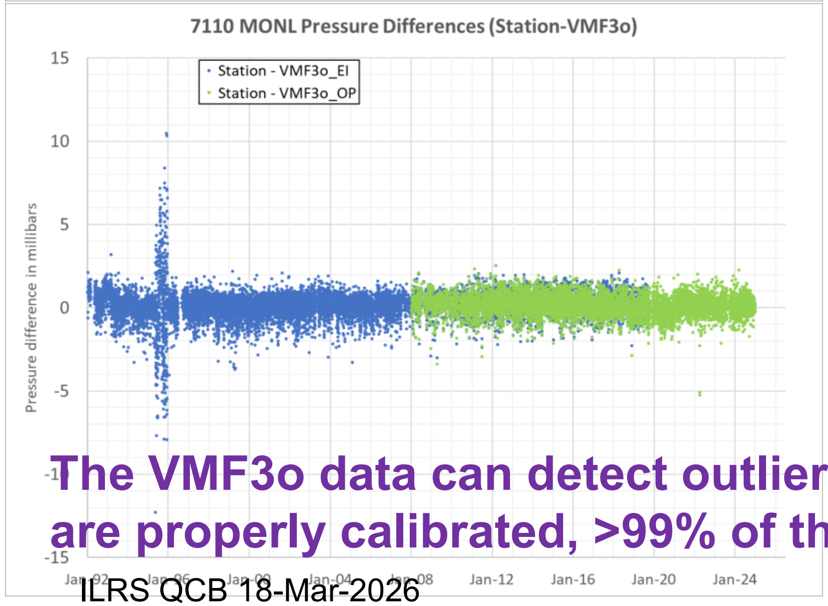

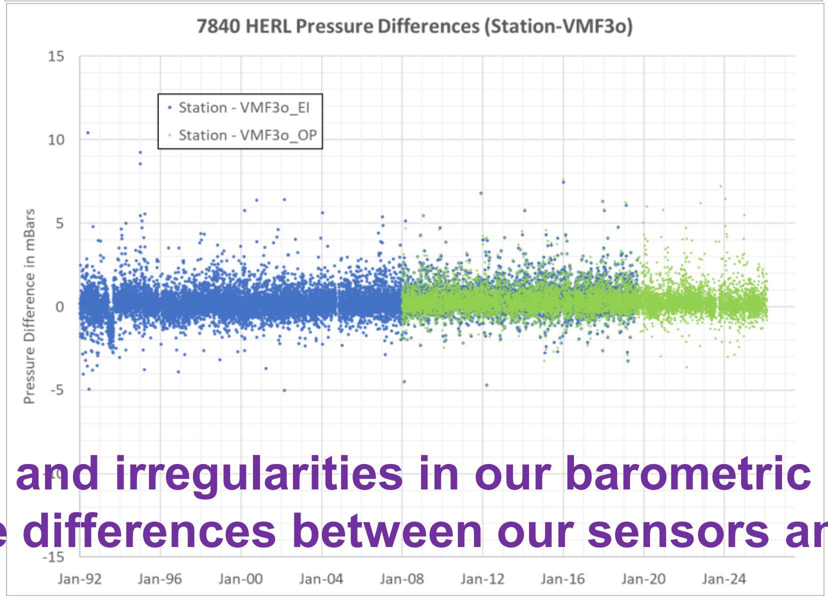

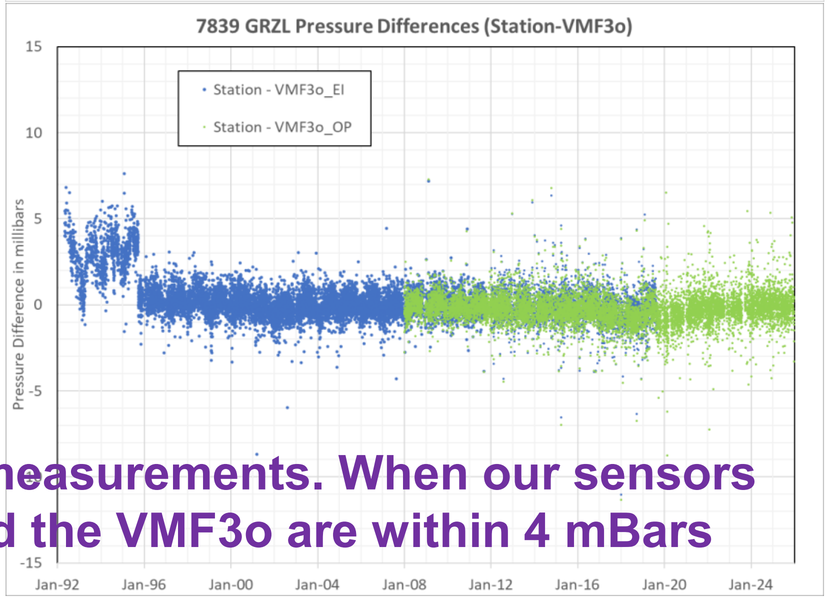

The VMF3o data can detect outliers and irregularities in our barometric measurements. When our sensors are properly calibrated, >99% of the differences between our sensors and the VMF3o are within 4 mBars

7080 MDOL Seasonal Differences between the Barometer and VMF3o

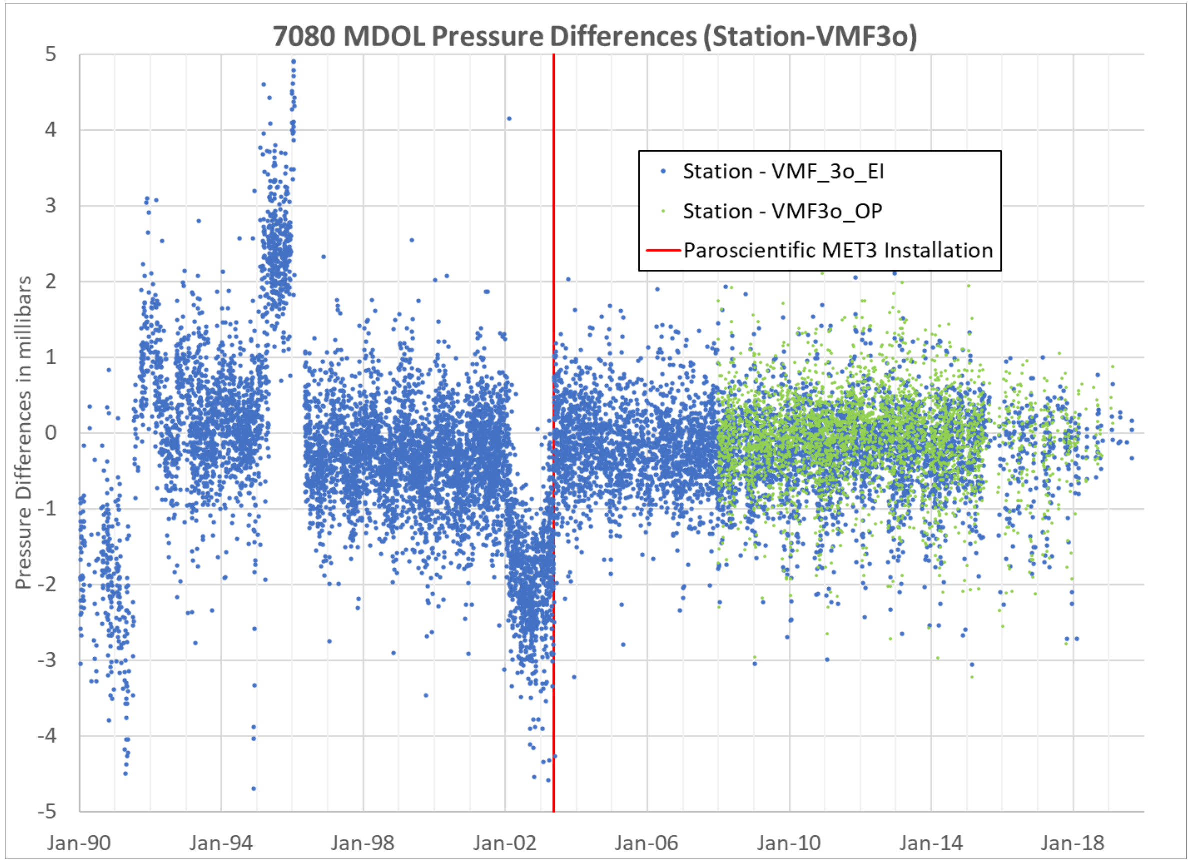

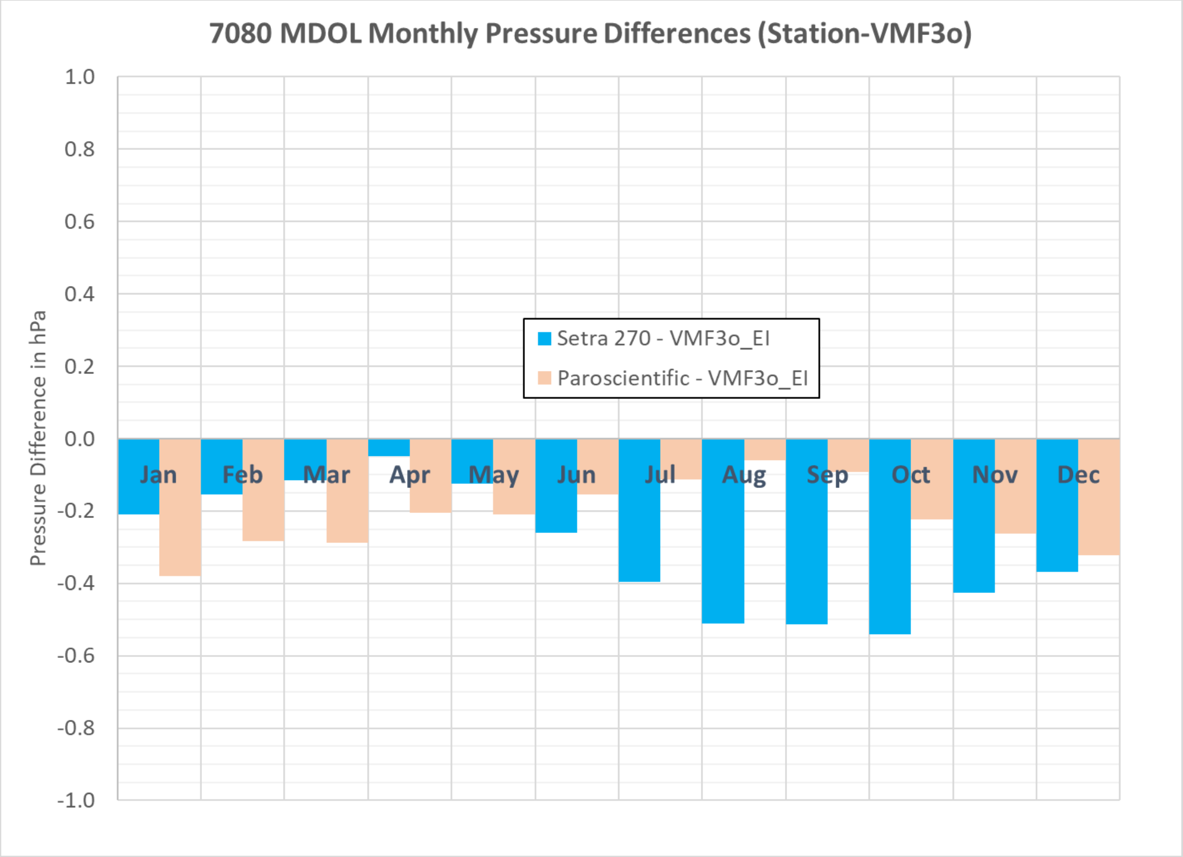

Seasonal Peak-to-Peak Variations	
Setra 270 - VMF3o_EI	MET3 - VMF3o_EI
0.49	0.32

- **On 17-May-2003, the Setra 270 Sensor was replaced with the Paroscientific MET3 which reduced the seasonal variations in the pressure differences**

7090 YARL Seasonal Differences between the Barometer and VMF3o

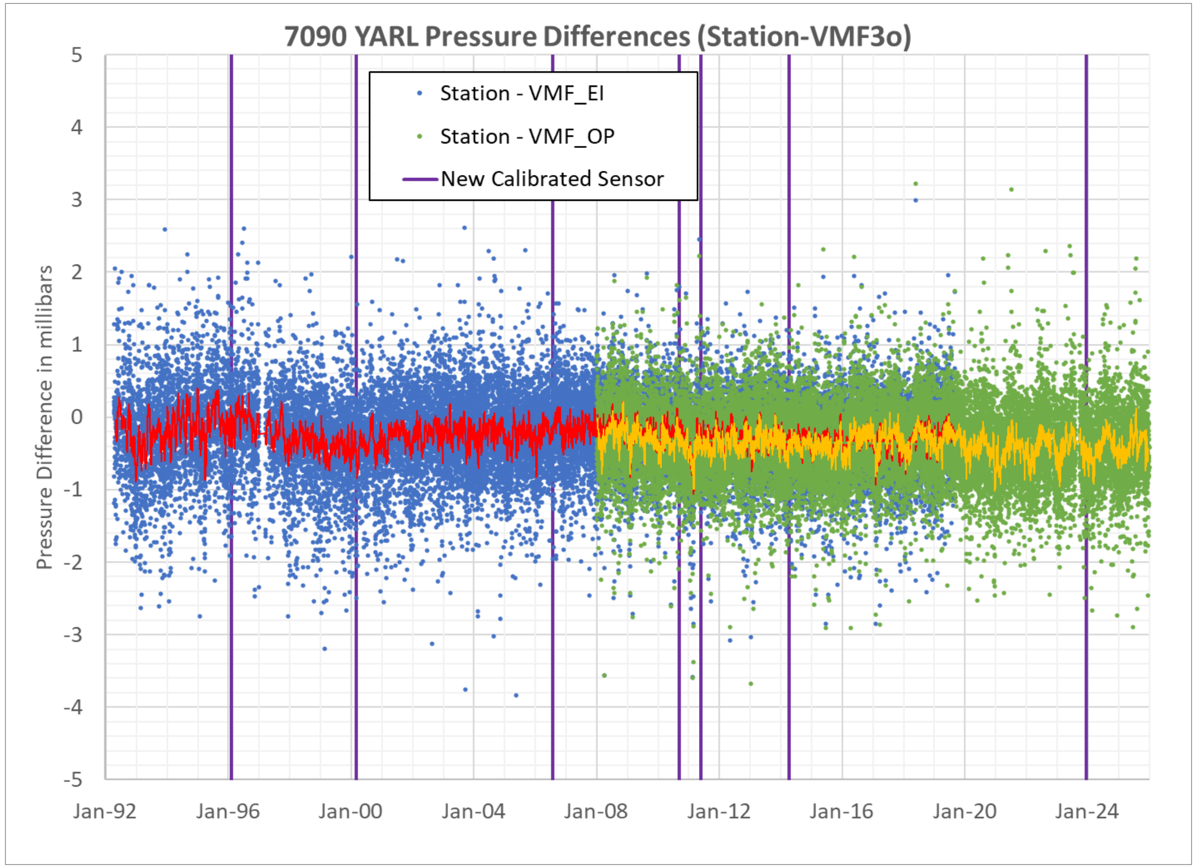

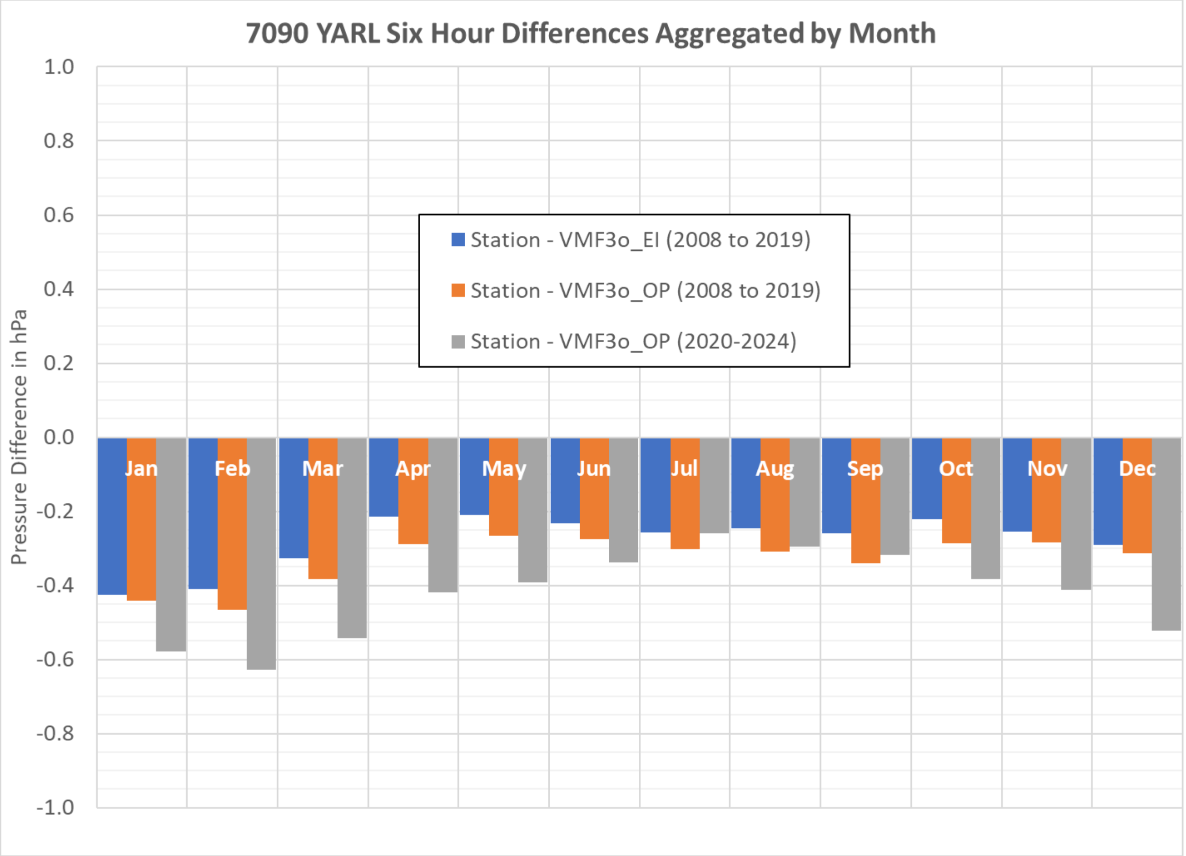

Seasonal Peak-to-Peak Variations		
Station - VMF3o_EI (2008-2019)	Station - VMF3o_OP (2008-2019)	Station - VMF3o_OP (2020-2025)
0.21	0.20	0.37

- **The seasonal variations in the station minus VMF3o_OP differences have increased perhaps starting in 2017**

New AutoQC Using VMF3o Data

- **In January 2026, the NASA SLR DOC implemented a new data integrity check to automatically flag, for further investigation, any six-hour period where the difference between the average six-hour pressures from the station and the VMF3o exceeds 4 mBars**
  - Twenty-five out of 1957 six-hour differences (station minus VMF3o) for 2026 (Jan and Feb) were flagged (1.3%)
    - One from Simeiz (1873): positive alarm, the mean difference between the Simeiz pressures and the VMF is -3 mBars
    - Twenty from Tsukuba (7306): false alarms, VMF3o data is suspect
    - Two From Xian (7329): inconclusive
    - Two from Simosato (7838): positive alarm, caused by frozen pressure for 3 hours on 8-Feb-2026 from 20:51 to 23:50
- **In February 2026, I was asked to peer review a paper titled "**Diagnosis strategy of abnormal on-site barometric pressure for SLR tropospheric delay correction**" written by our Chinese colleagues. In the paper, they automatically compare SLR pressures to Numerical Weather Model (NWM) derived pressures and auto correct SLR pressure measurements if the pressure difference exceeds 4 mBars**
- **How can aggregating the station minus VMF3o six-hour differences assist in barometric quality control. What other algorithms can be developed to identify short and long-term trends in the difference?**

Yearly Aggregation of the Six-Hour Differences

Tropospheric Biases in SLR Core Sites

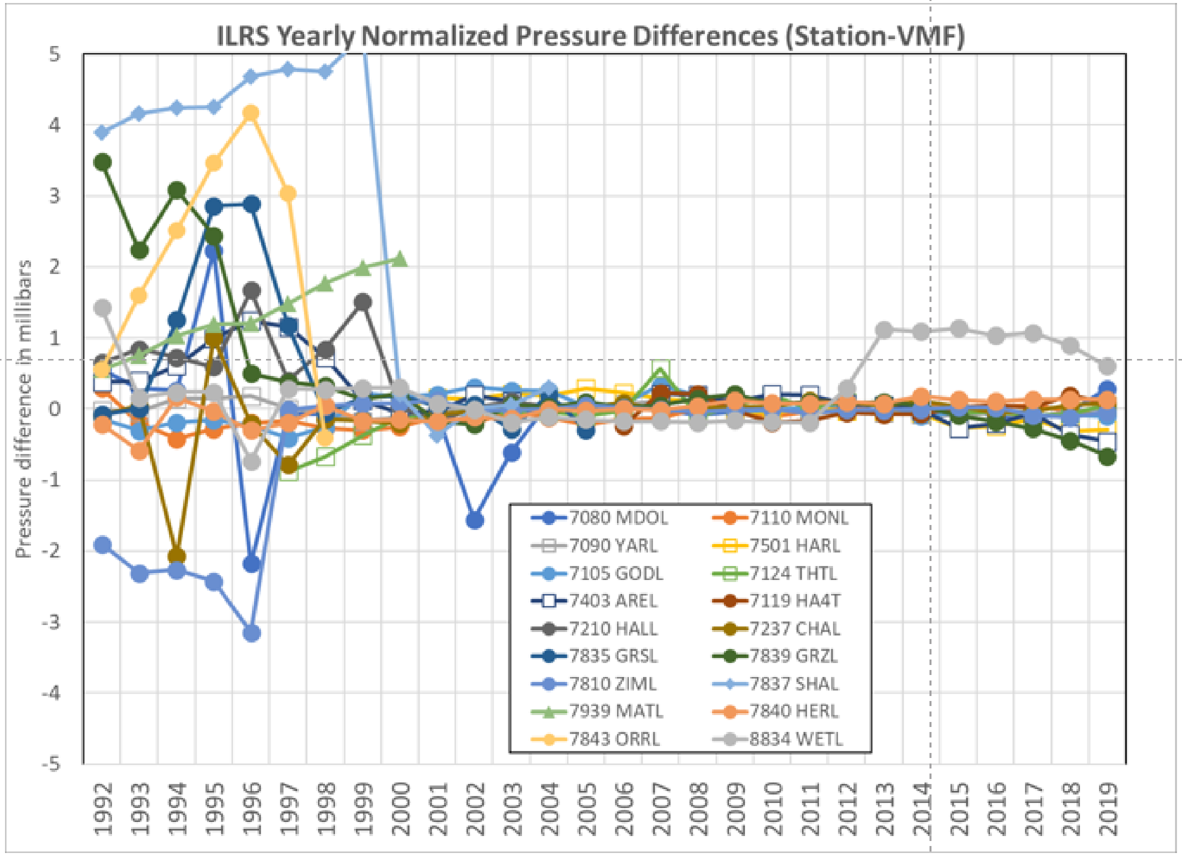

- ❑ A yearly time series of barometric errors in our core sites from 1992 to August 2019 based on comparing station's barometric data to the Vienna Mapping Function for optical frequencies (VMF3o)
- ❑ VMF3o is based on Numerical Weather Models (NWMs) provided by the European Centre for Medium-Range Weather Forecasts (Boisits et al., 2020) DOI:10.1007/s00190-020-01385-5

ILRS QCB 18-Jan-2023

14

- ❑ This slide was presented to the ILRS QCB in Jan-2023. This analysis was based on the original VMF3o_EI data
- ❑ As more accurate barometric sensors were deployed, the accuracy of the barometric data improved
- ❑ If you look closely, you will notice the discontinuity in the Wettzell 8834 data starting in 2012, when the height difference between the sensor and the SRP was not modelled. Also notice the drift in the Gras 7839 barometric pressure starting in 2015. Both stations reprocessed their data to remove these errors

Monthly Pressure Differences in mBars (Station minus VMF3o_OP)

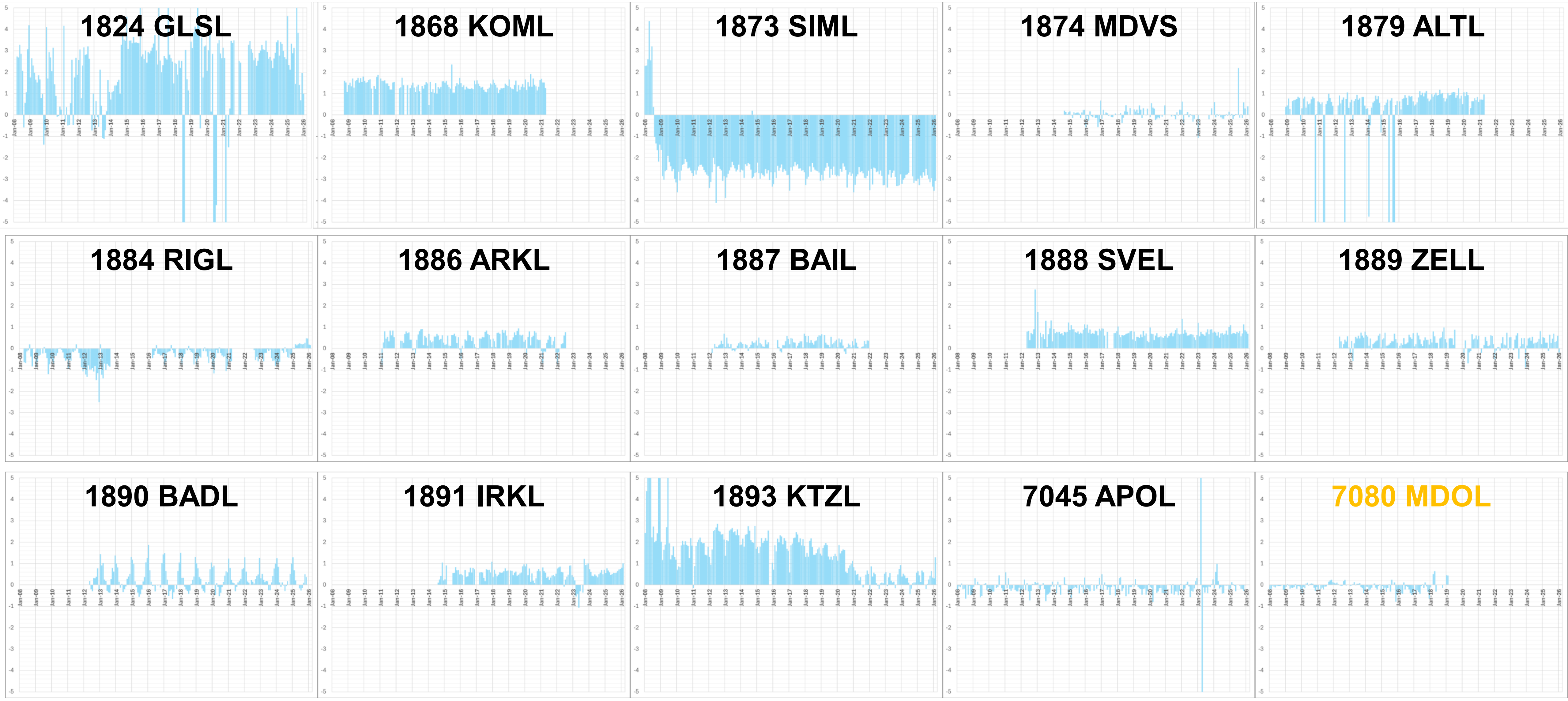

Monthly Pressure Differences in mBars (Station minus VMF3o_OP)

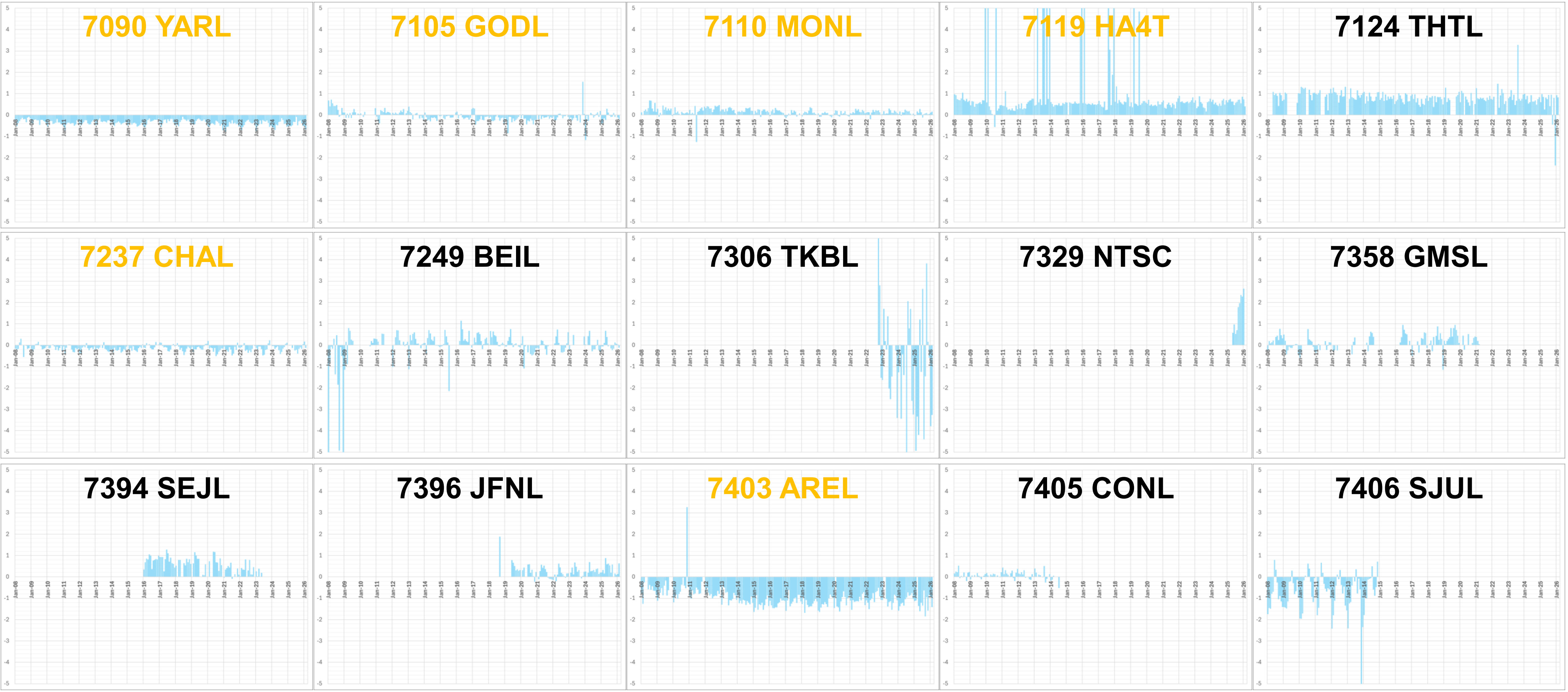

Monthly Pressure Differences in mBars (Station minus VMF3o_OP)

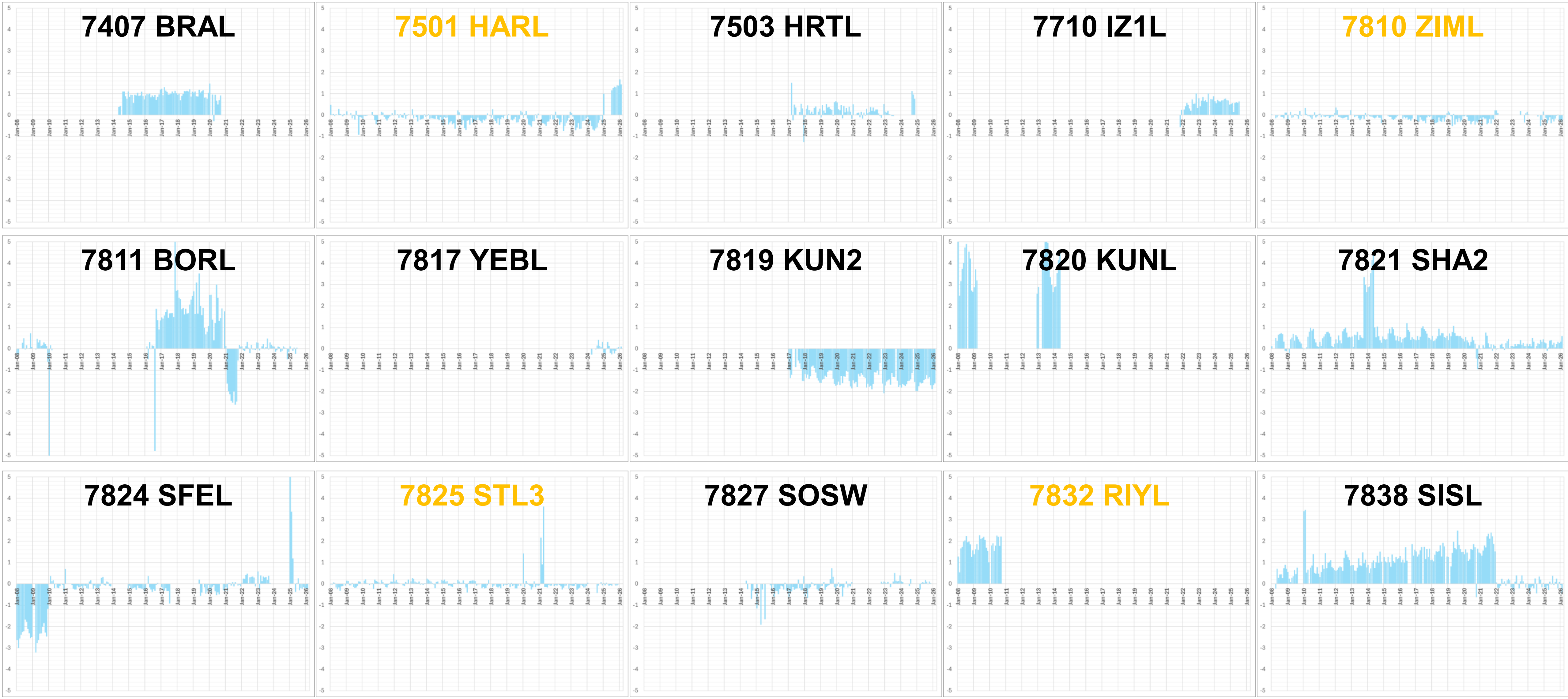

Monthly Pressure Differences in mBars (Station minus VMF3o_OP)

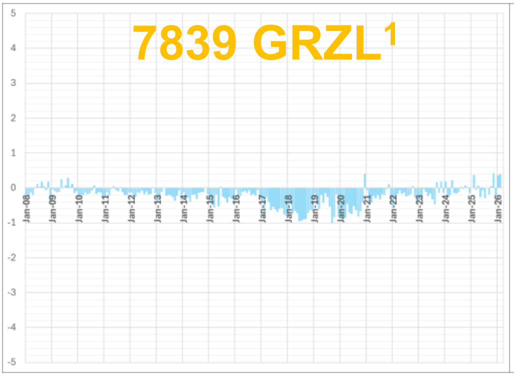

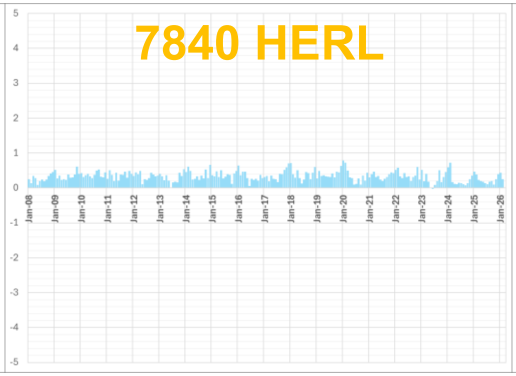

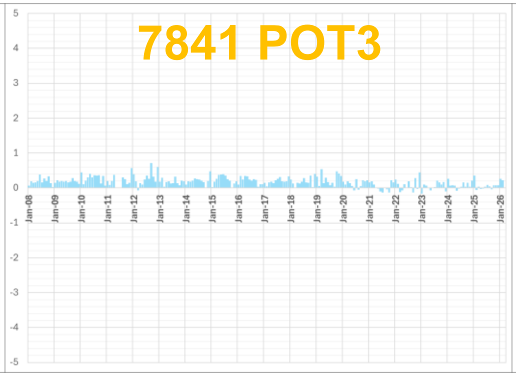

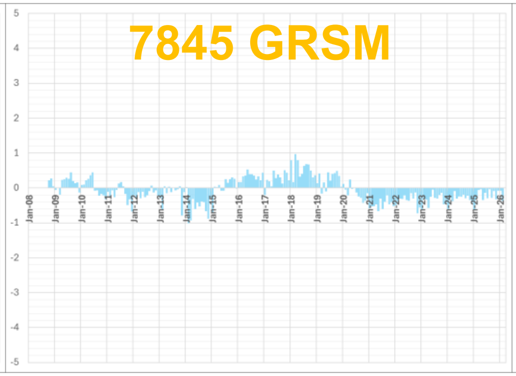

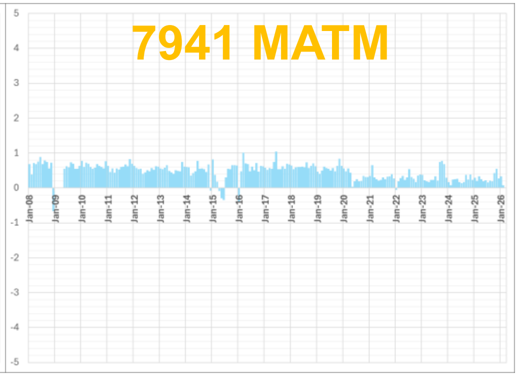

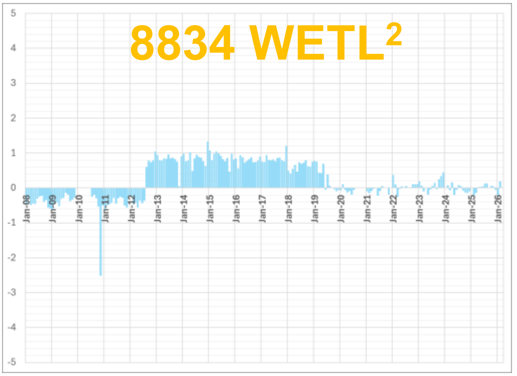

- *Footnote 1: 7839 GRZL results were based on a mixture of the original pressures and the corrected pressures*
- *Footnote 2: 8834 WETL results were based on the original pressures*

Other Station minus VMF3o Pressure Difference Statistics

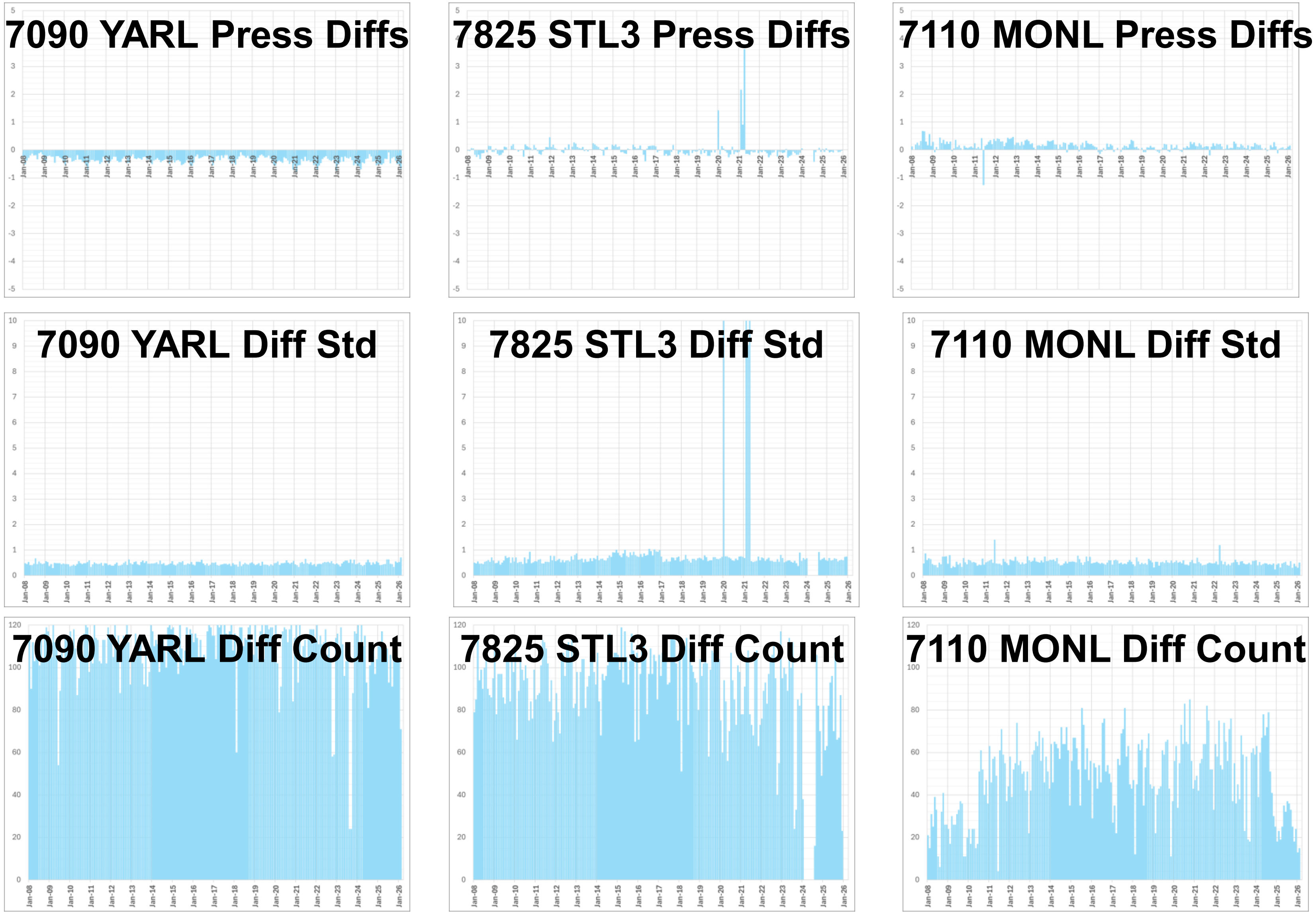

- The station minus VMF3o pressure differences alone don’t tell the whole story (1st row of charts)
- Adding in the standard deviation of the differences (2nd row of charts) reveals why there may be potential outliers in the differences in the 1st row. Large standard deviations may indicate frozen pressures and/or inexplicable jumps
- Adding in the count of differences (3rd row of charts) reveals the number of shifts that the station operates

Van’s Old Barometric Analysis vs the VMF3o Analysis

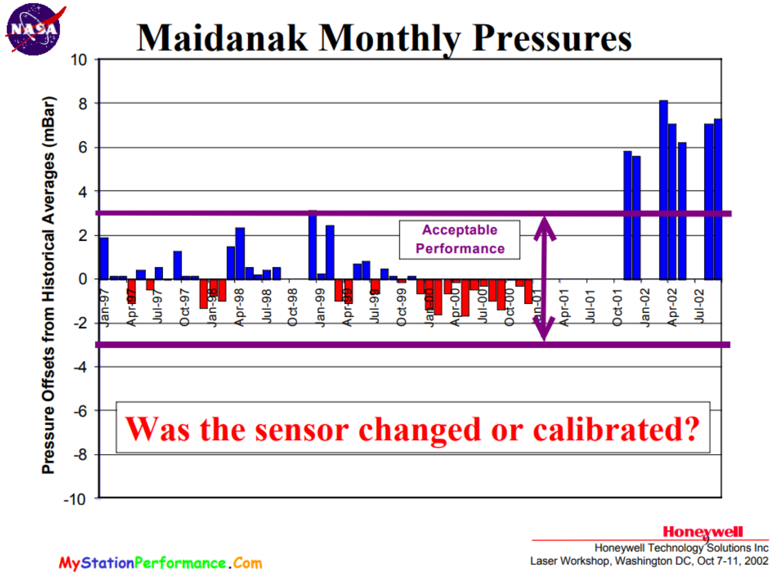

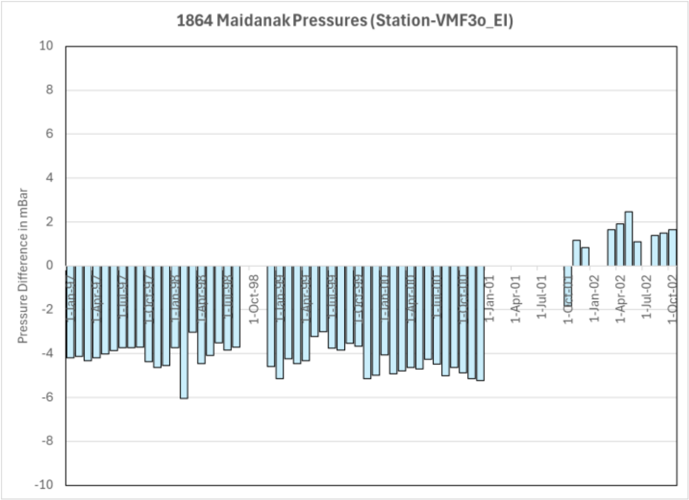

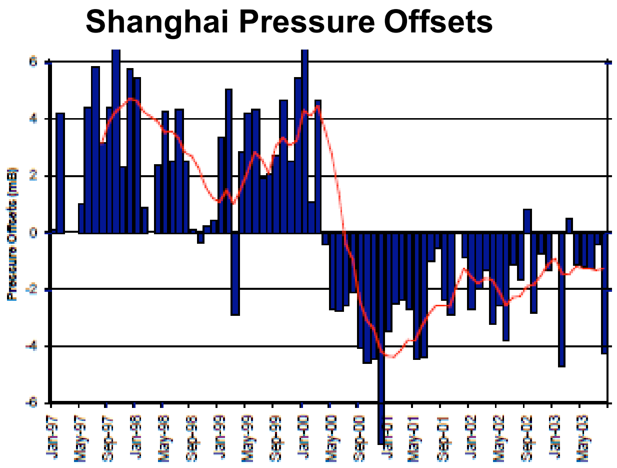

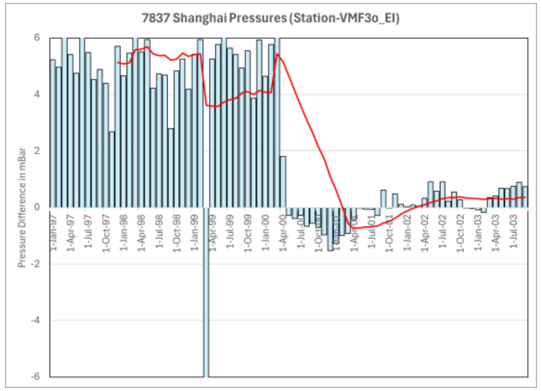

- Charts on the left were based on Van’s Pressure Monitoring Analysis from the early 2000’s
- Charts on the right were based on the VMF3o_El data
- Both analyses show the same trends in the barometric pressure discontinuities
- The most recent legacy Shanghai (7827) barometric sensor appears to be drifting positive

Meteorological Data Processing and Handling from Cradle to Grave?

Meteorological Data in the CSTG or MERIT II Format

- In both SLR legacy data formats, there were meteorological data in every Normal Point (NP) an FullRate (FR) record. No interpolation of meteorological data required
- In May 2012, the CRD format became the new ILRS data format. Based on the CRD format, interpolation of meteorological data may be required to the epoch of the NP or FR observation

CRD 20 Meteorological Record Format

3.4. Meteorological Record

This data record contains a minimal set of meteorological data. At least one record must appear in the data file.

3.4.1. Format:

1. A2(1-2) Record Type (= "20")
2. F18.12 Seconds of day (typically to 1 milllisec precision).
3. F7.2 Surface pressure (millibar)
4. F6.2 Surface temperature in degrees Kelvin
5. F4.0 Relative humidity at the surface in %
6. I1 Origin of values

    0=measured values (written whenever a value changes “significantly”)

    1=interpolated values applicable at the time (seconds of day) given in this record

3.4.2. Notes

Meteorological records should only be written when one of the fields changes “significantly”. As a minimum, a new record should be written whenever pressure changes by 0.1mB, the temperature changes by 0.1 K, or when the humidity changes by 5%. The time (seconds of day) of an interpolated record should match the time in the following normal point record.

Since meteorological records may be submitted in blocks and not interspersed with the normal point or range records, it is recommended that the meteorological records be accumulated and interpolated to the times needed (e.g., times of normal points or full rate records).

NASA SLR CRD Meteorological Record

```
h1 CRD  2 2026  1 30  5
h2 YARL       7090  5 13 3       ILRS
h3 lageos1     7603901 1155     8820 0 1 1
h4  1 2026  1 30  4 44 24 2026  1 30  5  1 46  0 0 0 0 1 0 2 0
h5  1 26 012800 SGF 05291
c0 0  532.000 new la1 mcp ti1 swm met    cac
c1 0 la1 Nd:Yag     1064.00       5.00      100.00  150.0  6.00     1
c2 0 mcp MCP-PMT     532.000  15.0 3393.0  31.0 analog 400.0  1.00  80.0 30.00 none     na      na  0
c3 0 ti1 Truetime_XLDC Truetime_XLDC Cybi_ETM na     0.0
c5 0 swm  sattrk 6.10 HPLDP,GNP 9.11.3,2.8.5
c6 0 met  Paroscientific MET-4 106772 Paroscientific MET-4 106772 Paroscientific MET-4 106772
c7 0 cac B             150.42450   1.00   0.1651 na                  HPLDP 9.11.3
40 17188.700584229082 0 new     2457     2443 150.4245    96307.3     0.0   21.3 na      na      na     2 2 0 3 na
41 14530.200585443527 0 new      865      857 150.4245    96308.0 na         17.3 na      na      na    2 2 0 1 na
41 19887.450584722683 0 new     1592     1580 150.4245    96306.6 na         22.7 na      na      na     2 2 0 2 na
20 17097.401  979.40 313.80  16. 0
11 17097.400587900000     0.047713806818 new 2  120.0     60   45.0   0.003   0.752 na          10.00 0 na
20 17238.401  979.40 313.30  16. 0
11 17238.400584600000     0.046097010679 new 2  120.0      9   27.0   0.366  -1.102 na           1.50 0 na
20 17385.801  979.40 313.00  16. 0
11 17385.800587700000     0.044708380878 new 2  120.0     30   42.0   0.062  -0.855 na           5.00 0 na
20 17439.601  979.40 313.00  16. 0
11 17439.600587699999     0.044285216082 new 2  120.0     78   53.0  -0.190   0.136 na          13.00 0 na
20 17584.401  979.30 313.00  16. 0
11 17584.400584700001     0.043384708040 new 2  120.0     54   45.0  -0.445   0.467 na           9.00 0 na
20 17682.201  979.30 313.30  16. 0
11 17682.200585700000     0.042982335545 new 2  120.0     29   59.0  -0.139  -0.840 na           4.83 0 na
20 17987.701  979.00 313.80  16. 0
11 17987.700583800000     0.042842504489 new 2  120.0      7   27.0  -0.472  -0.734 na           1.17 0 na
20 18056.101  979.20 314.30  16. 0
11 18056.100584299998     0.043043418127 new 2  120.0     26   47.0   0.135  -0.629 na           4.33 0 na
50 new    48.2  -0.178   0.174 na      0
```

- **In the NASA SLR onsite Normal Point (NP) generation software, a 20 meteorological record is created for each NP (see 20 meteorological records highlighted in green).**
- **The seconds of the day of 20 meteorological record matches the seconds of day of 11 range record but is rounded to the millisecond. (See 11 range records highlighted in gray)**
- **The meteorological measurement is based on the met data associated with the fullrate observation whose epoch is nearest to the mean epoch of the accepted fit residuals in the NP bin**
- **Barometric pressures did fluctuate by 0.4 mBar**

WPLTN CRD Meteorological Record

```
H1 CRD 2 2026 1 1 13
H2 CHAL 7237 19 01 4 ILRS
H3 lageos1 7603901 1155 08820 0 1 1
H4 1 2026 1 1 8 21 24 2026 1 1 8 43 13 0 0 0 0 1 0 2 0
H5 1 25 122900 HTS 36301
C0 0 532.000 std   CL2  CD1  CT1   na CSO1 CME1 CCA1
C1 0  CL2 Nd-YAG       1064.00    2000.00      2.50   50.0 10.31    1
C2 0  CD1 CSPAD 532.000 20.00 5.0 60.0 TTL 0.0  1.70 0.0 0.0 none na na na
C3 0  CT1 Meridian Meridian ET-A033 003309 0.0
C5 0 CSO1 SLR_TRACK V3 Pro2002 V1
C6 0 CME1 Paroscientific MET3 69628 Paroscientific MET3 69628 Paroscientific MET3 69628
C7 0 CCA1 NearTarget 3.699 1.0 0.0 2.0 Cal2000 V1
40 29880.000000000 0  std 4618 4248 3.699 183947.0 na 45.0 0.190 2.581 -2.0 4 0 0 1 92.0
41 29880.000000000 0  std 4618 4248 3.699 183947.0 na 45.0 0.190 2.581 -2.0 4 0 0 1 92.0
20 31396.000000000 999.90 255.90  58. 0
11 30100.887500870002 0.047220542835  std 2 120.0 338 25.3 0.012 -0.782 0.0 0.1 0 na
11 30183.749500869999 0.046356161305  std 2 120.0 1068 23.7 0.041 -0.669 -0.0 0.4 0 na
11 30294.731500869999 0.045368059203  std 2 120.0 1033 23.5 0.024 -0.604 -0.0 0.4 0 na
11 30419.745160840001 0.044505530146  std 2 120.0 974 22.8 0.045 -0.603 -0.0 0.4 0 na
11 30529.101660839999 0.043982848388  std 2 120.0 375 23.2 -0.128 -0.544 -0.0 0.2 0 na
11 31171.276500870001 0.045512350017  std 2 120.0 435 21.6 0.122 -0.822 -0.0 0.2 0 na
11 31264.500000860000 0.046353007356  std 2 120.0 599 22.0 0.155 -0.754 0.0 0.2 0 na
11 31357.481500860002 0.047325533497  std 2 120.0 437 25.1 0.087 -0.565 0.0 0.2 0 na
50  std 31.0 0.039 -0.635 -1.8 0
```

- **In this Changchun LAGEOS-1 CRD, there is only one 20 meteorological record and the 20 record seconds of day is greater than the epoch of the last 11 NP range record by 39 seconds**
- **Other non-LAGEOS Changchun CRDs only have one 20 meteorological record**
- **Since there is only one range record the meteorological data can NOT be interpolated. Should this be flagged as a data integrity issue? How do the different ACs handle this?**

EUROLAS CRD Meteorological Record

```
H1 CRD 2 2026 1 4 0
H2 HERL 7840 35 1 4 ILRS
H3 lageos1 7603901 1155 08820 0 1 1
H4 1 2026 1 3 23 28 19 2026 1 4 0 4 27 0 0 0 0 1 0 2 0
C0 0 532.080 PS kHzPS SPD5 HMas  HxF HxMet Hxtr
C1 0 kHzPS Nd-Yag 1064.16 1000.00 1.50 25.0 20.00 1
C2 0 SPD5 SPAD5 532.080 20.00 0.0 200.0 +0.7V 0.0 0.15 90.0 0.0 Single_fot 0.0 0.0 0
C3 0 HMas iMaser_3000 iMaser_3000 HxET_=_3x_dassault 55 5.743
C5 0 HxF kgate,dplay 0.1,0.1 solve,gauss 0.1,0.1
C6 0 HxMet Druck DPI141 (700/99-06)&(449/97-1) Rotronics MP103A-T7-W4W 46174001 Rotronics MP103A-T7-W4W 46174001
20 84179.520000 1010.47 269.90 84.6 0
20 84542.400000 1010.43 269.90 84.6 0
20 84896.640000 1010.39 269.90 84.6 0
20 85259.520000 1010.35 269.80 84.6 0
20 85622.400000 1010.45 269.80 84.8 0
20 85976.640000 1010.54 269.80 84.8 0
20 86158.080000 1010.53 269.70 84.8 0
20 120.960000 1010.53 269.70 84.9 0
20 483.840000 1010.55 269.70 85.3 0
41 83972.160000 0 PS 2492 2492 122.977 104777.8 0.0 22.0 0.070 -0.480 4.0 2 0 0 1 na
41 1010.880000 0 PS 3412 3412 122.977 104780.5 0.0 22.7 0.170 -0.260 -3.0 2 0 0 2 na
40 85583.520000 0 PS 5904 5904 122.977 104779.1 -2.7 22.3 0.120 -0.370 0.5 2 2 0 3 na
50 PS 59.4 0.424 -0.343 -8.0 0
11 84550.291234400000 0.049017373350 PS 2 120.0 600 57.0 na na na 0.5 0 na
11 84628.381745600000 0.047734296147 PS 2 120.0 739 60.0 na na na 0.6 0 na
11 84936.130165700000 0.043370386898 PS 2 120.0 1261 60.0 na na na 1.1 0 na
11 84968.725255200000 0.042984572504 PS 2 120.0 877 59.0 na na na 0.7 0 na
11 85139.588765700000 0.041246536675 PS 2 120.0 1043 59.0 na na na 0.9 0 na
11 85248.444439700000 0.040410729909 PS 2 120.0 646 56.0 na na na 0.5 0 na
11 85417.654019700000 0.039573077857 PS 2 120.0 734 54.0 na na na 0.6 0 na
11 85537.847019700000 0.039338071860 PS 2 120.0 2130 56.0 na na na 1.8 0 na
11 85569.481019700000 0.039327069914 PS 2 120.0 1179 55.0 na na na 1.0 0 na
11 85753.079847700000 0.039680695974 PS 2 120.0 1045 58.0 na na na 0.9 0 na
11 85879.612347700000 0.040328206118 PS 2 120.0 3710 58.0 na na na 3.1 0 na
11 85930.120347700000 0.040674269484 PS 2 120.0 879 55.0 na na na 0.7 0 na
11 86104.540275400000 0.042226240185 PS 2 120.0 1349 60.0 na na na 1.1 0 na
11 86225.948108700000 0.043604074144 PS 2 120.0 1061 62.0 na na na 0.9 0 na
11   229.339531700000 0.049560389354 PS 2 120.0 1278 66.0 na na na 1.1 0 na
11   253.027502000000 0.049962263723 PS 2 120.0 881 69.0 na na na 0.7 0 na
H8
```

- **In this Herstmonceux LAGEOS-1 CRD, there are multi 20 meteorological records and 11 NP range records, and the epochs of the 20 meteorological records are different from the 11 NP range record epochs**
- **The data analysts can interpolate and/or extrapolate the meteorological data to the epoch of the 11 NP range record**
- **Barometric pressures fluctuated by 0.16 mBars**
- **Note: This was a midnight crossing pass**

20 Meteorological Data Records Per LAGEOS-1 NPs (September 2025 to January 2026)

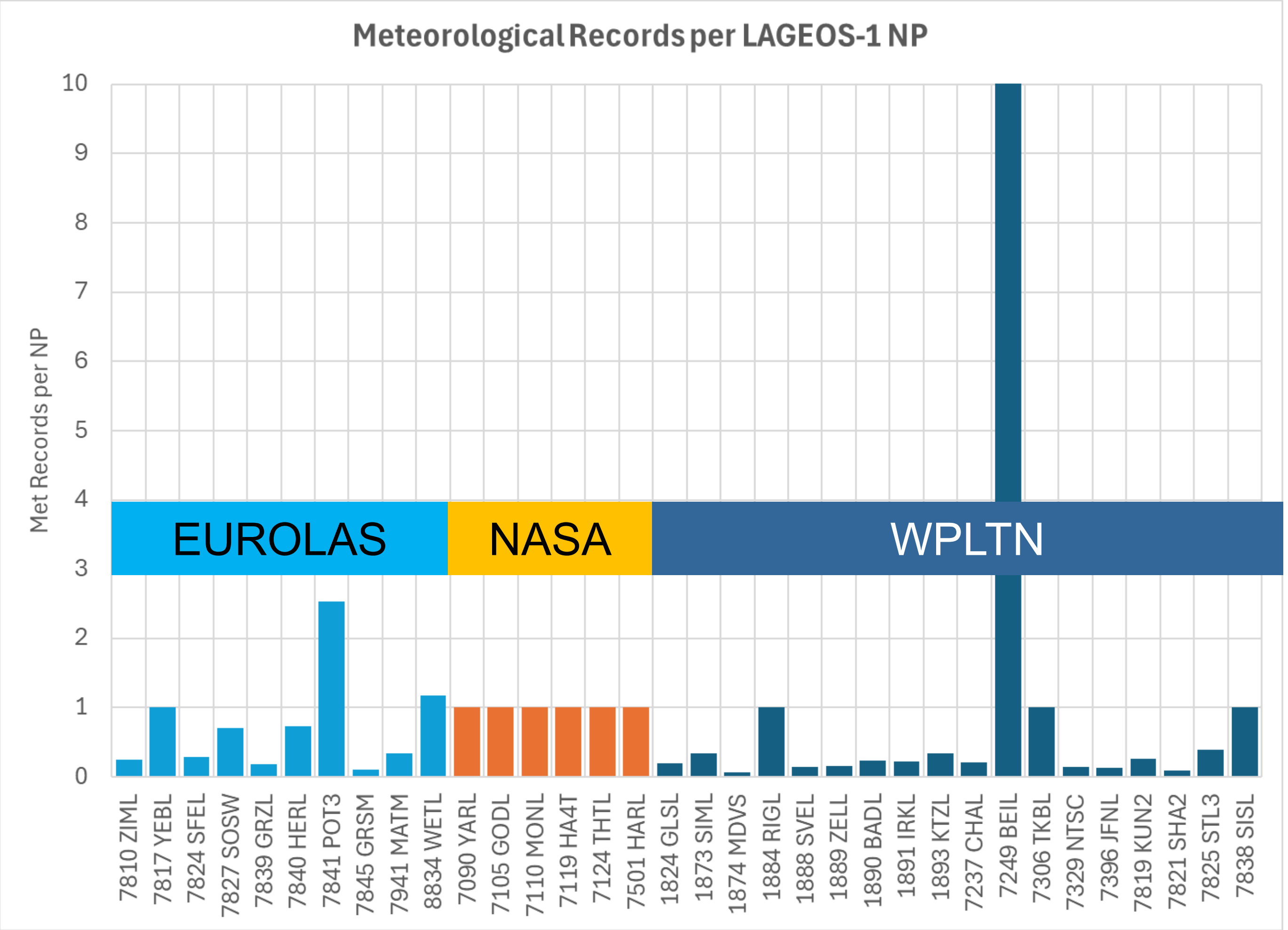

- ❑ **The legacy SLR formats (CSTG and MERIT II) included meteorological data in each NP record, so there was no need to interpolate/extrapolate**
- ❑ **The number of CRD 20 meteorological records per LAGEOS NP is diverse across the ILRS network (0.06 to 10)**
- ❑ **NASA SLR sites share the same data reduction software**
- ❑ **Having a meteorological record per each NP eliminates the possibility of an interpolation error by the data analysts**
  - ➢ Should the stations adopt this as a best data reduction process?

Issues with applying Barometric Pressure Corrections from the DHF

7080 Different Application of Tropospheric Biases by the ACs

- When a tropospheric bias is to be applied along with range bias estimation the application of the tropospheric bias is not consistent
- Below is an DHF example from McDonald (7080), where the tropospheric biases are in a period of RB estimation

*COI	Pad	S			Start Da	End Da	Bias Co	Bi	S'	Ra	UN	Com
	7080	51	501	A	93:001:00000	96:133:00000	E				mm	
	7080	52	501	A	93:001:00000	96:133:00000	E				mm	
	7080			A	95:065:00000	96:025:86400	P	-2.1			mB	BRE
	7080			A	96:026:00000	96:115:86400	P	-10.3			mB	BRE
	7080			A	96:116:00000	96:129:72000	P	-9.7			mB	BRE

Legend
Esitmate
Pressure Error

Legend	
51	LAGEOS-1
52	LAGEOS-2
	all Satellites

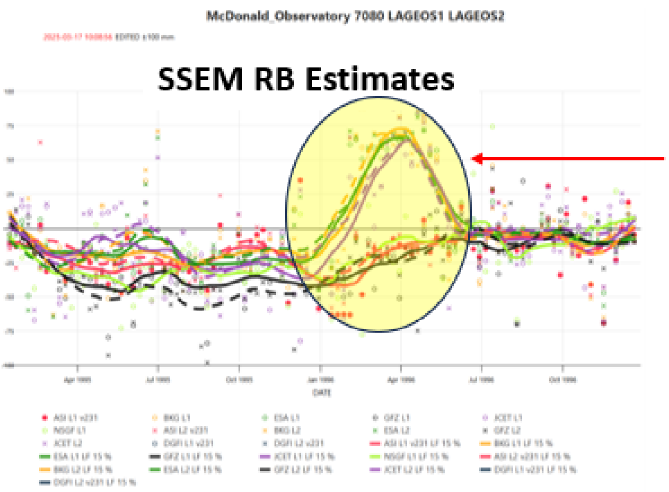

Issue:
RBs estimates vary by ACs;
Some ACs didn't apply tropo bias before RB estimation
End result:
Height Discontinuity

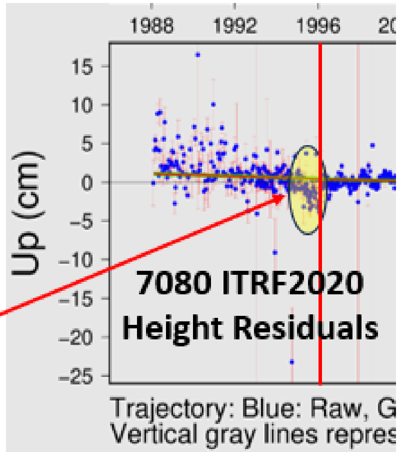

Solution: Always apply tropo/epoch biases *a priori* when estimating RBs

9

- This slide was presented to the QCB in Sep-2025
- Based on the DHF three of the Analysis Centers (BKG, ESA and JCET) did not apply *a priori* barometric correction before estimating a range bias that resulted in a 7080 MDOL ITRF2020 height discontinuity when the individual AC coordinate solutions were combined

Conclusions/Actions/Questions

- The NASA SLR DOC has implemented three new automated weekly barometric checks to flag
  - When the six-hour differences (station – VMF3o) in barometric pressure exceed +/- 4 mBars
  - When potential frozen pressures are detected
  - When there are inexplicable changes in barometric pressure within a CRD
- Calibrated barometric sensors are inherently more accurate than the VMF3o data. The VMF3o data, for most sites, when aggregated yearly is accurate to at least 0.4 to 0.6 mBars
- Are the seasonal trends in the six-hour differences (station – VMF3o) in the sensor and/or the VMF3o? If feasible, it is better to locate the barometric sensor in a controlled environment?
- Aggregating the six-hour pressures differences (station – VMF3o) can detect sudden jumps and drifts in our barometric measurements
- Would any of the station specific six-hour barometric VMF3o barometric differences be useful on the ILRS website?
- Need to develop barometric corrections for the ILRS DHF to fix legacy barometric errors
- Should there be a standard for how stations report their meteorological data? Should only one meteorological data record per CRD be flagged as a data integrity issue?
- Notify the ACs to check their software to determine if barometric pressure corrections are applied a priori before range bias estimation

ÖAW IWF

23RD INTERNATIONAL WORKSHOP ON LASER RANGING

Alternative normal point formation strategies for Galileo satellites

11 normal points instead of 1 normal point?

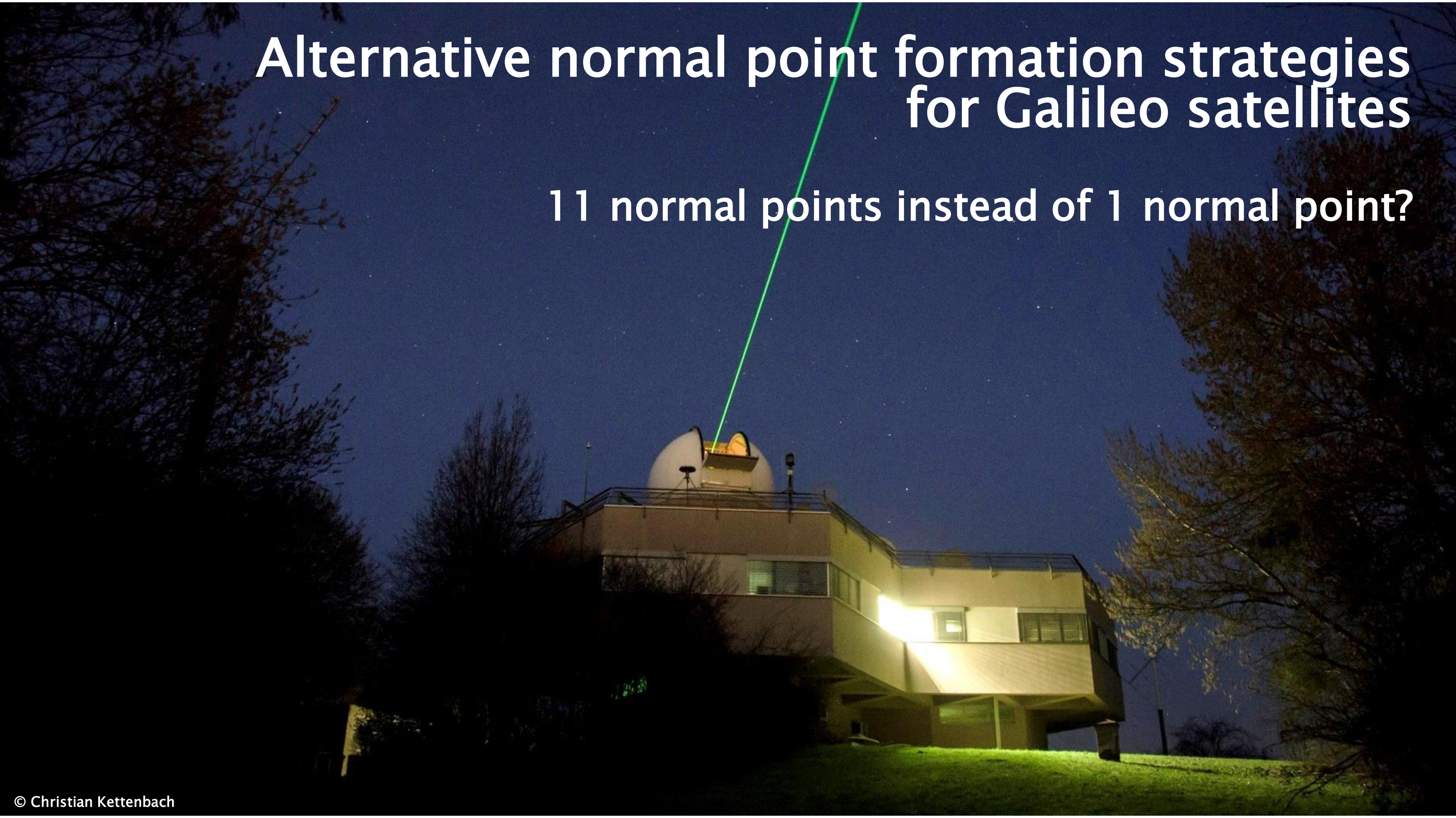

OVERVIEW

Principle

- Yaw steering: Satellites turn towards sun, twice per revolution
- Satellite-observer geometry: Multiple rows of reflectors align at constant ranges
- Symmetry conditions: dependent on hexagonal panel arrangement

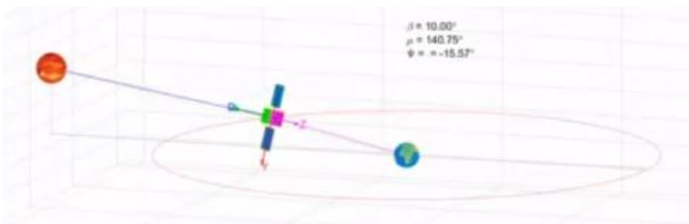

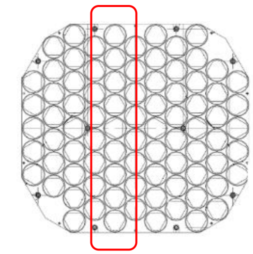

SLR data: row separation e.g. 7 mm

Effects on satellite laser ranging data

- Clustering of data at constant ranges
- SLR precision: mm-level
- Distance of alls rows can be identified
- -> better precison, incident angle

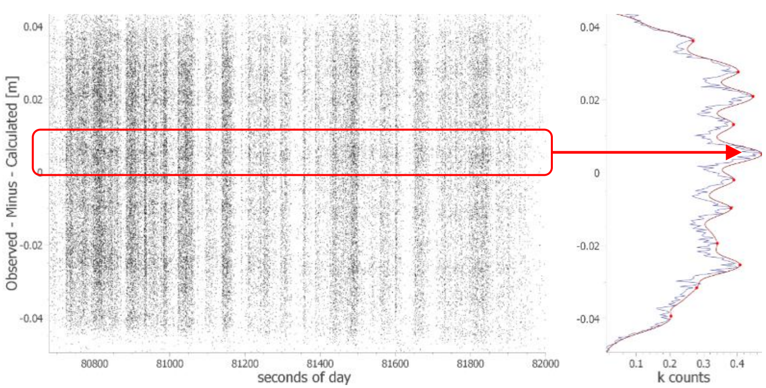

ESA contracts funded under H2020 programme

ÖAW IWF

GALILEO SYMMETRY CONDITIONS

Symmetry conditions explained

- 1) Rotate around screen axis by e.g. 30°, 60°, 90°
- 2) Tilt panel around symmetry axis -> rows separate from each other
- 3) Multiple CCRs at constant ranges: range separation based on tilt angle

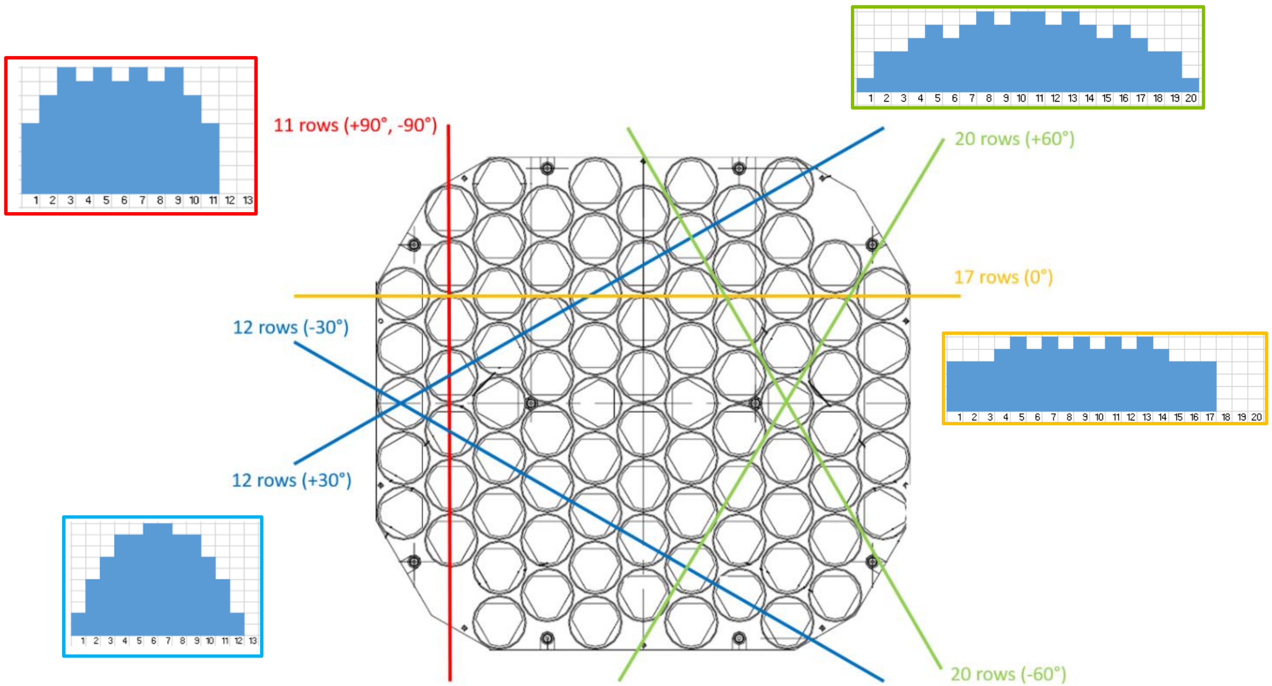

30°, 60° symmetry

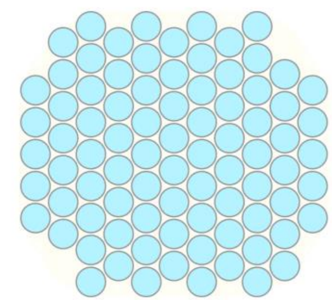

ESA contracts funded under H2020 programme

ÖAW IWF

O-C RESIDUAL SIMULATIONS

SLR simulation tool

- Predict SLR O-C range residuals [mm]
- Individual CCRs on Galileo panel color coded
- Different symmetry conditions: 90°, **60°**, **30°**
- Laser beam incident angle: 6°, 11.5°, 10°, 11°

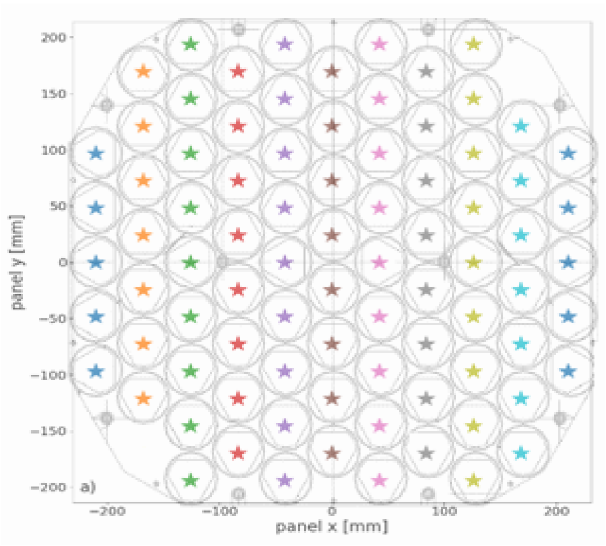

Full day: Galileo IOV

Retro reflector ranges

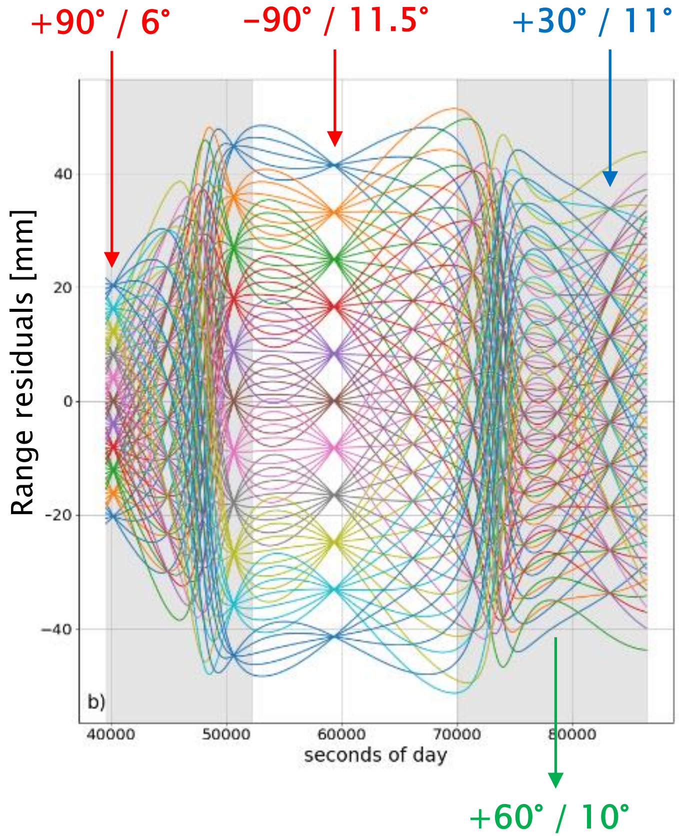

ÖAW IWF

Zoom in on 30° symmetry pass:
Residuals +/- 42 mm

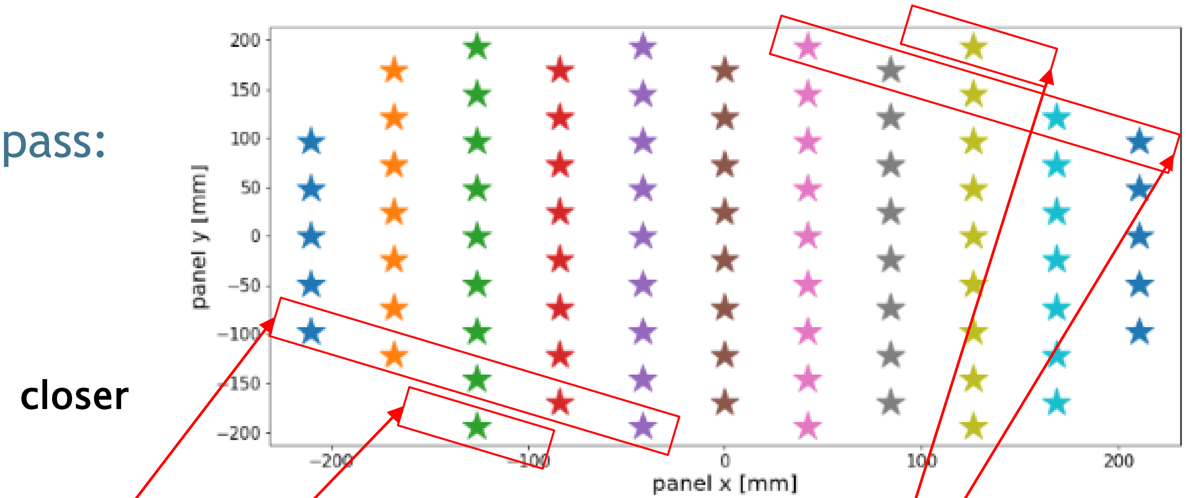

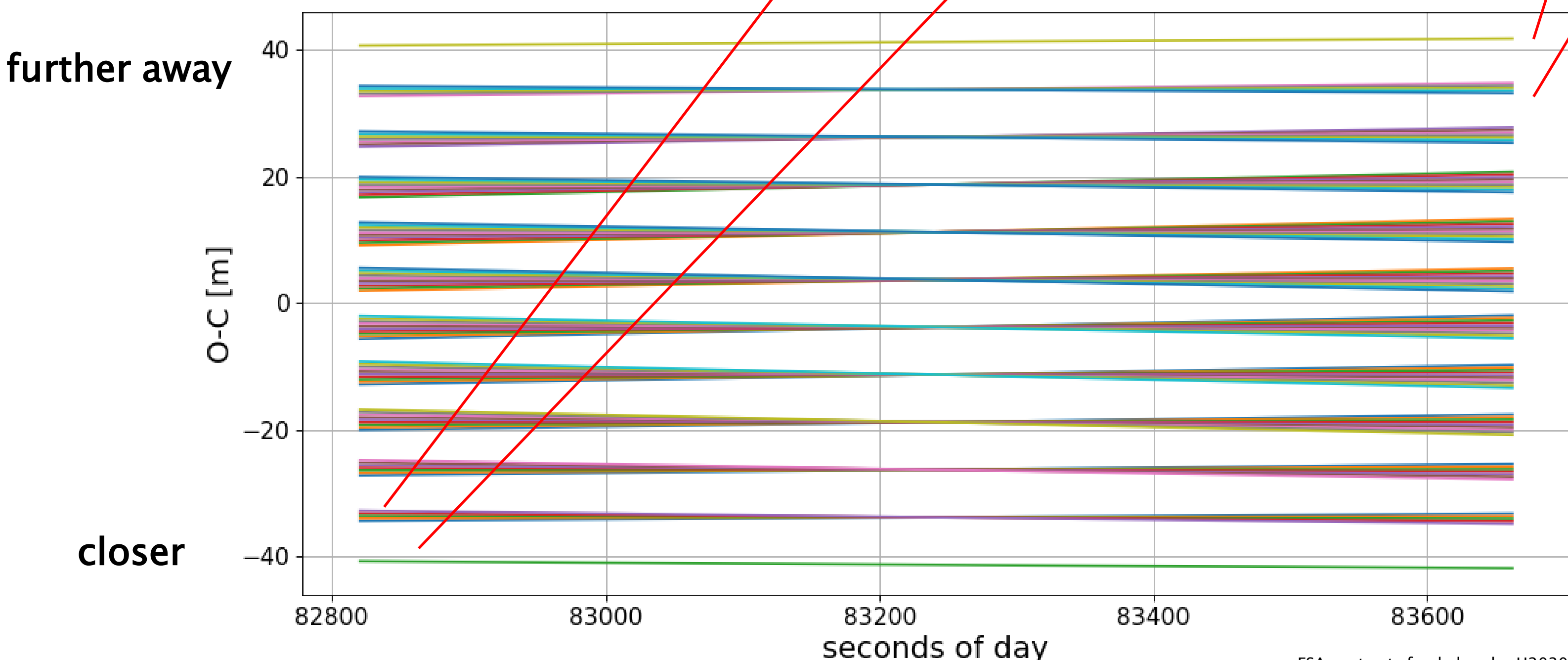

ESA contracts funded under H2020 programme

ÖAW IWF

GASP TOOL

GASP – Galileo Alert for Symmetry Passes

- Tool for Galileo symmetry pass prediction
- Observer gets alert 5 minutes before pass
- Campaign: >100 symmetry passes: within H2020 / ESA project

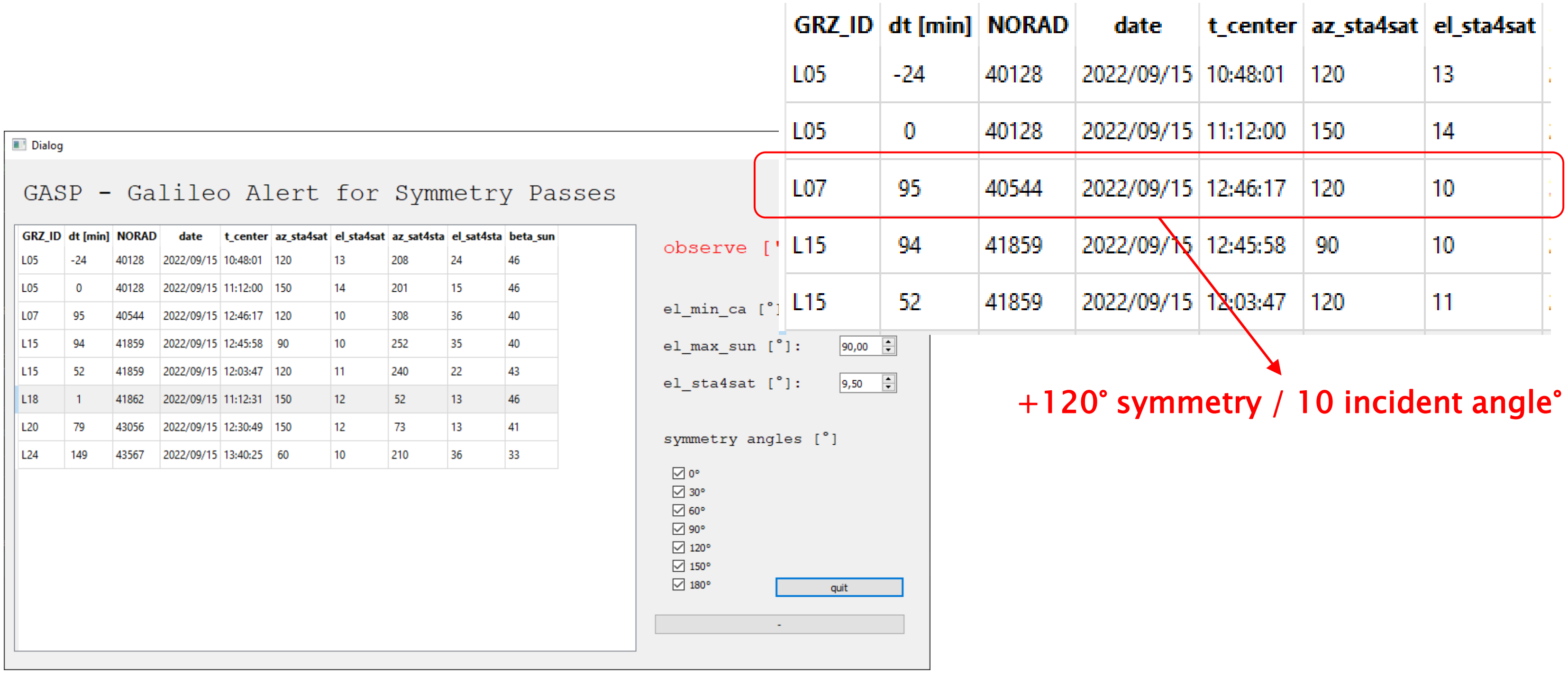
Dialog

GASP - Galileo Alert for Symmetry Passes

GRZ_ID	dt [min]	NORAD	date	t_center	az_sta4sat	el_sta4sat	az_sat4sta	el_sat4sta	beta_sun
L05	-24	40128	2022/09/15	10:48:01	120	13	208	24	46
L05	0	40128	2022/09/15	11:12:00	150	14	201	15	46
L07	95	40544	2022/09/15	12:46:17	120	10	308	36	40
L15	94	41859	2022/09/15	12:45:58	90	10	252	35	40
L15	52	41859	2022/09/15	12:03:47	120	11	240	22	43
L18	1	41862	2022/09/15	11:12:31	150	12	52	13	46
L20	79	43056	2022/09/15	12:30:49	150	12	73	13	41
L24	149	43567	2022/09/15	13:40:25	60	10	210	36	33

GRZ_ID	dt [min]	NORAD	date	t_center	az_sta4sat	el_sta4sat
L05	-24	40128	2022/09/15	10:48:01	120	13
L05	0	40128	2022/09/15	11:12:00	150	14
L07	95	40544	2022/09/15	12:46:17	120	10
L15	94	41859	2022/09/15	12:45:58	90	10
L15	52	41859	2022/09/15	12:03:47	120	11

ÖAW IWF

1) PEAK-BASED NORMAL POINTS

Normal point formation technique

- Normal point: compressed high-prescision SLR data (Galileo: 300 second interval)

1) Raw data

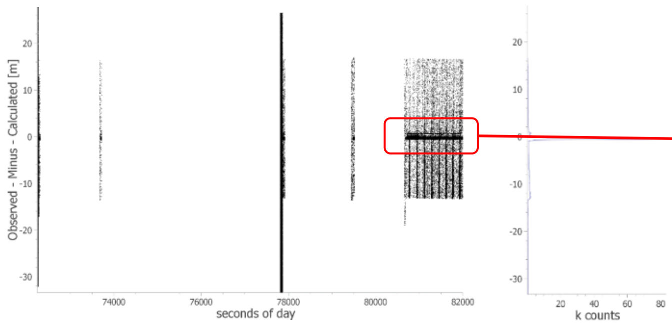

2) Cut raw data

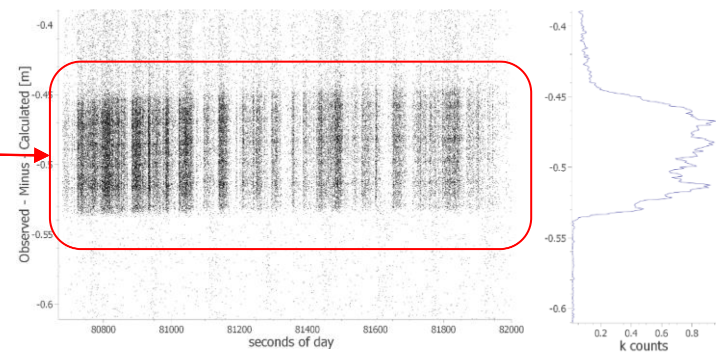

3) Orbit cleaning -> peak detection

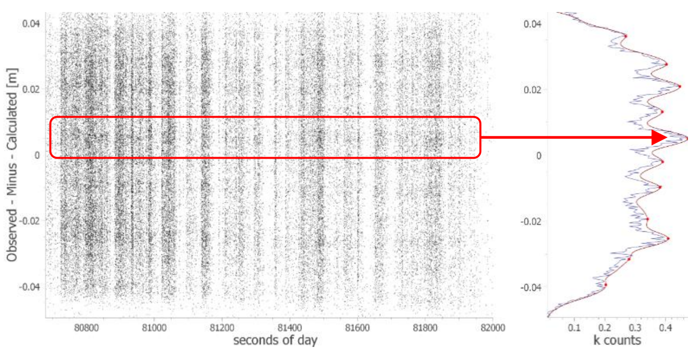

4) Cut individual rows -> form normal points

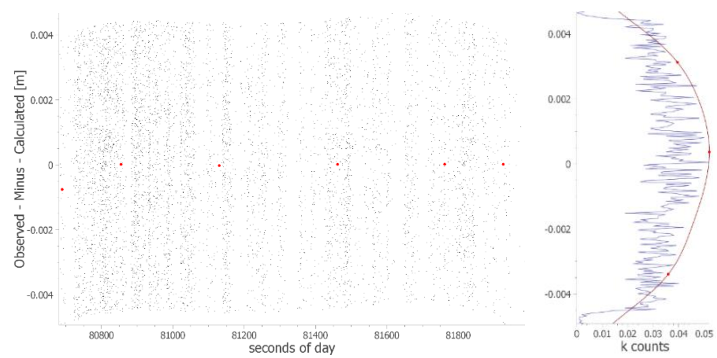

ESA contracts funded under H2020 programme

2) CORREATION NORMAL POINTS

- Calculate histogram of measured range residuals, calculate smoothed ranges
- Simulate SLR residuals of all 84 CCRs
- Calculate average CCR range in normal point interval
- Overlay Gaussian distribution at each of the CCRs positions (e.g. 2 mm SLR precision width)
- Add up 84 Gaussians distributions to one simulated distribution
- Calculate correlation: simulated function vs. measured data

Result: offset (correction) applied to regular normal point

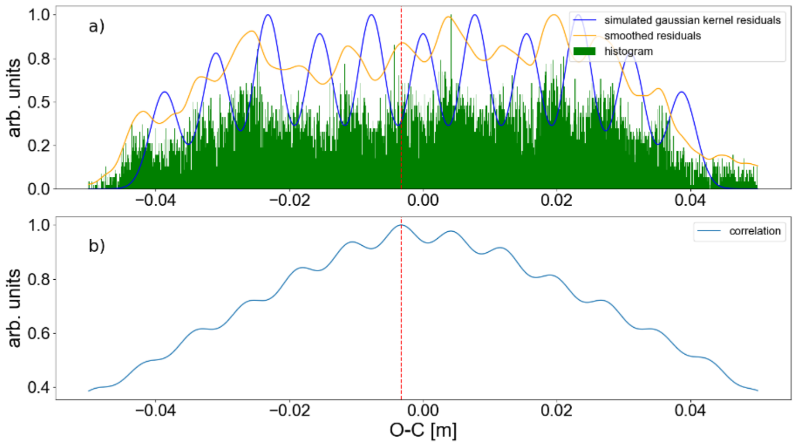

ESA contracts funded under H2020 programme

ÖAW IWF

PEAK / CORRELATION VS. REGULAR NP

Galileo 103

- +30° symm / 10 normal points

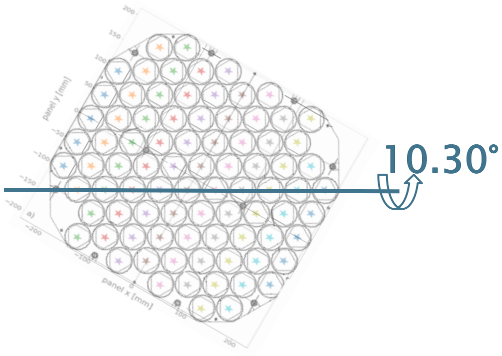

New normal points: 1 mm closer to POD orbit

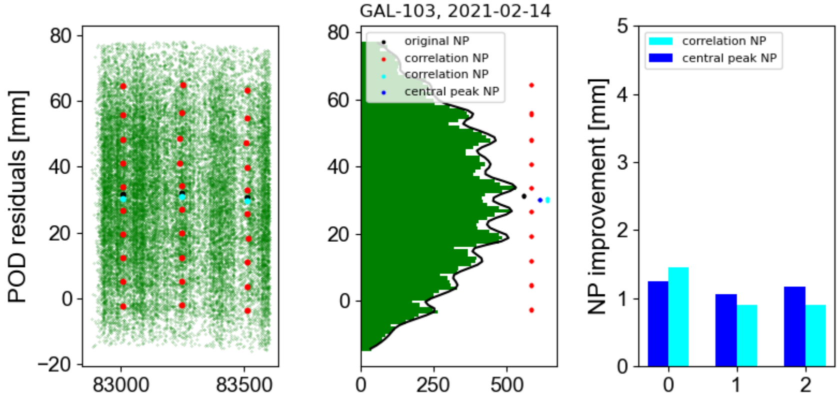

Galileo 102

- -90° symm / 11 normal points

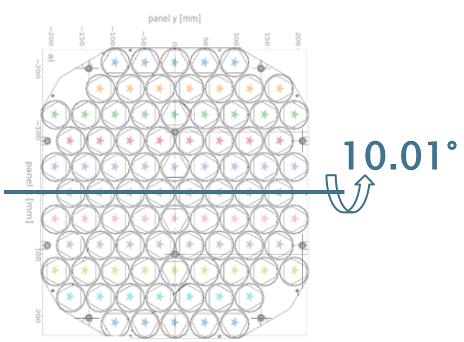

New normal points: 1 mm closer to POD orbit

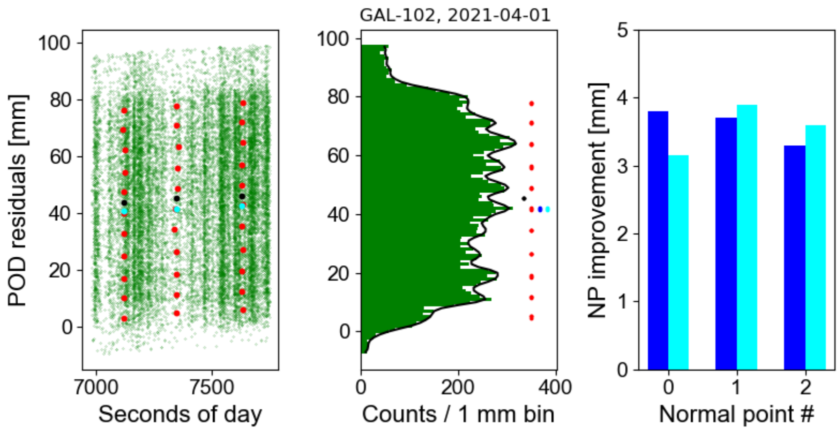

ESA contracts funded under H2020 programme

ÖAW IWF

INCIDENT ANGLE: GALILEO 103

Galileo 103: L0304520, +30° symmetry

- Range offset between rows measured -> laser beam incident angle
- Lomb analysis smoothed ranges: $\alpha_{pred} = 10.30°,\ \alpha_{calc} = 10.29°$

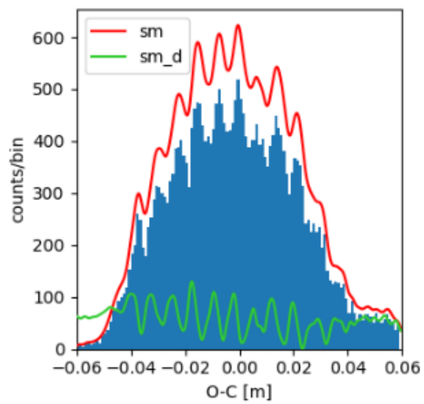

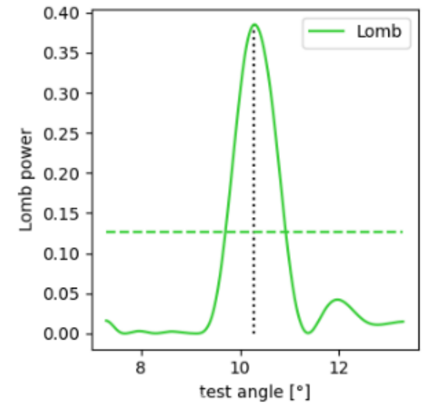

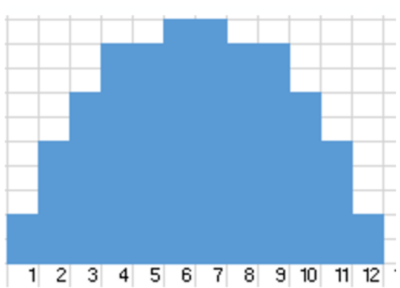

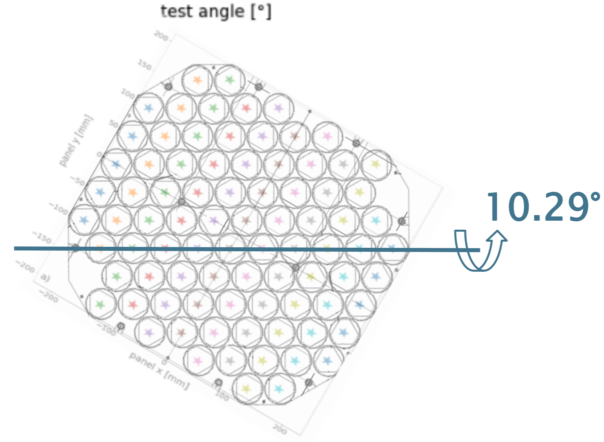

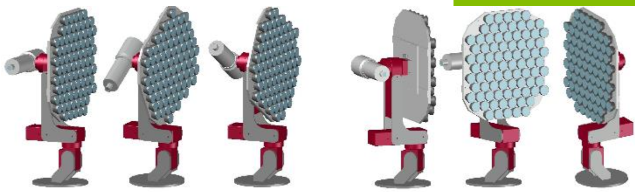

elevation = symmetry condition azimuth = incident angle

REMOTE MEASUREMENTS

- Remote Location: 32 km from Graz SLR station
- Spare IOV Panel: mounted on astronomical tripod
- Azimuth / elevation --> symmetry condition / incident angle

Laser: Graz SLR station

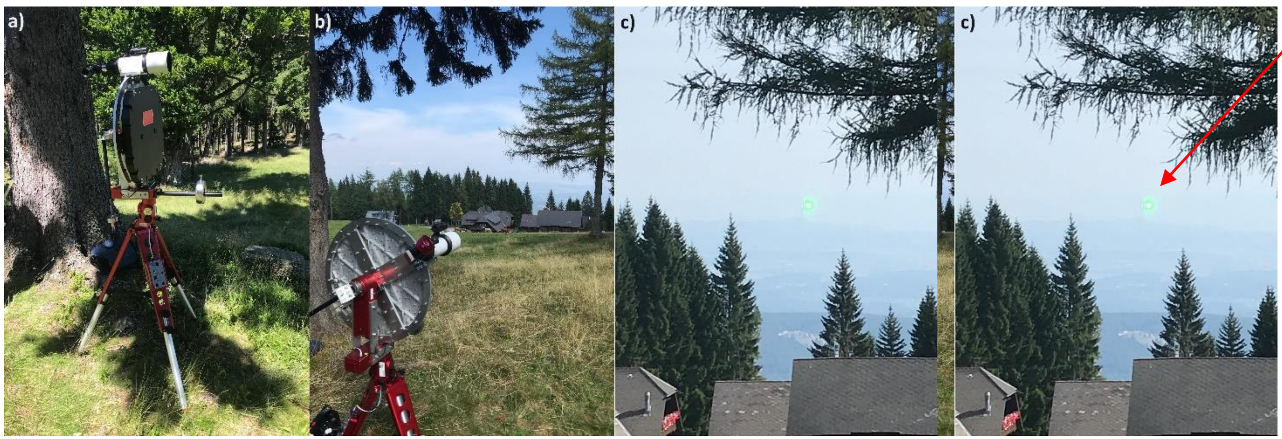

ÖAW IWF

SUMMARY

"The work reported in this paper has been performed and fully funded under a contract of the European Space Agency in the frame of the EU Horizon 2020 Framework Programme for Research and Innovation in Satellite Navigation. The views presented in the paper represent solely the opinion of the authors and should be considered as R&D results not necessarily impacting the present and future EGNOS and Galileo system designs"

Summarizing…

- Galileo Symmetry conditions
- Galileo Alert for Symmetry Passes tool
- Galileo SLR residual simulations
- Real data post-processing
- Incident angle calculations based on SLR data
- Alternative Normal point formation strategies (11 instead of 1 normal point?)
- Central normal points: closer to ESA POD orbit

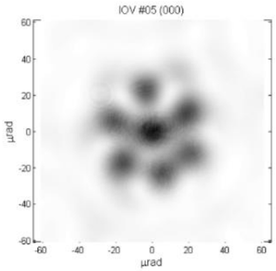

- FOC: Some interesting Galileo FOC histograms (201, 214, 217, 219) -> FFDP + clocking ?

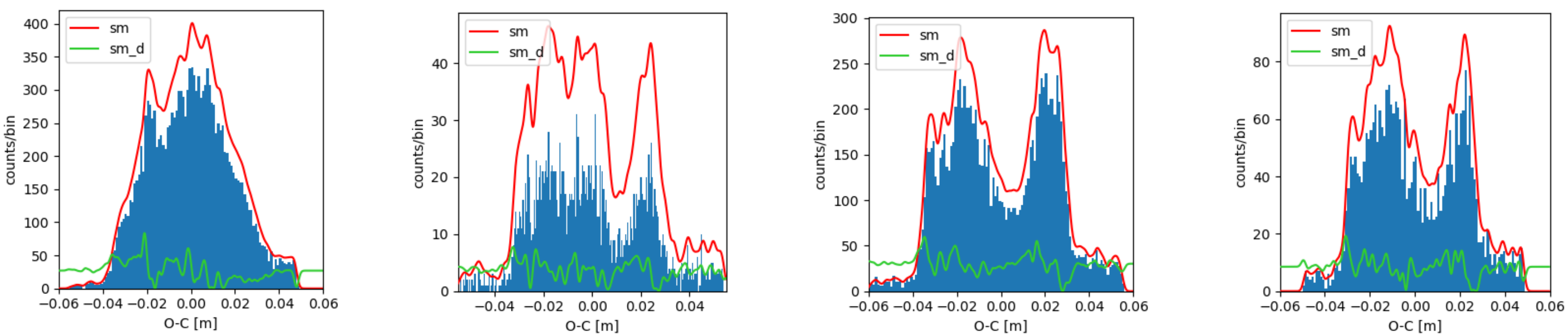

ÖAW IWF

! THANK YOU !

Theory says, eye-safe at 32 km… but: SAFETY FIRST

No cows were hit with the laser or harmed in any way during the measurement…

ILRS QCB Meeting

03/18/2026

Mike Croteau & Claudia Carabajal

ILRS

Agenda

Van:
- New Graz Data Screening Algorithm
- ILRS Barometric Analysis

Peter:
- Discussion on issues from examples of Station Performance.

Frank:
- Satellite interleaving (brief)

Mike/Claudia:
- Brief ILRS CB updates

Others?

Station Performance Guidelines

- Still need to review and update the 2023 Revised Performance Guidelines (revised after the launch of LARES-2)
  - Included in the 10/06/2025 meeting notes, sent to ILRS CB, and to ASC Chair/Co-Chair (no further inputs).
  - Final version (2025/2026) Performance Guidelines, shared with ASC; discussion at the last ILRS ASC meeting.

To be finalized after consensus is achieved, approved by ILRS GB, and published on the ILRS website, and disseminated to the community.

Station News: Station Surveys and Plan

- Review Team needs to reconvene, reviews of the Station Surveys and Plan (now 8).
- Provide feedback to the stations after discussions with the the review team.

Station News: Engineering Stations

Monument	Code	Location Name, Country	CDDIS SOD	IERS DOMES Numbers	IGS Site Log	IVS Site Log	IDS Site Log	Date of Latest Site Log	Date of Latest Site History Log
7040	OCTL	Wrightwood, California	70409201	49901S001	-	-	-	20050127	-
7125	GO1L	Greenbelt, Maryland	71259301	40451M114	X	X	X		-
7317	ISHL	Ishioka, Japan	73179501	21791M004	X	X	-	20250411	-
7395	GEOL	Geochang, Republic of Korea	73956501	23910S001	X	-	-	20170925	-
7816	SMIL	Stuttgart, Germany	78165202	10916S001	X	X	-	20221206	-
7826	STRK	Mt Stromlo, Australia	78269101	50119S007	X	-	X	20190813	-
7865	STAL	Stafford, Virginia	78658601	49654M001	-	-	-	20200312	20191015

- **No responses to date.**
- Discussions (ILRS CB/QCB) about having 'engineering' data in a different class, and putting the engineering station data to its own folder. **No updates.**

‘Engineering' stations may never meet the stringent quarantine data gathering and data quality requirements. Their data may always be in a quarantine folder, which many users never access. Having a unique category for engineering stations may impact NASA SLR Data Operations. **Still desired?**

Mission Updates/New Missions:

NanoFF B:

- Tracking for the **NanoFF B** satellites campaign started on September 29th, 2025.
- Satellite included in Time Bias service.
- Mission will let ILRS CB know when tracking of **Nano-FF-A** will start. Distance between the spacecrafts is now between 50 km - 100 km.

Mission page:
https://ilrs.cddis.eosdis.nasa.gov/missions/satellite_missions/current_missions/nanoFF_general.html

HTV-X:

- The HTV-X will transfer essential cargo such as large-sized devices for the ISS and life support goods for astronauts. The costs for the HTV-X will be cut down through compact designing and efficient operations. Moreover, the HTV-X will be designed to become more useful for owners of experiment devices on earth.
- HTV-X will also be able to propose solutions to national challenges and take part in innovations by conducting experiments for acquisition of new technologies even outside of space business.
- **Launched October 26, 2025. ILRS CB assigned the SIC 1559. Tracking began after release from the ISS to start March 12th, 2026 through early-April 2026.**
- For more details, please refer to https://humans-in-space.jaxa.jp/en/htv-x/specifications/

QPS-SAR10:

- Launched May 17th, 2025. Support started in August 2025 (restricted tracking). Simosato and Grasse added to stations supporting the mission.

Mission Updates/New Missions:

e-kagaku-1

- Proved difficult to track; satellite is magnetized internally, so it flies in an orientation aligned with the Earth's magnetic field. Mission provided website with visibility for statiosn. Predictions no longer provided.

Sentinel-6B/Jason CS-B

- Launched November 17th, 2025. Sentinel-6/Jason-CS mission is a joint oceanography mission to monitor global ocean circulation and sea-level. The Sentinel-6B/Jason-CSB satellite is the follow-on to the TOPEX/POSEIDON, Jason-1, Jason-2, Jason-3 and Sentinel-6A/Jason-CSA satellites.
- ILRS CB assigned SIC 4382. Tracking started December 16th, 2025, when the satellite reached the mission orbit.

GPS-III SV09 & SV10 (USA Space Force):

- GPS III satellites are used to keep the Navstar Global Positioning System operational, to modernize the existing system to respond to advances in technology and new demands. GPS III will deliver sustained, reliable GPS capabilities to America's warfighters, our allies, and civil users. The project involves new ground stations and new satellites, with additional navigation signals for both civilian and military users and aims to improve the accuracy and availability for all users. GPSIII SV09 is the ninth GPS Block III satellite.
- Launched 28 January, 2026, by SpaceX atop a Falcon 9 rocket from SLC-40 at Cape Canaveral Space Force Station.
- Tracking started December 16th, 2025, when the satellite reached the mission orbit.

Mission News: ICESat-2 tracking by new stations

- Scott Luthcke and his team requested that we check on a few stations and see if we can add a few more. They will need to be evaluated by the mission once the current System Parameters are provided, to see if they can safely track ICESat-2.
    - San Fernando – SFEL (San Fernando, Spain); recently passed quarantine, new improved system. Had to work out software. **No agreement signed yet.**
    - SOSW - 7827 (Wettzell, Germany); hasn’t tracked since late 2020.
    - ZIML - 7810 (Zimmerwald, Switzerland);
    - HARL - 7501 (Hartebeesthoek, South Africa); no tracking from 2022-2023, resumed tracking in 2024, but recently hasn't tracked since late 2024.
    - MDOL - 7080 (McDonald Observatory, Texas); on our approved stations list, but hasn’t tracked throughout the mission.

  Checking on the status for each one, to report back to Scott. Analysis by the mission and Agreements needed before tracking can begin.

Tracking Campaigns:

GALILEO for Science :

- Campaign ended at the end of February 2026.

Galileo for Science Campaign Pass Totals (Aggregate)																
Pad	Location	101	102	103	201	202	203	205	206	208	209	210	211	212	221	**Total**
1873	Simeiz						1	1				1				**3**
1874	Mendeleevo 2								1			1				**2**
1884	Riga		21	26	26	18	18	28	23	13	19	31	26	14	19	**282**
7090	Yarragadee	321	322	328	305	279	130	132	166	156	235	183	242	149	149	**3097**
7105	Greenbelt	11	83	14	46	49	29	26	25	47	62	47	50	41	58	**588**
7110	Monument Peak	10	24	13	10	28	19	23	26	21	20	26	9	21	19	**269**
7124	Tahiti		2		3		2			2		1		2		**12**
7237	Changchun	177	173	165	139	138	174	130	130	157	156	125	117	160	163	**2104**
7249	Beijing	67	82	46	70	57	76	52	54	46	38	44	45	49	68	**794**
7306	Tsukuba	53	58	53	51	50	50	37	39	38	44	33	34	38	43	**621**
7329	Xian	21	20	21	21	22	22	13	26	15	18	19	21	14	24	**277**
7396	Wuhan	47	45	48	42	50	48	42	59	40	26	50	46	40	54	**637**
7501	Hartebeesthoek		1													**1**
7701	Izana	30	34	33	31	37	20	23	26	31	33	24	32	31	24	**409**
7810	Zimmerwald	28	35	46	33	27	18	23	30	33	28	32	25	24	22	**404**
7811	Borowiec	1		4	5	1	1		1	6	2	1				**22**
7817	Yebes	11	8	15	12	9	6	12	19	14	11	19	23	15	16	**190**
7819	Kunming	160	170	176	147	167	172	141	147	170	172	135	133	163	177	**2230**
7821	Shanghai	98	97	94	75	69	65	77	90	89	78	74	86	70	91	**1153**
7825	Mt Stromlo		161		144	146	84	75	58	51	140	66	88	36	17	**1066**
7827	Wettzell	42	42	40	42	55	34	41	41	30	37	36	44	37	35	**556**
7838	Simosato		7		7	5					2		7			**28**
7839	Graz	142	139	136	150	141	136	113	135	127	113	136	129	112	130	**1839**
7840	Herstmonceux	106	155	112	124	170	93	105	107	117	173	128	106	112	94	**1702**
7841	Potsdam	85	77	91	75	70	69	69	81	59	67	61	75	68	73	**1020**
7845	Grasse	111	98	95	139	132	73	92	115	92	112	114	97	82	88	**1440**
7941	Matera	38	166	40	250	228	33	32	39	41	111	146	147	34	50	**1355**
8834	Wettzell	18	212	153	179	208	155	124	138	108	187	123	171	118	133	**2027**
	Totals	1678	2334	1852	2327	2358	1731	1616	1782	1711	2093	1866	1964	1642	1768	**24128**

Reports: https://ilrs.gsfc.nasa.gov/science/SLR_science_campaigns/galileo_for_science.html

Meetings:

- AGU 2025: Magda et al. single presentation from NASA/UMBC/JCET AC.
- ILRS GB (February 19th, 2026)
  - ILRS CB Director's position transition: Mike Pearlman (outgoing), Mike Croteau, new ILRS CB Director.
  - GMV request to stations for tracking of Galileo satellites
  - LLR Observations and data availability, and tracking of LAGEOS-1/-2 and LARES-2 by the Apollo LLR station
  - ILRS Elections
- GENESIS SLR WG5 Meeting (February 2026)
- REFAG2026 Symposium (March 2-3-4, 2026)
- UAW Munich (March 5-6, 2026) (first week of March, 2026)
- GENESIS Calibration and Science Workshops (March 11-12-13, 2026)

Report

- Worked on Reports for NASA Space Geodesy Project (SGP) on Station Performance, ILRS support, and ILRS products updates for 2025.
- Request to update the ILRS Report for the IAG EC Meeting (to deliver by Cinzia after the meeting occurred, she was not in attendance).

GPS Solutions (2024) 28:73
https://doi.org/10.1007/s10291-024-01615-9

ORIGINAL ARTICLE

Satellite laser ranging to Galileo satellites: symmetry conditions and improved normal point formation strategies

Michael A. Steindorfer[1] · Franz Koidl[1] · Georg Kirchner[1] · Peiyuan Wang[1] · Florian Dilssner[2] · Erik Schoenemann[2] · Aaron Strangfeld[3] · Francisco Gonzalez[3]

Received: 28 September 2023 / Accepted: 12 January 2024 / Published online: 16 February 2024

Abstract

High-precision satellite laser ranging measurements to Galileo retroreflector panels are analyzed to determine the angle of incidence of the laser beam based on specific orientations of the panel with respect to the observing station. During the measurements, the panel aligns with respect to the observing station in such a way that multiple retroreflectors appear at the same range, forming regions of increased data density—separated by a few millimeters. First, measurements to a spare IOV-type retroreflector mounted on an astronomical mount at a remote location 32 km away from the Graz laser ranging station are performed. In addition, more than 100 symmetry passes to Galileo satellites in orbit have been measured. Two novel techniques are described to form laser ranging normal points with improved precision compared to traditional methods. An individual normal point can be formed for each set of retroreflectors at a constant range. The central normal point was shown to be up to 4 mm more accurate when compared with a precise orbit solution. Similar offsets are determined by applying a pattern correlation technique comparing simulated with measured data, and the first method is verified. Irregular reflection patterns of Galileo FOC panels indicate accumulated far-field diffraction patterns resulting from non-uniform retroreflector distributions.

Keywords Galileo · Satellite laser ranging · Attitude determination · Retroreflector · Far field diffraction pattern · Normal point

Introduction

Satellite laser ranging (SLR) over the last decades has continuously aimed to improve accuracy and precision. Most SLR stations are, however, locally organized and apply improvements and changes (hardware, software or post-processing) to the system individually, which also influences data precision and has to be carefully considered e.g. by data analysis centers. Satellites hosting different arrangements of retroreflectors while being illuminated from different angles or laser beam polarizations can introduce changes in the distribution of detected photons, which then potentially affect the precision if not considered during post processing. To make use of these signature effects for improvements is a promising approach and was already demonstrated multiple times in the SLR community e.g. for geodetic satellites but also for navigation satellites (Otsubo et al. 2001) as well as by analyzing up to decades of SLR data (Sośnica et al. 2015). This research focuses on signature effects within Galileo data, which can be utilized to improve SLR precision further.

SLR measures the range to satellites equipped with corner cube retro reflectors (CCRs) by precisely timing the time of flight of the reflected laser pulses. Since the first measurements in 1965 the precision of SLR has improved significantly. With the use of single photon avalanche diode (SPAD) detectors, picosecond pulse length lasers and precise timing and calibration, single shot precision now reaches approximately 3 mm. Measured satellites include geodetic, scientific or Global Navigation Satellite System (GNSS) satellites.

✉ Michael A. Steindorfer
michael.steindorfer@oeaw.ac.at

1 Space Research Institute, Austrian Academy of Sciences, Schmiedlstraße 6, 8042 Graz, Austria

2 European Space Agency, ESA/ESOC, Robert-Bosch-Str. 5, 64293 Darmstadt, Germany

3 European Space Agency, ESA/ESTEC, Keplerlaan 1, 2201 AZ Nordwijk, The Netherlands

Currently there are four GNSS constellations in the world. The United States' Global Positioning System (GPS) was the first to be established, dating back to 1978. The Russian Global'naya Navigatsionnaya Sputnikovaya Sistema (GLONASS) was launched four years later. China started its Beidou system in 2000. The first launch of the In Orbit Validation (IOV) satellites of the European Galileo system was in 2011 (European GNSS Supervisory Authority 2020). India and Japan have their own regional systems based on satellites in geostationary and geosynchronous orbits.

The current generation of Galileo, BeiDou and GLONASS satellites carry a CCR panel hosting up to 90 reflectors. The arrangement of the CCRs on the panel varies from circular, ring shaped to hexagonal or rectangular arrangements (Pearlman et al. 2002). Galileo IOV-type panels include 84 CCRs arranged hexagonally with 33 mm minimum aperture, FOC (Full Orbit Capacity) satellite have only 60 CCRs with 28.2 mm minimum aperture and hence lower optical cross section (ILRS 2023). Depending on the relative motion of the satellite with respect to the observer, the center of the reflection pattern of each individual CCR is shifted toward the direction of flight of the spacecraft. This so-called velocity aberration depends on the orbit and—especially for lower orbits—also on the elevation of the satellite in the sky and can vary between 20 µrad and 50 µrad. Due to the larger distances, the velocity aberration for GNSS orbits is approximately constant in the order of 25 µrad (Degnan 2012). Typically, larger CCR diameters on the order of 3–4 cm are used for GNSS satellites. Based on diffraction laws, CCRs are chosen so that a large fraction of the reflected energy is directed at an angle close to the velocity aberration defined by the orbit. (Nugent and Condon 1966) Further modification of the far-field diffraction pattern (FFDP) (Degnan 2012) can be achieved by intentionally misaligning the back surface—typically dihedral angles (Chandler 1960; Thomas and Wyant 1977) of 2 µrad or more shift the reflected energy from the central to the outer regions of the FFDP. The rear reflective surfaces of GNSS satellites are mostly uncoated, resulting in a hexagonal reflection pattern (Arnold 2002). The front surfaces are either broadband-coated or coated specifically for SLR wavelengths.

SLR provides an independent, purely passive technique that can be used to study the systematic effects of different techniques (Luceri et al. 2019; Thaller et al. 2015), to validate orbits (Thaller et al. 2011; Strugarek et al. 2022; Zajdel et al. 2023), to generate combined and improved orbits (Bury et al. 2018), to analyze solar radiation pressure (Kucharski et al. 2017), or to perform time transfer (Samain et al. 2015).

SLR is a technique that reliably contributes (Sośnica et al. 2014) to the International Terrestrial Reference Frame (ITRF), with new developments towards a laser ranging reference frame (SLRF) recently announced (SLRF 2020). Important parameters connected to SLR are Earth rotation, gravity field, center of mass or polar motion. Scientific missions that rely on SLR data include oceanic motions, Earth topography, sea level variations, and Earth magnetic field or ice masses. Relativistic experiments (gravitational redshift, dark matter, Lense-Thirring effect) could be performed using different satellites (Delva et al. 2019; Ciufolini et al. 2019). Future trends in the laser ranging community include further increasing the repetition rate (Dequal et al. 2021; Wang et al. 2021; Long et al. 2022), possibly performing mm-precision laser ranging of satellites and space debris (Cordelli et al. 2020; Steindorfer et al. 2020) with one system.

The precision of SLR measurements depends on several factors such as sensor type and characteristics (single vs. multi-photon detectors), laser pulse width, event timing or calibration. In addition, the satellite signature and its analysis play an important role in further improving the precision further. SLR stations capable of detecting single photons with sufficient precision are even able to identify single CCRs of low flying satellites. Geodetic satellites have a specific return signal profile that is used to filter out the reflected photons that always correspond to the same region of the satellite—the leading edge.

Galileo orbits currently reach sub-cm-level accuracies (Dilssner et al. 2022), the panels also show different reflection profiles (Degnan 2012) which depend on the panel orientation (Steindorfer et al. 2019), the angle of incidence of the laser beam (Murphy Jr. and Goodrow 2013), laser polarization (Arnold 2002), thermal effects (Dell'Agnello et al. 2012; Boni et al. 2011), return rate and detector type (Kirchner et al. 1999; Kodet et al. 2009; Prochazka et al. 2020). Gaps in the individual FFDP distributions are counteracted by rotating the individual CCRs (clocking) (Dell'Agnello et al. 2011), which can lead to additional signal strength variations when looking at the overall pattern. Satellite signatures (Kucharski et al. 2015) can, therefore, influence the mean reflectance point of the Galileo panel, as the dataset of the entire panel is currently used in the post-processing of the laser ranging data. More photons from the front of the panel will therefore also shift the measurement towards closer ranges.

We investigate alternative measurement and normal point formation techniques. The first is the peak method, which is based on panel orientations where multiple CCRs are aligned at equal ranges with respect to the observing station. These so-called symmetry conditions can be accurately predicted by adding yaw steering to nadir pointing Galileo satellites (Montenbruck et al. 2015). For these passes the satellite signature is characterized and since the panel geometry is known, individual normal points can be formed for each of these ranges. The second method is the pattern correlation method (Brunelli 2009). The expected return pattern of the residuals is correlated with the observed one to identify the center position of the panel and to form the normal points.

The two techniques are compared with respect to the current method based on example passes.

Materials and methods

In the following chapter, the basics of SLR, SLR residual simulations, Galileo symmetry simulations and the measurement setup will be summarized. Simulation and observation results from four different satellites are shown and referred to by Name (Type, PRN, Norad): Galileo 101 (IOV, E11, 37846), Galileo 103 (IOV, E19, 38857), Galileo 213 (FOC, E04, 41861), Galileo 219 (FOC, E36, 43566). However, all Galileo satellites up to Galileo 219 were observed during the observation campaign.

Satellite laser ranging—measurement

Satellite laser ranging provides precise range measurements to Earth-orbiting satellites equipped with CCRs. The worldwide network of laser ranging stations is globally distributed and coordinated by the International Laser Ranging Service (ILRS). Data centers collect the data, make it publicly available and publish frequently updated orbit predictions of the satellites. Different stations follow various approaches with respect to laser and detector technology. Low repetition rate stations fire laser pulses at about 10 Hz, each pulse with an energy in the order of 100 mJ, resulting in multiple photons reflected back from the target significantly favoring the closest CCRs. High repetition rate stations use repetition rates of about 2 kHz. Pulse energies are much lower, e.g. 400 µJ for the Graz SLR station. This increases the data rate and due to the statistical distribution of the reflected photons operating single photon return rate, multiple retroreflectors can be identified in the data. To reduce the divergence of the laser beam leaving the SLR station, beam expansion optics are used to expand the laser beam to 5 cm and beyond. Some stations use a separate lens-based beam expander. Common transmit-receive stations use the same large mirror-based telescope for beam expansion and reception of reflected photons reducing the divergence to values below the atmospheric seeing, which then becomes the limiting factor in terms of return rate. Pulse durations are typically in the order of 10 ps, resulting in optimal single shot measurement precision of up to 3 mm. Laser ranging with such a precision naturally requires precise timing of the events of the photon leaving the station and returning back after reflection (event timing). Detector technology includes microchannel plates, photomultipliers or single photon avalanche diodes. Depending on the signal strength reflected back to the station, receiving telescopes with different apertures are used (typically about 50 cm diameter). With larger apertures, precise pointing and increased laser power, lunar laser ranging is also performed by a few stations. Space debris laser ranging was first demonstrated in the years of the twenty-first century and relies on the diffuse reflection of photons over the entire space object by firing higher laser powers (> 10 W). Diffuse reflections provide an indication of the size and shape of the objects. For both laser ranging and space debris laser ranging, range variations can be used for spin period and attitude determination purposes.

Satellite laser ranging—residual simulations

Earth-orbiting satellites maintain a constant orientation with respect to a given coordinate frame. Nadir-pointing GNSS satellites are orientated with their navigation antenna pointing toward the center of the Earth (radial component), the second coordinate axis pointing in the direction of flight (velocity vector, along track) and the third component out of the orbital plane (cross product of velocity and along track component). For Galileo satellites, yaw-steering is implemented to allow the solar panels to face the sun. The yaw steering frame (YSF) is also nadir pointing but the axes $\boldsymbol{e}_{x,YS}, \boldsymbol{e}_{y,YS}, \boldsymbol{e}_{z,YS}$ are calculated using the following formulas,

$$\boldsymbol{e}_{y,YS} = \frac{\boldsymbol{e}_{\mathrm{sun}} \times \boldsymbol{r}_{\mathbf{sat}}}{|\boldsymbol{e}_{\mathrm{sun}} \times \boldsymbol{r}_{\mathbf{sat}}|} \tag{1}$$

$$\boldsymbol{e}_{z,YS} = -\frac{\boldsymbol{r}_{\mathbf{sat}}}{|\boldsymbol{r}_{\mathbf{sat}}|} \tag{2}$$

$$\boldsymbol{e}_{x,YS} = \boldsymbol{e}_{y,YS} \times \boldsymbol{e}_{z,YS} \tag{3}$$

where $\boldsymbol{e}_{\mathrm{sun}}$ is the unit vector pointing from the satellite to the sun and $\boldsymbol{r}_{\mathbf{sat}}$ is the satellite position vector. Other reference coordinate frames of importance are the inertial Geocentric Celestial Reference Frame (GRCF), which is defined with respect to the stellar background, and the geocentric International Terrestrial Reference Frame (ITRF). The True Equator Mean Equinox (TEME) is an intermediate frame—the output of the Simplified General Perturbation 4 (SGP4) propagation used to obtain satellite predictions based on Two Line Element (TLE) data sets.

To acquire simulated SLR data the following steps are implemented:

(1) Satellite orbit predictions: sources e.g. TLE, CPF (Consolidated Prediction Format, a data format used within the SLR community); time intervals: e.g. 60 s
(2) Lagrange interpolation: saves computation time; allows shorter time steps; e.g. 1 s
(3) CCR parameter definition: 3D position, normal vector, field of view; defined with respect to the center of mass or the geometrical center of the panel

(4) Optional: define rotation parameters; spin axis, spin period, initial orientation; rotate satellite
(5) SLR residual calculation: (Rotated) CCR positions are added relative to a reference coordinate frame (RCF); e.g. YSF, GCRS, nadir, …
(6) Observed-Minus-Calculated (O-C) residual calculation: Difference between CCR ranges and reference orbit predictions

In the following the YSF will be used as the reference frame, since the goal of this study is to analyze the Galileo SLR residuals.

Galileo symmetry conditions

As the Galileo satellites change their yaw orientation throughout the orbit, special “symmetry conditions” occur with respect to the observing ground station, where several CCRs appear at the same distance (Fig. 1). The panel orientation relative to the ground station is characterized by two parameters.

α_{symm}: The symmetry angle that defines the orientation of the symmetry axis around which the panel appears rotated with respect to the observing station. The symmetry angle is defined as the angle of the rotation axis relative to the horizontal x-axis. For our simulations and measurements the symmetry angles of interest are $\alpha_{symm} = 0°, \pm30°, \pm60°, \pm90°$ as defined by the hexagonal arrangement of the Galileo panel.

α_{laser}: The tilt of the panel relative to the observer is then characterized by a rotation around the previously defined symmetry axis. This tilt also describes the angle of incidence of the laser beam on the panel.

During the residual simulations α_{symm} is calculated by first projecting the vector pointing from the station to the satellite $\boldsymbol{r}_{sat-sta} = \boldsymbol{r}_{sat} - \boldsymbol{r}_{sta}$ onto the plane given by the Galileo panel. The projection $\boldsymbol{u}_{n}$ of a vector $\boldsymbol{u}$ onto the plane defined by the normal vector $\boldsymbol{n}$ is given by

$$\boldsymbol{u}_{n} = \boldsymbol{u} - \frac{\boldsymbol{u}\,\boldsymbol{n}}{||\boldsymbol{n}||^{2}}\boldsymbol{n} \quad (4)$$

The angle between this projected vector and the yaw steering vector $\boldsymbol{e}_{x,ys}$ now defines the symmetry angles α_{symm}. The incident angle α_{laser} of the laser beam is simply the angle between $\boldsymbol{r}_{sat}$ and $\boldsymbol{r}_{sat-sta}$.

In other words, α_{symm} and α_{laser} are the azimuth and elevation angles of the SLR station as seen from the Galileo panel. For Galileo orbits (except for the two eccentric orbits) the incident angle cannot exceed $\alpha_{tilt} = 12.5°$.

Applying the result from the previous chapter, it is possible to simulate the SLR residuals for half a day for Galileo 103 (Fig. 2). The individual CCRs are color coded based on the 90° symmetry condition, which means that all CCRs of the same color for this specific symmetry angle will appear in constant range (Fig. 2a). The residual simulations (Fig. 2b) clearly show that the CCRs come together at a constant range at certain times, and then move apart. A − 90° symmetry condition occurs just before the second of day 60,000. A + 30° symmetry condition occurs at second of day 83,000 which causes differently colored CCRs to join together. The overall distribution of the residuals varies between ± 20 and ± 45 mm which directly correlates to the incident angle of the laser beam. The elevation and azimuth of the satellite (as seen from the station) show two grayed out areas where the satellite is above the station horizon (Fig. 2c). Furthermore, the symmetry angle and the laser

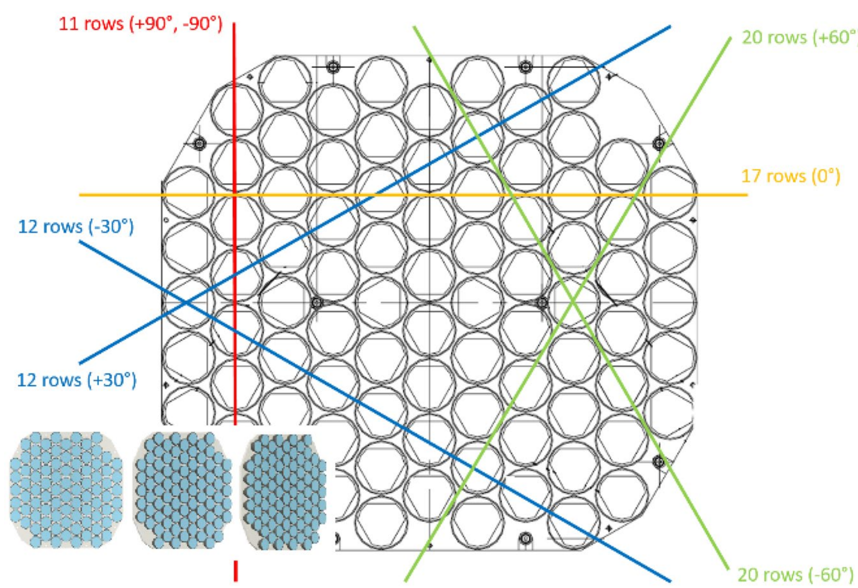

Fig. 1 Potential symmetry conditions on a Galileo IOV panel. Relative to the *x*-axis, symmetry angles of 0°, ± 30°, ± 60°, and ± 90° are indicated in different colors. The insert illustrates the tilt of the panel letting individual rows appear at constant range with respect to the observing station

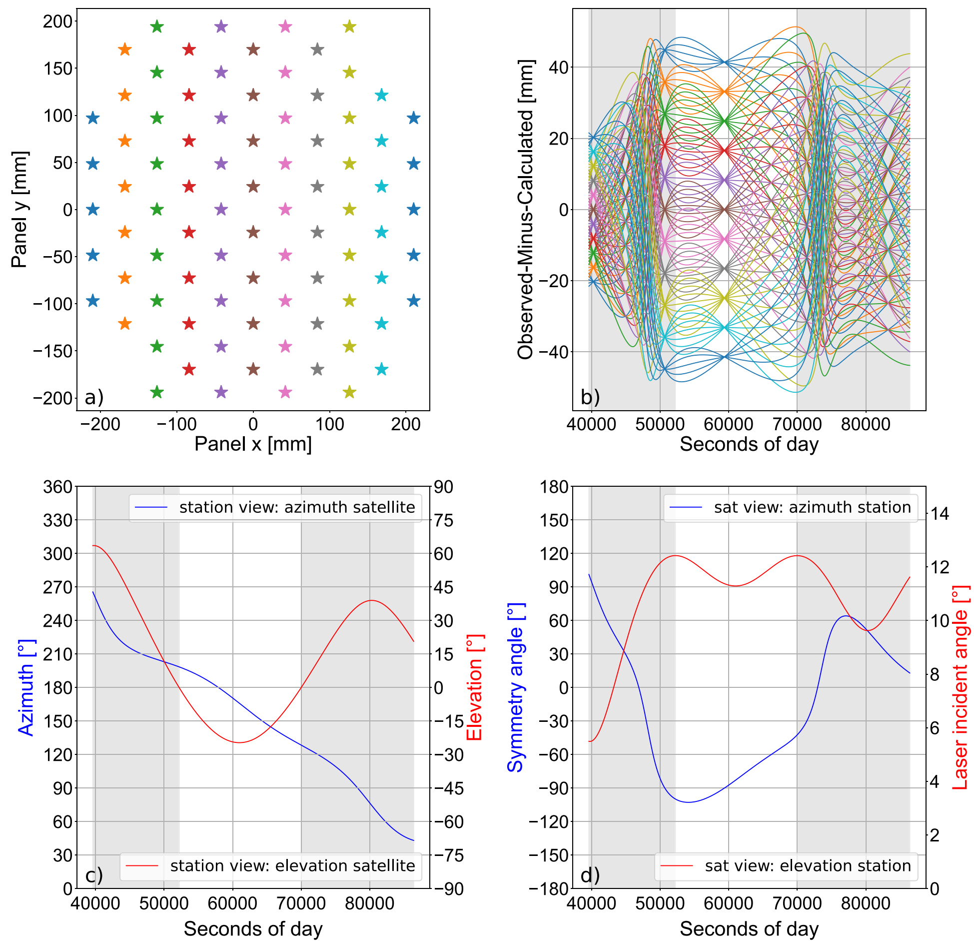

Fig. 2 Simulated SLR residuals for the IOV panel satellite Galileo 103 (NORAD: 38857). **a** Graphical display of the distribution of CCRs on the IOV panel. **b** Color coded simulated SLR residuals for 2021/02/14 UTC 11:00–24:00. **c** Azimuth and elevation of the satellite as seen from the station. **d** Azimuth (symmetry angle) and elevation (laser incident angle) of the station as seen from the satellite. In gray the parts of the pass where the satellite is above the horizon are highlighted

beam incident angle correlate well with the residual simulations (Fig. 2d). It can be seen that intermediate symmetry conditions also occur throughout the day.

In-orbit measurements—measurement setup

A tool has been developed to predict symmetry passes with respect to the Graz SLR station accordingly. Based on the latest predictions, the observer is warned by a popup message shortly before a symmetry pass occurs. The measurement goal was to cover a period of ± 5 min around the central symmetry epoch with continuous observations. Preliminary tests showed that due to the small separation between the CCRs symmetry passes with $\alpha_{symm} = \pm 0°$ and $\alpha_{symm} = \pm 60°$ are not resolvable within the SLR data. This can be explained by the 2–3 mm single shot RMS precision limit of our SLR station measurements. Therefore, our focus in the following was to measure $\alpha_{symm} = \pm 30°$ and $\alpha_{symm} = \pm 90°$ symmetry conditions. Between 2020/06/11 and 2021/04/24 a dedicated campaign was performed measuring more than 100 symmetry passes in linear and circular polarization. In the results section, a method is presented to calculate the incident angle of the laser beam from raw SLR data only. Detailed data analysis sheets are calculated for each of the recorded passes.

Remote location—measurement setup

A spare IOV retroreflector panel was provided on loan from ESA to perform measurements at a remote location on a mountain at 1200 m surface elevation, 32 km outside of Graz, with direct line of sight to the SLR station (Fig. 3c, image of the green laser beam originating from Graz SLR station). The reflector panel (Fig. 3a, covered within the black housing) was mounted on an Avalon M-Zero mount, which allows its azimuthal fork arm to be moved horizontally to mount the panel in direct extension of the azimuth axis. Thus, by changing the azimuth of the mount, the incident angle of the laser beam α_{laser} can be varied. Changing the elevation angle of the mount is related to the symmetry angle α_{sym}. The zero alignment of the panel with respect to the SLR station (ensuring that the panel normal vector is facing towards Graz SLR station) was done by:

(1) Aligning the panel with the mounted add-on telescope by analyzing an image of the laser beam on a CMOS

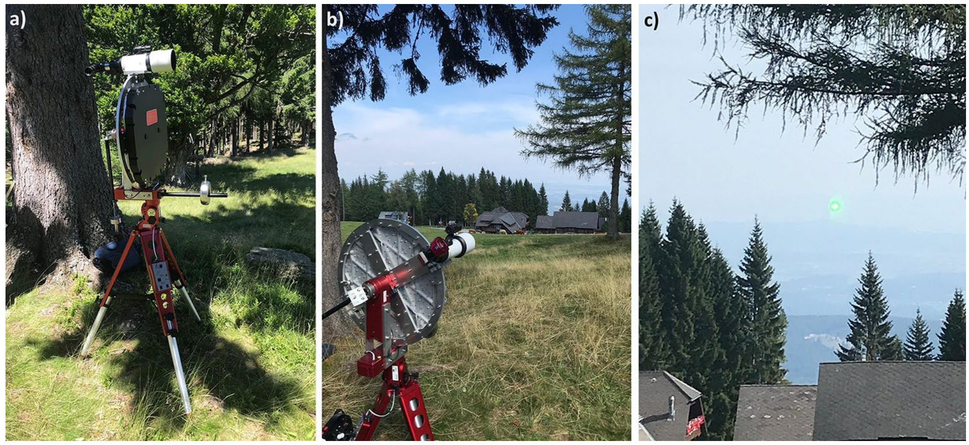

Fig. 3 Measurement setup at the remote location. **a** overall setup of the panel (with cover) mounted on an Avalon telescope mount, the white add-on telescope with attached camera was used to perform the 0° pre-alignment of the panel w.r.t. Graz station. **b** The setup pointing towards Graz SLR station. **c** Close-up of the laser firing towards the remote location (green flash)

camera (Fig. 3b, small white add-on telescope) with attached camera.

(2) Fine-tuning the alignment by covering the CCR panel and optimizing the number of return photons from the reflection of mirrors inside the panel holder.

The mount was rotated to various combinations of incident angle and symmetry conditions using a self-written ASCOM-based Python software (Fig. 4). Each position was held for a predefined time, while storing mount parameters and timestamps for later SLR return identification. In the results section, using only the raw data sets, the incident angle was calculated and compared to the mount values.

ILRS Normal point formation

Within the ILRS, raw SLR data must be post-processed in a defined way. The data cleaning pipeline starts with residual calculation, coarse outlier removal, systematic trend removal, computation of fitted residuals and outlier identification based on a 2.2 sigma criterion. The process is performed iteratively until the accepted data set (corresponding to the reflected photons from the target) does not change anymore. Normal point formation involves dividing the data into bins, calculating the mean fit residual value and the mean epoch of the accepted data, finding the observation closest to the mean epoch and then calculating the normal point and RMS from the generated data. For Galileo satellites, the routine relies on the entire data set. In the results section of this paper, alternative ways of generating the normal points based on the symmetry conditions mentioned before are discussed.

Results and discussion

In the following chapter (1) the results of the measurements the spare panel placed at a location with direct sight connection, 32 km away from the SLR station, (2) the measurement campaign to Galileo satellites and (3) the normal point analysis methods are discussed.

SLR measurements, remote location

At the remote site, 32 km from Graz Observatory, 30° and 90° symmetry conditions were set with the panel mounted on the astronomical mount. The incident angle was varied from 5° to 15° in increments of 0.5° and between 10° and 13° in increments of 0.2°. It was found that the actual position of the mount can be slightly different from the desired value after the final rotation. Therefore, at the beginning and at the end of the measurement, the current mount tilt value

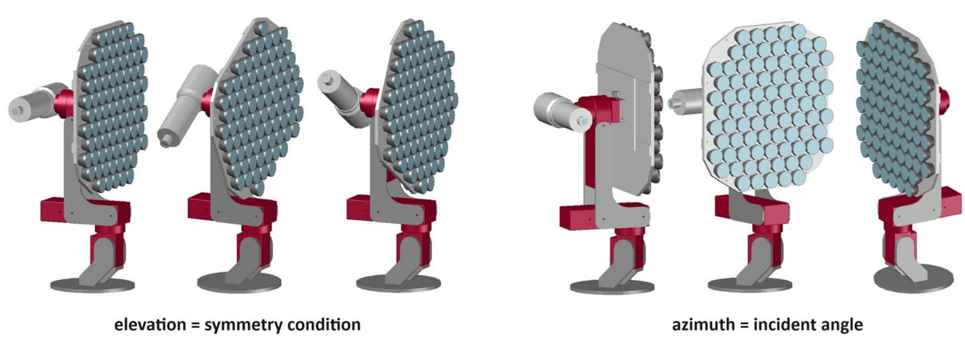

Fig. 4 Explanation of the orientation of the panel at the remote location: Changing the elevation angle of the mount leads to a change of the symmetry condition; a change in azimuth leads to different incident angles

was read out and saved to a file along with the current GPS time. The mount value will be referred to as the predicted incident angle α_{pred}.

Each measurement was performed for 60 s, while keeping the return rate at a single photon level by adjusting the divergence of the laser beam. In the generated data sheets, the raw data set (Fig. 5, upper left) clearly shows patterns of increased data density at constant ranges. The range values are discretized to calculate a smoothed Gaussian residual curve (Fig. 5, lower graph red curve). For each 1 mm bin containing N range measurements y_i, the Gaussian smoothing is calculated according to the following equation:

$$y_{sm} = y_{arb} \sum_{i=0}^{N} \exp^{\frac{-0.5(y_i - y_{cen})^2}{\sigma^2}} \tag{5}$$

The parameter sigma σ corresponds to the weighting/averaging of the values in the bin and determines the smoothing of the range residuals. For the following plots, sigma is set to 0.001. The derivative is taken from the smoothed data set (Fig. 5, green curve). Both plots are compared to a histogram calculated using the same bin width (Fig. 5, green curve). A Lomb analysis of the derivative of the smoothed curve is then performed to examine the periodicity with respect to the range between the different rows. The results of this analysis shows a clear peak at certain range. Knowing the geometry of the Galileo panel, the x-axis was translated into the incident angle (Fig. 5, upper right). The maximum of the curve is detected and then compared to the predicted incident angle—the angle given by the mount.

For the 30° symmetry case, where the mount was moved to a nominal incident angle of 10.8°, the value returned from the mount after slewing was $\alpha_{pred} = 10.76°$. Data analysis of the measurement yielded a laser beam incident angle value of $\alpha_{calc} = 10.13°$.

The difference between the mount-based and measured angle of incident was calculated for all measurement sets. The smaller the incident angle, the closer the individual peaks become to each other, and at some point the Lomb periodogram can no longer detect a distinct peak due to the intrinsic measurement precision of the SLR technique. For the analyzed symmetry conditions, it was possible to reliably calculate an incident angle above 9° (90° symmetry: Fig. 6a, 30° symmetry Fig. 6c).

The offset between the mount angle and the calculated incident angle was also compared to the nominal mount angle (Fig. 6b, d). Furthermore, the mean ($\Delta\alpha_{mean}$) and standard deviation ($\Delta\alpha_{std}$) of the offsets were calculated (Table 1). Both symmetry angles showed a distribution of incident angle offsets around a mean value, and no drift was found in the data set, indicating the quality of the method used. The measurement on the second day 2021/09/14 gave better results for the 30° symmetry condition than the one on the first day 2021/07/06. For the 90° symmetry condition, the standard deviations were comparable on both days.

On the second day, the mean value of both 90° and 30° symmetry conditions was significantly better. The detected offsets are expected to come from an initial misalignment during the 0° alignment routine using CCRs and mirrors. For the measurement on the second day, an RMS analysis ($\Delta\alpha_{rms}$) of the returns coming from the full panel moving

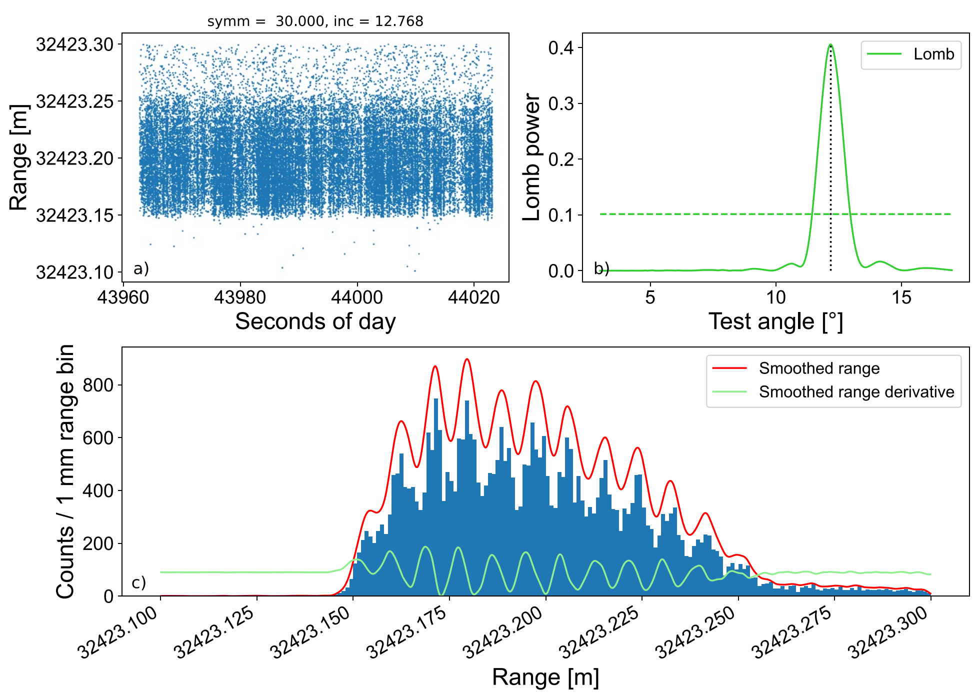

Fig. 5 Datasheet for a measurement to the remote location at 30° panel symmetry. The incident angle of the mount was set to 12.77°. The calculated incident angle derived from the range measurements resulted in 12.13°

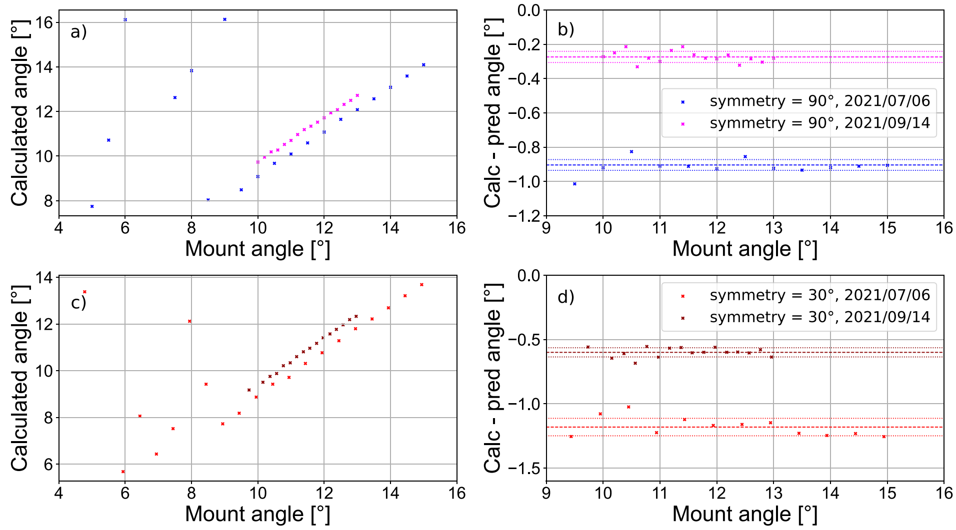

Fig. 6 Remote measurements to a spare Galileo IOV panel: Read out mount incident angle [°] in dependence of the calculated incident angle [°] as derived from the SLR measurements to the remote location 32 km from Graz SLR station for 30° (**a**) and 90° symmetry angle (**c**). The negative offsets between calculated (from SLR measurements) and predicted (from the read-out mount angle) result from initial 0° misalignment of the panel (**b**, **d**). Above 9° incident angle the presented method reliably determines the incident angle

Table 1 Ground measurement to a spare IOV panel 32 km away from the observatory for symmetry conditions 30° and 90°. A misalignment error was detected proving an accuracy of the method below 0.1

Day	Symm	$\Delta\alpha_{mean}$(°)	$\Delta\alpha_{std}$ (°)	$\Delta\alpha_{rms}$(°)
2021/07/06	30°	−1.18	0.068	
2021/07/06	90°	−0.90	0.033	
2021/09/14	30°	−0.27	0.036	−0.31
2021/09/14	90°	−0.60	0.031	−0.64

over 0° degree resulted in comparable 0° alignment offsets for both symmetry conditions.

Taking into account alignment inaccuracies, mount positioning errors and errors due to Gaussian smoothing and period detection, it is assumed that the incident angle can be accurate to within at least 0.1° under optimal conditions (Table 1).

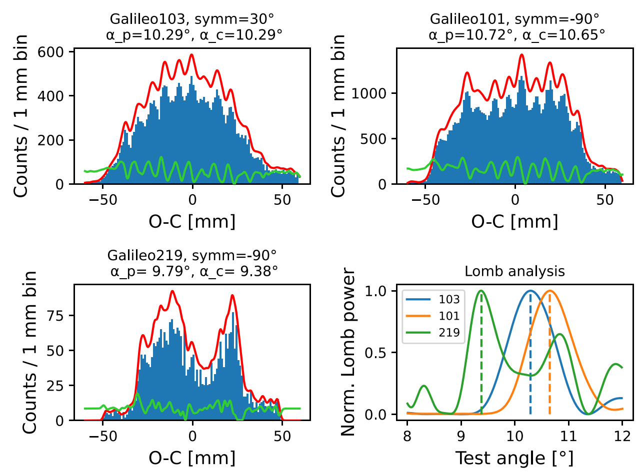

Fig. 7 Histogram distribution (blue), smoothed range residuals (red) and first derivative (green) for three Galileo satellites (Galileo 103, Galileo 101, Galileo 219). Lower right: Lomb analysis displayed for tested incident angles between 8° and 12°, showing a clear maximum at 10.29°, 10.65° and 9.38°. Galileo 219 shows a highly asymmetric reflection pattern

SLR measurements, in-orbit

A large campaign analyzing more than 100 different Galileo symmetry passes was performed in 2021. As during the remote location measurements, the symmetry conditions of 30° and 90° were analyzed. As in Fig. 5, the range residual data was analyzed by forming a histogram, together with smoothed range residuals and their first derivative (Fig. 7).

Three example passes highlight the different reflectance profiles depending on the symmetry angle and the panel type. The Lomb analysis of the derivative shows clearly identifiable peaks corresponding to certain incident angles. For the two shown examples Galileo 103 (average return rate 1.8%) and Galileo 101 (2.7%), the differences from the TLE predicted angle are less than 0.1° (Fig. 7). The measured pass of Galileo 103 corresponds to the simulated residuals as shown in Fig. 2. The larger offset for the Galileo FOC satellite 219 is connected to the low return rate (0.4%), following from the smaller FOC CCRs and the overall lower number of CCRs on the panel. This results in patterns that are harder to discriminate. Some Galileo FOC measurements show an asymmetric distribution of returns with a significant reduction in signal strength, especially around the 90° symmetry condition. For example, at an incident angle of 9.8°. Galileo 219 shows two distinct peaks at − 1.1 cm and + 2.2 cm, and a valley at + 0.7 cm. Using 2.2 sigma clipping on the entire data set of such a distribution will offset the normal point. Such an intensity distribution is expected to result from the far field diffraction pattern (FFDP) of the individual CCRs:

The reflective backside of Galileo CCRs is uncoated and relies on total internal reflection. Therefore, the resulting FFDP consists of six side lobes and a central maximum. The side lobes are hexagonally distributed at angles based on Airy diffraction (depending on the diameter of the CCR). For Galileo satellites at 23,200 km altitude, the velocity aberration of 25 µrad correlates with the maximum values in the FFDP; for IOV satellites, a further distribution of energy at certain angles is achieved by intentional spoiling (tilting) of the backsides of the CCRs. Due to the minimum values in the pattern of each individual CCR, an equal alignment of all CCRs of the panel would lead to certain observer-satellite geometries where the reflected intensity is very low. For this reason, Galileo panels are "clocked"—the CCRs are rotated in 15° (FOC) or 20° (IOV) increments—resulting in a more uniform overall FFDP. However, depending on how many CCRs of which clocking orientation are within a row of the symmetry condition, the reflected intensity can still vary, leading to different intensities within each of the peaks.

Using a fixed set of analysis parameters, a total of 98 passes were analyzed and corresponding data sheets were generated. The incident angle difference (calculated minus predicted values) was plotted for each individual Galileo satellite up to Galileo-219 (Fig. 8). It can be seen that the standard deviation of the offset is larger for FOC satellites (1 sigma = 1.26°, dashed red line) than IOV satellites (1 sigma = 0.53°, dashed blue line) than. Furthermore, there is no clear dependence on individual satellites. However, Galileo satellite 213 showed a slightly larger positive offset than the other satellites.

The predicted incident angles were compared with the incident angle difference (Fig. 8b) for IOV type (blue) and FOC type (red) panels and plotted separately for linear (x) and circular (o) laser light polarization. It can be clearly seen that the difference to TLE values is larger for IOV panels than for FOC panels. One reason for this is that for FOC satellites, due to the smaller distance between the CCRs, the different peaks appear closer together and are therefore more difficult to separate. Second, due to the smaller aperture and fewer CCRs, the overall return rate is lower, resulting in weaker signals. For IOV, only 1 out of 31 measured passes had an incident angle difference relative to the calculated value greater than 1°. For FOC panels, 23 out of 67 calculated angles had an offset greater than 1° relative to the predicted angle. For FOC satellites, a few incident angles are much larger than 12°. These are the two Galileo satellites in eccentric orbits.

The predicted incident angles are plotted against the Lomb-Scargle power (Fig. 8c). It is clearly visible that the Lomb power correlates with the incident angle for IOV and FOC panels. Due to the larger separation and the increased number of CCRs, the pattern identification is easier for IOV and favors larger incident angles.

The calculated incident angle can be compared with the satellite telemetry as obtained from the Attitude and Orbit Control System (AOCS) of the satellite. The AOCS keeps the spacecraft pointing at the Earth mainly based on infrared Earth sensors and the Sun sensors. The infrared Earth sensors do this by detecting the contrast between the cold of deep space and the heat of the Earth. These sensors provide a direct measurement of the pitch and roll angle of the satellite. The telemetry from the satellite system has an inherent noise better than ± 0.1° in roll and pitch (Dungate et al. 2005) while the error of the calculated tilt angle is ± 0.2° assuming a 1 mm error in the sub-peak estimation while neglecting datasets with low return rate.

By taking the measurements from Fig. 8 for the ± 90° symmetry condition it is possible to get a direct measurement of the roll angle of the satellite. Figure 9 provides a comparison of the determined roll angle against the roll

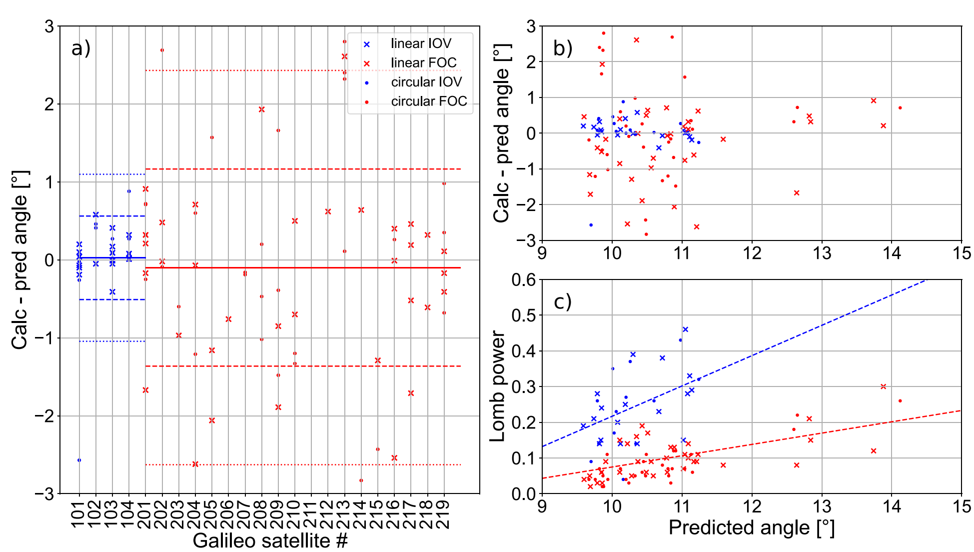

Fig. 8 Offset between predicted and calculated incident angle for **a** different Galileo satellites, **b** as compared to the predicted incident angle (from TLEs), **c** Lomb power resulting from the incident angle calculation

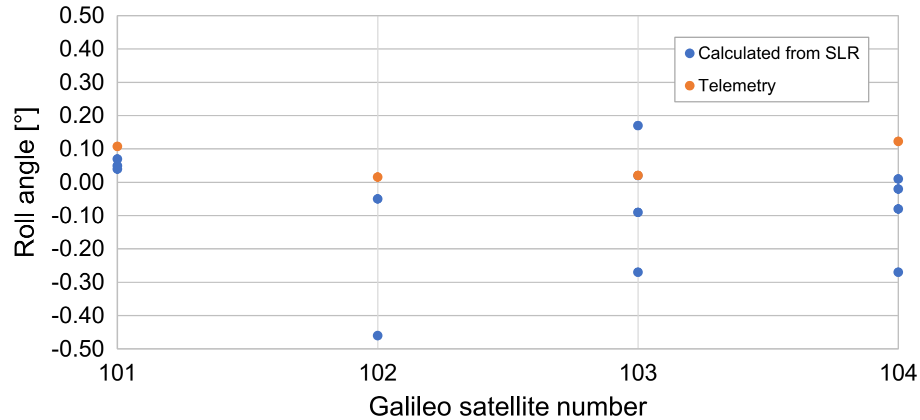

Fig. 9 Roll angle observed from telemetry and the calculated roll angle from the ± 90° symmetry condition

angle from satellite telemetry data given by ESA. Though satellites Galileo 101 and Galileo 104 present a small + 0.1° offset during the observation period, the spread and noise of the available measurements does not allow for a clear estimation of the value.

The estimation of pointing errors or intentional GNSS bias can be of added value to explain the perturbing forces on the satellite (Bury et al. 2020). It can be concluded that the SLR attitude derivation technique can provide information about the attitude pointing accuracy with ± 0.2° accuracy which can be increased with an additional number of measurements.

Additionally, it can be concluded that if the signal strength from the satellite and the separation between the CCRs is large enough, the incident angle can be accurately determined. Future ultra-high repetition rate stations operating at low pulse energies with single photon return rates should be able to identify the satellite signature more clearly.

New normal point formation techniques

Based on the residual distribution which shows increased data density under symmetry conditions, two alternative normal point formation techniques are proposed: A peak-based method and a pattern correlation-based method.

Peak-based normal point formation: After orbit cleaning and smoothing the post-processed range data set, the peaks correlating to the center of each row can be determined (compare Figs. 5, 7). For each row, the data set is then cut based on the neighboring peaks. The upper and lower data cutoffs are defined by the average of the selected peak and the neighboring peaks. The cut dataset for each peak is then treated as regular Galileo SLR data (flattened by orbit-based parameter adjustment and 2.2 sigma clipped). This method allows of up to 11 normal points (90° symmetry) and up to 12 normal points (30° symmetry) to be generated simultaneously.

Cross-correlation method: A simulated residual pattern is calculated by forming a Gaussian distribution at the average position for each CCR. The width of the Gaussian function is based on the SLR precision of 3 mm. Adding the individual Gaussian led to overall simulated distribution of the whole panel (Fig. 10a, blue). The expected return pattern of the residuals is cross-correlated (Fig. 10b, blue) with the observed one (Fig. 10a, orange) to identify the offset (Fig. 10, red vertical dots) which will then be applied to correct the normal points. It is investigated here for the same passes.

The calculated normal points were plotted and compared by using the available Galileo Precise Orbit Determination (POD) orbits (Fig. 11). The original normal points using the full data set are plotted in black color, the peak-based normal points are highlighted in red, and the correlation normal points in cyan. In addition, the central normal point of the peak-based method is highlighted in blue. For 90° symmetry and an odd number of 11 rows, the central column is simply the 6th normal point. For 30° symmetry, the central normal point is determined by calculating the average of the two innermost rows. The difference from the original normal point formation method is calculated to highlight the offsets between the different methods, showing an improvement of the normal points. The histogram of the fitted raw POD range residuals is generated to show the distribution of the normal point relative to the peaks in the data.

As an example, two analyzed IOV passes are shown. A significant offset (up to 4 mm) was found compared to the original normal point formation method. Variations in the data set can be caused by a different resulting FFDP of each row, thermal changes in the FFDP, from sensor specific noise distribution based on the return rate. The analysis showed that the normal points from both alternative normal point formation techniques were 0POD reference trajectory values. Pattern correlation and peak-based methods showed similar results, differing by up to 1 mm.

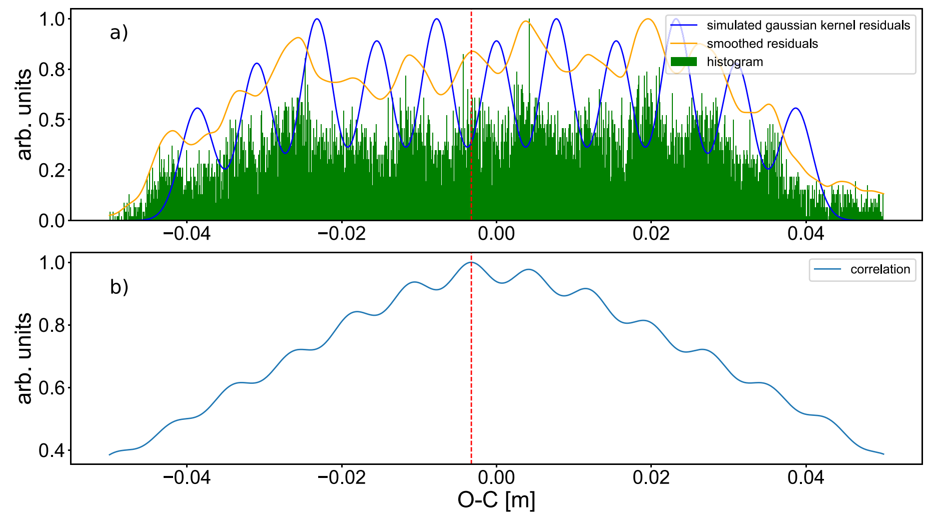

Fig. 10 Visualization of cross-correlation method. **a** The histogram of the measured data (green) is plotted together with the smoothed residuals (orange) and the simulated Gaussian kernel residuals. **b** The maximum of the cross-correlation between simulated and measured data corresponds to the offset applied to the normal point (dashed red line)

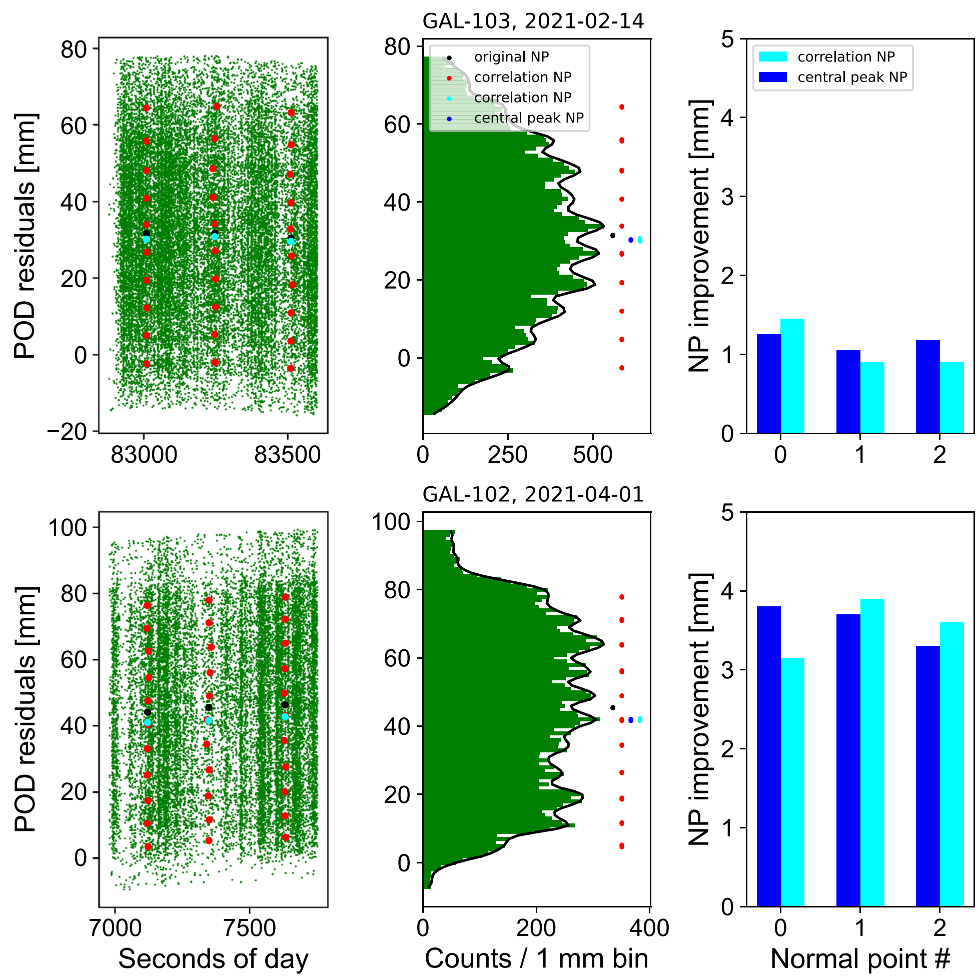

Fig. 11 Alternative normal point formation. top row: Galileo 103, 30° symmetry condition, day 045/2021; bottom row Galileo 102, 90° symmetry condition, day 091/2021. Left column: Full rate data POD residuals with normal points calculated with different methods. Center column: Histogram and smoothed residuals. Right column: Improvement of normal point w.r.t. reference orbit

The current observation strategy (connected to ILRS recommendation) in Graz is to get approx. 1000 points per normal point to achieve optimum precision. After this threshold the observers are instructed to switch to the next target. The shown pass of Galileo 103 (Fig. 11) was continuously measured for approx. 700 s covering a bit less than 3 normal point durations. The number of points per normal point are given in Table 2, indicating that a sufficient precision can be reached even for each individual normal point. Considering future developments such as MHz laser ranging with laser

Table 2 For the time interval t1, t2, t3 of three normal points, the number of points within full-data normal point is compared to the individual normal points of the peak based method

pts/NP	full	# 1	#2	#3	#4	#5	#6	#7	#8	#9	#10
t1	10,585	572	824	953	1241	1252	1230	1154	1179	1025	631
t2	10,142	600	773	1009	1115	1152	1171	1018	1082	987	693
t3	6985	376	552	637	823	905	722	674	719	683	485

powers of multiple Watts, will allow for targets signature-based data analysis, also for other SLR satellites.

Summary and conclusion

Galileo symmetry conditions occur whenever the panel is aligned such that multiple CCRs are aligned at equal distances with respect to the observing station. Characteristic patches of dense data form within the raw SLR data sets from which a histogram or smoothed range residuals can be calculated. The range differences between the individual rows can be used to calculate the angle of incidence of the laser beam with respect to the panel.

Ground-based measurements were performed to a spare Galileo IOV panel fixed on an astronomical mount on a hill 32 km outside the Graz SLR station. Different symmetry orientations were investigated and under optimal conditions it was possible to determine the incident angle down to 9° incident angle for symmetry conditions of 30° and 90° with an accuracy of less than 0.1°. The larger the incident angle, the easier it was to identify the rows and calculate the incident angle. Constant offsets to the nominal mounting values were found and initial panel misalignments of less than 1° were identified.

Simulated SLR residuals were generated, allowing accurate prediction of the symmetry conditions of existing Galileo satellites based on yaw steering laws. More than 100 passes to Galileo IOV and FOC satellites were measured and the laser beam incident angle was calculated from the measurements. It was found that the accuracy of the measurement correlates with the separation of the CCR rows. As mentioned before IOV panels use larger CCRs than FOC and hence the distance between the CCR is also larger. Accurate incident angle measurements could play an important role in validating on-board telemetry.

In-orbit based measurements were compared with satellite telemetry for the IOV satellites. The attitude was reconstructed with $\pm 0.2°$ accuracy.

Two new normal point formation techniques based on the symmetry condition data distribution were presented, showing an offset up to 4 mm compared to the method based on the full panel data set. The application of the pattern correlation method seems promising for general non-symmetry passes. More accurate normal points could eventually help improve SLR-based orbit predictions or the consistency between the GNSS-based and the SLR-based realization of the ITRF reference frame help to In the future, MHz satellite laser ranging (Wang et al. 2021) will provide high precision results with superior temporal resolution. Due to the higher power (40 W) with pulse energies strictly in the single-photon regime, the number of returns per second can be significantly increased. This allows for improved pattern identification and thus more advanced normal point formation methods to address the issue of satellite signature in the datasets. For the peak-based normal point formation, observation strategies could be adapted to favor symmetry conditions with improved normal point precision.

Acknowledgements Special thanks go to the European Space Agency for providing us with a spare retroreflector panel, which allowed us to perform very interesting measurements at the remote location in the Austrian mountains, outside the clean-room environment.

Author contributions MS, FG, ES and GK designed the research. MS performed simulations, data analysis and post-processing, developed the peak-based method and wrote the main manuscript text. FK designed and constructed the rotation stage for the Galileo panel and adapted Graz station setup for tracking. PW, FK and MS conducted the measurements to the remote location. AS developed the correlation-based method. FD referenced the measurement with respect to Galileo POD orbits.

Funding Open access funding provided by Österreichische Akademie der Wissenschaften. The study "Galileo attitude determination using mm SLR measurements" was funded within the H2020 program H2020-ESA-038 GNSS Evolutions—Experimental Payloads and Science Activities. The work reported in this paper has been performed and fully funded under a contract of the European Space Agency in the frame of the EU Horizon 2020 Framework Programme for Research and Innovation in Satellite Navigation. The views presented in the paper represent solely the opinion of the authors and should be considered as R&D results not necessarily impacting the present and future EGNOS and Galileo system designs".

Data availability Normal point data of Galileo satellites are found at the analysis centers within the ILRS.

Declarations

Conflict of interest We declare that the authors have no competing interests as defined by Springer, or other interests that might be perceived to influence the results and/or discussion reported in this paper.

Consent for publication All authors read and approved the final manuscript to be published. We agree to be accountable for all aspects of the work in ensuring that questions related to the accuracy or integrity of any part of the work are appropriately investigated and resolved.

References

Arnold DA (2002) Retroreflector array transfer functions. In: 13th international laser ranging workshop, Washington DC. https://ilrs.gsfc.nasa.gov/docs/retro_transfer_functions.pdf

Boni A et al (2011) World first SCF-test of the NASA-GSFC LAGEOS sector and hollow retroreflector. In: 17th international workshop on laser ranging, Bad Koetzing. https://cddis.nasa.gov/lw17/docs/papers/session11/06-A_Boni_ILRS_talk_article.pdf

Brunelli R (2009) Template matching techniques in computer vision: theory and practice. Wiley

Bury G, Sośnica K, Zajdel R (2018) Multi-GNSS orbit determination using satellite laser ranging. J Geod. https://doi.org/10.1007/s00190-018-1143-1

Bury G, Sośnica K, Zajdel R, Strugarek D (2020) Toward the 1-cm Galileo orbits: challenges in modeling of perturbing forces. J Geod. https://doi.org/10.1007/s00190-020-01342-2

Chandler KN (1960) On the effects of small errors in the angles of corner-cube reflectors. J Opt Soc Am 50(3):203–206. https://doi.org/10.1364/JOSA.50.000203

Ciufolini I, Matzner R, Paolozzi A, Pavlis EC, Sindoni G, Ries J, Gurzadyan V, Koenig R (2019) Satellite laser-ranging as a probe of fundamental physics. Sci Rep 9(1):15881. https://doi.org/10.1038/s41598-019-52183-9

Cordelli E, Vananti A, Schildknecht T (2020) Analysis of laser ranges and angular measurements data fusion for space debris orbit determination. Adv Space Res 65(1):419–434. https://doi.org/10.1016/j.asr.2019.11.009

Degnan JJ (2012) A tutorial on retroreflectors and arrays for SLR. In: International technical laser workshop 2012, Frascati. https://ilrs.gsfc.nasa.gov/docs/2012/degnan_retrotutorialppt_121105.pdf

Dell'Agnello S et al (2011) Creation of the new industry-standard space test of laser retroreflectors for the GNSS and LAGEOS. Adv Space Res 47:822–842. https://doi.org/10.1016/j.asr.2010.10.022

Dell'Agnello S et al (2012) SCF-Test of a Galileo-IOV retroreflector and thermal-optical simulation of a novel GNSS retroreflector array on a critical orbit. In: 2012 IEEE First AESS European conference on satellite telecommunications (ESTEL). IEEE, Rome, pp 1–6

Delva P et al (2019) Testing the gravitational redshift with Galileo satellites. In: Proceedings of the "Rencontres de Moriond—Gravitation", La Thuile. https://arxiv.org/abs/1906.06161

Dequal D, Agnesi C, Sarrocco D, Calderaro L, Santamaria Amato L, Siciliani de Cumis M, Vallone G, Villoresi P, Luceri V, Bianco G (2021) 100 kHz satellite laser ranging demonstration at Matera Laser Ranging Observatory. J Geod 95(2):26. https://doi.org/10.1007/s00190-020-01469-2

Dilssner F, Strangfeld A, Gonzales F, Schoenemann E, Steindorfer M (2022) Galileo mission recent results, ongoing support and future launches. In: 22nd international workshop on laser ranging, Guadalajara. https://www.youtube.com/watch?v=BC1uBW5wWRU

Dungate D, Hardacre S, Pigg MC, Liddle D, Lefort X (2005) GSTB-V2/A normal mode AOCS design. In: 6th international ESA conference on guidance, navigation and control systems, Loutraki

European GNSS Supervisory Authority (2020) GNSS user technology report, 3rd edn. Publications Office, LU

ILRS (2023) Galileo: Retroreflector Information. https://ilrs.gsfc.nasa.gov/missions/satellite_missions/. ILRS International Laser Ranging Service. Accessed Nov 2023

Kirchner G, Koidl F, Prochazka I, Hamal K (1999) SPAD time walk compensation and return energy dependent ranging. In: 11th International Workshop on Laser Ranging, Deggendorf. https://cddis.nasa.gov/lw11/docs/twc_sig2.pdf

Kodet J, Prochazka I, Koidl F, Kirchner G, Wilkinson M (2009) SPAD active quenching circuit optimized for satellite laser ranging applications. In: Proceedings of SPIE—The International Society for Optical Engineering, vol 7355

Kucharski D, Kirchner G, Otsubo T, Koidl F (2015) A method to calculate zero-signature satellite laser ranging normal points for millimeter geodesy—a case study with Ajisai. Earth Planet Space 67(1):34. https://doi.org/10.1186/s40623-015-0204-4

Kucharski D et al (2017) Photon pressure force on space debris TOPEX/Poseidon measured by satellite laser ranging: spin-up of TOPEX. Earth Space Sci 4(10):661–668. https://doi.org/10.1002/2017EA000329

Long M, Zhang H, Yu RZ, Wu Z, Qin S, Zhang Z (2022) Satellite laser ranging at ultra-high PRF of hundreds of kilohertz all day. Front Phys. https://doi.org/10.3389/fphy.2022.1036346

Luceri V, Pirri M, Rodríguez J, Appleby G, Pavlis EC, Müller H (2019) Systematic errors in SLR data and their impact on the ILRS products. J Geod 93(11):2357–2366. https://doi.org/10.1007/s00190-019-01319-w

Montenbruck O, Schmid R, Mercier F, Steigenberger P, Noll C, Fatkulin R, Kogure S, Ganeshan AS (2015) GNSS satellite geometry and attitude models. Adv Space Res 56(6):1015–1029. https://doi.org/10.1016/j.asr.2015.06.019

Murphy TW Jr, Goodrow SD (2013) Polarization and far-field diffraction patterns of total internal reflection corner cubes. Appl Opt 52(2):117. https://doi.org/10.1364/AO.52.000117

Nugent LJ, Condon RJ (1966) Velocity aberration and atmospheric refraction in satellite laser communication experiments. Appl Opt 5(11):1832–1837. https://doi.org/10.1364/AO.5.001832

Otsubo T, Appleby GM, Gibbs P (2001) Glonass laser ranging accuracy with satellite signature effect. Surv Geophys 22:509–516. https://doi.org/10.1023/A:1015676419548

Pearlman MR, Degnan JJ, Bosworth JM (2002) The international laser ranging service. Adv Space Res Res 30(2):135–143. https://doi.org/10.1016/S0273-1177(02)00277-6

Prochazka I, Bimbova R, Kodet J, Blazej J, Eckl J (2020) Photon counting detector package based on InGaAs/InP avalanche structure for laser ranging applications. Rev Sci Instrum 91(5):056102. https://doi.org/10.1063/5.0006516

Samain E, Exertier P, Courde C, Fridelance P, Guillemot P, Laas-Bourez M, Torre J-M (2015) Time transfer by laser link: a complete analysis of the uncertainty budget. Metrologia 52(2):423. https://doi.org/10.1088/0026-1394/52/2/423

SLRF2020 Product, Greenbelt, MD, USA (2020) NASA Crustal Dynamics Data Information System (CDDIS). Accessed 22 July 2023

Sośnica K, Jäggi A, Thaller D, Beutler G, Dach R (2014) Contribution of Starlette, Stella, and AJISAI to the SLR-derived global reference frame. J Geod 88(8):789–804. https://doi.org/10.1007/s00190-014-0722-z
Sośnica K, Thaller D, Dach R, Steigenberger P, Beutler G, Arnold D, Jäggi A (2015) Satellite laser ranging to GPS and GLONASS. J Geod 89:725–743. https://doi.org/10.1007/s00190-015-0810-8
Steindorfer MA, Kirchner G, Koidl F, Wang P, Wirnsberger H, Schoenemann E, Gonzalez F (2019) Attitude determination of Galileo satellites using high-resolution kHz SLR. J Geod 93(10):1845–1851. https://doi.org/10.1007/s00190-019-01284-4
Steindorfer MA, Kirchner G, Koidl F, Wang P, Jilete B, Flohrer T (2020) Daylight space debris laser ranging. Nat Commun 11(1):3735. https://doi.org/10.1038/s41467-020-17332-z
Strugarek D, Sośnica K, Arnold D et al (2022) Satellite laser ranging to GNSS-based Swarm orbits with handling of systematic errors. GPS Solut 26:104. https://doi.org/10.1007/s10291-022-01289-1
Thaller D, Dach R, Seitz M, Beutler G, Mareyen M, Richter B (2011) Combination of GNSS and SLR observations using satellite co-locations. J Geod 85:257–272. https://doi.org/10.1007/s00190-010-0433-z
Thaller D, Sośnica K, Steigenberger P, Roggenbuck O, Dach R (2015) Pre-combined GNSS-SLR solutions: what could be the benefit for the ITRF?. In: REFAG 2014. International Association of Geodesy Symposia, vol 146. Springer
Thomas DA, Wyant JC (1977) Determination of the dihedral angle errors of a corner cube from its Twyman-Green interferogram. J Opt Soc Am 67(4):467. https://doi.org/10.1364/JOSA.67.000467
Wang P, Steindorfer MA, Koidl F, Kirchner G, Leitgeb E (2021) Megahertz repetition rate satellite laser ranging demonstration at Graz observatory. Opt Lett 46(5):937. https://doi.org/10.1364/OL.418135
Zajdel R, Masoumi S, Sośnica K et al (2023) Combination and SLR validation of IGS Repro3 orbits for ITRF2020. J Geod 97:87. https://doi.org/10.1007/s00190-023-01777-3

Michael A. Steindorfer received his Ph.D. in Physics at Karl Franzens University in Graz, Austria, focusing on photonics, nanotechnology, biomimetics and 3D-laser lithography. He joined the Space Research Institute of the Austrian Academy of Sciences in 2015 and became Group Leader of Satellite Laser Ranging Group in 2022. His main research interests are satellite laser ranging, space debris laser ranging, attitude determination, optics, raytracing simulations and real-time image analysis.

Franz Koidl is a long-term team member of the SLR group of the Space Research Institute with 30 years of experience in satellite laser ranging, mechanical engineering, electronical engineering and lasers.

Georg Kirchner built Graz SLR station from ground up since 1980 and was group leader within the Space Research Institute until the end of 2021. He has been a member of the ILRS governing board since the beginning.

Peiyuan Wang is working for the SLR group of the Space Research Institute since 2014, with experience in satellite laser ranging, FPGA design, hardware and software development.

Florian Dilssner is a satellite navigation engineer in the Navigation Support Office at ESOC, ESA, Darmstadt, Germany. He earned his Dipl.-Ing. and Dr.-Ing. degrees in geodesy from the University of Hannover, Germany.

Erik Schoenemann is a satellite navigation engineer in the Navigation Support Office at ESA, ESOC, Darmstadt, Germany. He earned his Dipl.-Ing. and Dr.-Ing. degrees in geodesy from the University of Darmstadt, Germany.

Francisco Gonzalez is a Navigation Performance and Verification Engineer at ESA, ESTEC, The Netherlands. He earned his Dipl.-Ing. in geodesy from the University of Jaen, Spain and Dr.- Ing. from the University of Karlsruhe, Germany.

Aaron Strangfeld is a Quantum Engineer at ESA working on Quantum Sensing Technology for future Earth Observation missions.